

UNIVERSITY OF CALIFORNIA
SANTA CRUZ

**SEARCH FOR WW AND WZ RESONANCES IN $\ell\nu qq$ FINAL
STATES IN pp COLLISIONS AT $\sqrt{s} = 13$ TEV WITH THE ATLAS
DETECTOR**

A dissertation submitted in partial satisfaction of the
requirements for the degree of

DOCTOR OF PHILOSOPHY

in

PHYSICS

by

Natasha Woods

December 2019

The Dissertation of Natasha Woods
is approved:

Abraham Seiden, Chair

Mike Hance

Bruce Schumm

Quentin Williams
Vice Provost and Dean of Graduate Studies

Copyright © by

Natasha Woods

2019

Table of Contents

List of Figures	vi
List of Tables	xvi
Abstract	xix
Dedication	xx
Acknowledgments	xxi
I Introduction	1
1 Introduction	2
II Theoretical Motivation	6
2 The Standard Model of Particle Physics	7
2.1 Introduction	7
2.2 Quantum Field Theory	7
2.3 $U(1)_{EM}$ Local Gauge Invariance	8
2.4 Yang-Mills Gauge Theories	11
2.5 Particles in the Standard Model	12
2.6 Higgs Mechanism	17
2.7 Electroweak Theory	18
2.8 Quantum ChromoDynamics	19
3 Standard Model Successes and Limitations	25
4 New Physics Models with Diboson Resonances	28
4.1 Randall Sundrum Bulk Model	28
4.2 Simple Standard Model Extensions	30

III Experimental Setup	32
5 LHC	33
5.1 LHC Layout and Design	35
6 The ATLAS Detector	39
6.1 Coordinate System	42
6.2 Inner Detector	42
6.2.1 Pixel Detector	44
6.2.2 Semiconductor Tracker	45
6.2.3 Transition Radiation Tracker	45
6.3 Calorimeters	46
6.4 Muon Spectrometer	51
6.5 Magnet System	55
6.6 Trigger System	56
IV The Search for WW and WZ Resonances in $\ell\nu qq$ final states	58
7 Dataset and Simulated Samples	59
7.1 Dataset	59
7.2 Simulated Samples	62
8 Objects	63
8.1 Electrons	63
8.2 Muons	64
8.3 Jets	65
8.3.1 Small-R jets	68
8.3.2 Large-R jets	68
8.3.3 Variable Radius jets	72
8.3.4 Jet Flavor Tagging	72
8.4 MET/Neutrinos	73
8.5 Overlap Removal	73
8.6 Reconstructed Resonance Mass (m_{WW})	74
9 Event Selection and Categorization	75
9.1 Pre-selection	76
9.2 Trigger	77
9.3 non-VBF/VBF RNN	79
9.4 Signal Region Definitions	86
9.5 Selection Acceptance and Efficiency	88

10 Background Estimate	91
10.1 Control Regions	92
10.2 Fake Lepton Backgrounds	99
11 Systematic Uncertainties	113
11.1 Experimental Systematics	113
11.2 Theory Systematics	115
12 Statistical Analysis	123
12.1 Likelihood Function Definition	124
12.2 Fit Configuration	124
12.3 Best Fit μ	127
12.4 Discovery Test	127
12.5 Exclusion Limits	129
13 Results	131
13.1 Expected and Measured Yields	131
13.2 Systematic Profiling and Correlations	145
13.3 Discovery Tests	147
13.4 Limits	153
V Quark and Gluon Tagging	155
14 Prospects	156
15 n_{trk} Calibration	163
16 Application	169
VI Conclusion	174
17 Conclusions	175
Bibliography	176

List of Figures

2.1	The particles of the Standard Model.	14
2.2	Summary of how Standard Model particles interact with other Standard Model particles.	15
2.3	This figure shows the three dominant QCD interactions. From Ref. [20]	21
2.4	Strength of the U(1), SU(2), and SU(3) gauge couplings as a function of the energy scale of the interaction (Q). From Ref. [14]	22
2.5	A cartoon of string breaking: the QCD string spanned between quark Q and antiquark \bar{Q} breaks due to $q\bar{q}$ creation [5]	24
3.1	A comparison of cross section measurements at $\sqrt{s} = 7, 8, 13$ TeV from ATLAS compared to theoretical measurements. From Ref. [7]	27
4.1	Cartoon of RS Bulk Model	29
5.1	Scaling of various SM cross sections with \sqrt{s}	34
5.2	The layout of the LHC and the four detectors along the beam line (ATLAS, LHCb, ALICE, CMS).	36
5.3	An overview schematic of the LHC accelerator subsystems.	37
6.1	Overview schematic of the ATLAS detector.	40
6.2	A simplified schematic of how different particles interact and are detected within ATLAS.	41
6.3	Layout of ATLAS Inner Detector	43

6.4	Layout of ATLAS ID Barrel System.	44
6.5	Overview of ATLAS electromagnetic and hadronic calorimeters.	48
6.6	Schematic of ECAL.	49
6.7	Schematic of HCAL.	50
6.8	Schematic of Muon Spectrometer [cite G35]	53
6.9	Schematic of MDT chamber. [cite G35]	54
6.10	Schematic of RPC chamber, which is used for triggering in the central region of the detector [cite G35].	54
6.11	Schematic of TGC chamber, which is used for triggering in the muon end-cap region. [cite G35]	55
6.12	Layout of ATLAS magnet systems.	56
7.1	Integrated luminosity for data collected from ATLAS from 2011 - 2018	60
7.2	Mean number of interactions per crossing for data collected from ATLAS from 2011 - 2018	61
8.1	This figure shows the breakdown of the muon reconstruction efficiency scale factor measured in $Z \rightarrow \mu\mu$ as a function of p_T [6].	65
8.2	[10] This diagram shows the calibration stages for EM jets.	67
8.3	The upper cut on D_2 (a) and jet mass window cut i.e. the upper and lower boundary of the mass (b) of the W -tagger as a function of jet p_T . Corresponding values for Z -tagger are shown in (c) and (d). The optimal cut values for maximum significance are shown as solid markers and the fitted function as solid lines. Working points from $VV \rightarrow JJ$ [ATLAS-HDBS-2018-31-002] is also shown as dashed lines as a reference. Natasha reword?	71
8.4	Natasha write caption	71
9.1	RNN architecture. Natasha add caption	81

9.2	This figure shows the embedded logic in LSTM cells. This image was taken from [25], where a more in depth discussion about LSTMs may be found.	82
9.3	RNN Score distribution for ggF and VBF signals and backgrounds.	83
9.4	ROC curve using k-fold validation for RNN.	84
9.5	Comparison of GGF Z' limits for different RNN score selections. The bottom panel shows the ratio of the upper limits set for different RNN cuts to the cut-based analysis. In this panel smaller numbers, indicate that the expected upper limit is smaller than the cut-based analysis, which is desired.	85
9.6	Event Categorization. Natasha write more.	88
9.7	Selection acceptance times efficiency for the $W' \rightarrow WZ \rightarrow \ell\nu qq$ events from MC simulations as a function of the W' mass for Drell-Yan (left) and VBF production (right), combining the merged HP and LP signal regions of the $WW \rightarrow \ell\nu J$ selection and the resolved regions of the $WW \rightarrow \ell\nu jj$ selection. Note: the VBF selection acceptance for the DY W' is approximately zero in the left plot.	89
9.8	Selection acceptance times efficiency for the $G \rightarrow WW \rightarrow \ell\nu qq$ events from MC simulations as a function of the G mass for (a) Drell-Yan and (b) VBF production, combining the merged HP and LP signal regions of the $WW \rightarrow \ell\nu J$ selection and the resolved regions of the $WW \rightarrow \ell\nu jj$ selection. Note: the VBF selection acceptance for the ggF G'_{KK} is approximately zero in the left plot.	90
10.1	Data MC comparison for the merged WW HP TCR. The bottom panel shows the ratio of the difference between data and simulation to simulation. The red bands include the all systematic and statistical uncertainties on the background.	93

10.2 Data MC comparison for the merged WW LP TCR. The bottom panel shows the ratio of the difference between data and simulation to simulation. The red bands include the all systematic and statistical uncertainties on the background.	94
10.3 Data MC comparison for the merged WZ HP TCR. The bottom panel shows the ratio of the difference between data and simulation to simulation. The red bands include the all systematic and statistical uncertainties on the background.	95
10.4 Data MC comparison for the merged WZ LP TCR. The bottom panel shows the ratio of the difference between data and simulation to simulation. The red bands include the all systematic and statistical uncertainties on the background.	96
10.5 Data MC comparison for the resolved WW TCR. The bottom panel shows the ratio of the difference between data and simulation to simulation. The red bands include the all systematic and statistical uncertainties on the background.	97
10.6 Data MC comparison for the resolved WZ TCR. The bottom panel shows the ratio of the difference between data and simulation to simulation. The red bands include the all systematic and statistical uncertainties on the background.	98
10.7 The E_T^{miss} distribution in MJCR for 2017 data in the electron channel(left), muon channel with W-boson pT < 150 GeV (center) and > 150 GeV (right). Multi-jet templates are given by the difference between the data and simulated distributions.	101
10.8 Postfit Data/MC comparison of distributions of E_T^{miss} , m_T^W , lepton and neutrino p_T , $m_{\ell\nu jj}$, lepton- ν angular distance in the WW electron channel. The MJ template is obtained from the pre-MJ-fit.	102
10.9 Postfit Data/MC comparison of distributions of E_T^{miss} , m_T^W , lepton and neutrino p_T , $m_{\ell\nu jj}$, lepton- ν angular distance in the WW muon channel. The MJ template is obtained from the pre-MJ-fit.	103

10.10 Postfit Data/MC comparison of distributions of E_T^{miss} , m_T^W , lepton and neutrino p_T , $m_{\ell\nu jj}$, lepton- ν angular distance in the WZ untag electron channel. The MJ template is obtained from the pre-MJ-fit.	104
10.11 Postfit Data/MC comparison of distributions of E_T^{miss} , m_T^W , lepton and neutrino p_T , $m_{\ell\nu jj}$, lepton- ν angular distance in the WZ untag muon channel. The MJ template is obtained from the pre-MJ-fit.	105
10.12 Postfit Data/MC comparison of distributions of E_T^{miss} , m_T^W , lepton and neutrino p_T , $m_{\ell\nu jj}$, lepton- ν angular distance in the WZ untag electron channel. The MJ template is obtained from the pre-MJ-fit.	106
10.13 Postfit Data/MC comparison of distributions of E_T^{miss} , m_T^W , lepton and neutrino p_T , $m_{\ell\nu jj}$, lepton- ν angular distance in the WZ untag muon channel. The MJ template is obtained from the pre-MJ-fit.	107
10.14 Postfit Data/MC comparison of distributions of E_T^{miss} , m_T^W , lepton and neutrino p_T , $m_{\ell\nu jj}$, lepton- ν angular distance in the VBF WW electron channel. The MJ template is obtained from the pre-MJ-fit.	108
10.15 Postfit Data/MC comparison of distributions of E_T^{miss} , m_T^W , lepton and neutrino p_T , $m_{\ell\nu jj}$, lepton- ν angular distance in the VBF WW muon channel. The MJ template is obtained from the pre-MJ-fit.	109
10.16 Postfit Data/MC comparison of distributions of E_T^{miss} , m_T^W , lepton and neutrino p_T , $m_{\ell\nu jj}$, lepton- ν angular distance in the VBF WZ electron channel. The MJ template is obtained from the pre-MJ-fit.	110
10.17 Postfit Data/MC comparison of distributions of E_T^{miss} , m_T^W , lepton and neutrino p_T , $m_{\ell\nu jj}$, lepton- ν angular distance in the VBF WZ muon channel. The MJ template is obtained from the pre-MJ-fit.	111
11.1 The $W/Z+jet$ systematics for the a) Merged ggF, b) Resolved ggF, c) Merged VBF, and d) Resolved VBF regions. The top subplot shows the nominal and variation distributions/bands, the middle shows the ratio of the two, and the final shows just the shape of the envelope (the final uncertainty).	117

11.2 The two-point generator comparison between Sherpa and MadGraph for the W/Z+jet samples in the a) Merged ggF, b) Resolved ggF, c) Merged VBF, and d) Resolved VBF regions. The normalization of the Madgraph sample is set to the Sherpa value to consider only shape effects. The bottom inset shows the ratio of the two.	118
11.3 Ratio between the variations of generator (red) and hadronization (blue) variations for the Merged regime for $t\bar{t}$ sample.	119
11.4 Ratio between the variations of generator (red) and hadronization (blue) variations for the Resolved regime for $t\bar{t}$ sample.	119
11.5 Ratio between the variations of ISR up (red) and down (blue) variations for the Merged regime for $t\bar{t}$ sample.	120
11.6 Ratio between the variations of ISR up (red) and down (blue) variations for the Resolved regime for $t\bar{t}$ sample.	121
11.7 Ratio between the variations of FSR up (red) and down (blue) variations for the Merged regime for $t\bar{t}$ sample.	122
11.8 Ratio between the variations of FSR up (red) and down (blue) variations for the Resolved regime for $t\bar{t}$ sample.	122
 12.1 The HVT signal mass resolution as a function of mass fit with a straight line in the Resolved ggF region (left) and VBF (right) region.	126
12.2 The HVT signal mass resolution as a function of mass fit with a straight line in the Merged ggF region (left) and VBF (right) region.	126
 13.1 This figure shows the distribution of $m_{\ell\nu qq}$ in the DY WW control regions.	139
13.2 This figure shows the distribution of $m_{\ell\nu qq}$ in the DY WZ control regions.	140
13.3 This figure shows the distribution of $m_{\ell\nu qq}$ in the VBF WW control regions.	141

13.4 This figure shows the distribution of $m_{\ell\nu qq}$ in the VBF WZ control regions.	142
13.5 This figure shows the distribution of $m_{\ell\nu qq}$ in the GGF WW signal regions.	143
13.6 This figure shows the distribution of $m_{\ell\nu qq}$ in the GGF WZ Untag signal regions.	143
13.7 This figure shows the distribution of $m_{\ell\nu qq}$ in the GGF WZ Tag signal regions.	144
13.8 This figure shows the distribution of $m_{\ell\nu qq}$ in the VBF WZ Tag signal regions.	144
13.9 This figure shows the distribution of $m_{\ell\nu qq}$ in the VBF WZ Tag signal regions.	145
13.10 Ranked systematics and their fitted values for WW DY (right) and VBF (left) selections.	146
13.11 Ranked systematics and their fitted values for WZ DY (right) and VBF (left) selections.	146
13.12 Correlations between systematics for WW DY (right) and VBF (left) selections.	147
13.13 These plots show the measured p_0 value as a function of resonance mass for HVT Z' DY production.	148
13.14 These plots show the measured p_0 value as a function of resonance mass for HVT Z' VBF production.	149
13.15 These plots show the measured p_0 value as a function of resonance mass for HVT W' DY production.	150
13.16 These plots show the measured p_0 value as a function of resonance mass for HVT W' VBF production.	151
13.17 These plots show the measured p_0 value as a function of resonance mass for the RS Graviton DY production.	152
13.18 This figure shows theory, expected and observed limits for HVT W' DY (left) and VBF (right) production.	153

13.19 This figure shows theory, expected and observed limits for HVT Z' DY (left) and VBF (right) production.	154
13.20 This figure shows theory, expected and observed limits for RS Gravitons via DY production.	154
14.1 PDGID of the truth-level parton matched to the small-R jets passing the Resolved GGF WW Signal Region selections for the (a) Leading (b) Sub-Leading jets . These distributions are shown for 300, 500, and 700GeV Z' signals and the background (all simulated backgrounds that pass SR selections).	158
14.2 The number of tracks in small-R jets in events passing the Resolved GGF WW Signal Region selections for the (a) Leading (b) Sub-Leading jets. These distributions are shown for 300, 500, and 700GeV Z' signals and the background.	158
14.3 The number of tracks in background small-R jets in events passing the Resolved GGF WW Signal region selection vs. $\ln(p_T)$ for (a)Leading (b) Sub-Leading jets. The best fit line for the distribution is also shown, as well as the percentage of jets that pass a cut of number of tracks $< 4 \times \ln(p_T) - 5$. Note the number of total entries in these plots has been normalized to one.	159
14.4 The number of tracks in small-R jets in 300GeV Z' events passing the Resolved GGF WW Signal region selection vs. $\ln(p_T)$ for (a)Leading (b) Sub-Leading jets. The best fit line for the distribution is also shown, as well as the percentage of jets that pass a cut of number of tracks $< 4 \times \ln(p_T) - 5$.Note the number of total entries in these plots has been normalized to one.	159

14.5 The number of tracks in small-R jets in 500GeV Z' events passing the Resolved GGF WW Signal region selection vs. $\ln(p_T)$ for (a)Leading (b) Sub-Leading jets. The best fit line for the distribution is also shown, as well as the percentage of jets that pass a cut of number of tracks $< 4 \times \ln(p_T) - 5$. Note the number of total entries in these plots has been normalized to one.	160
14.6 The number of tracks in small-R jets in 700GeV Z' events passing the Resolved GGF WW Signal region selection vs. $\ln(p_T)$ for (a)Leading (b) Sub-Leading jets. The best fit line for the distribution is also shown, as well as the percentage of jets that pass a cut of number of tracks $< 4 \times \ln(p_T) - 5$. Note the number of total entries in these plots has been normalized to one.	160
14.7 ROC Curve for Quark and Gluon Tagging with a cut on the number of tracks that depends on the $\ln(p_T)$	161
14.8 The top panel shows the distribution of m_{lvqq} with and without quark gluon tagging. The middle panel shows the ratio of the signals and backgrounds with and without quark gluon tagging. The bottom panel shows the change in S/\sqrt{B} with quark gluon tagging.	162
16.1 The top panel shows the distribution of m_{lvqq} with and without requiring jets to be true quarks. The middle panel shows the ratio of the signals and backgrounds with and without requiring jets to be true quarks. The bottom panel shows the change in S/\sqrt{B} when requiring jets to be true quarks.	170
16.2 Unfolded and extracted n_C qg dstbs.	171
16.3 PDGID of the truth-level parton matched to the small-R jets passing the Resolved GGF WW Signal Region selections for the (a) Leading (b) Sub-Leading jets . These distributions are shown for 300, 500, and 700GeV Z' signals and the background.	172

List of Tables

2.1	Representations of the SM fermions under $SU(3)_C \times SU(2)_L \times U(1)_Y$ gauge symmetry group. Rows are correspond to different weak isospin states and columns to different QCD color states.	13
9.1	The list of triggers used in the analysis.	78
9.2	Summary of selection criteria used to define the signal region (SR), W +jets control region (W CR) and $t\bar{t}$ control region ($t\bar{t}$ CR) for merged 1-lepton channel.	87
9.3	The list of selection cuts in the resolved analysis for the WW and WZ signal regions (SR), W +jets control region (WR) and $t\bar{t}$ control region (TR).	88
10.1	Definitions of “inverted” leptons used in multijet control region. For the inverted muon selection, $ptvarcone30$ is given by sum of the p_T of tracks in a cone around the muon candidate divided by the muon p_T . The size of the cone, δR used is $10\text{GeV}/p_T^\mu$ or 0.3, whichever is smaller. So, as the p_T of the muon increases, the cone size used decreases. This is useful as more boosted muons are more likely to be produced in dense environments and using a smaller cone size more accurately determines the quality of the muon.	100

10.2 Fit validation result in WCRs for 2015+16 data. The fit is done in various WCRs, in order to obtain the corresponding scale factors for MJ templates: ggF resolved WCR for the $WW \rightarrow lvqq$ selection, ggF resolved untagged WCR for the $WZ \rightarrow lvqq$ selection, ggF resolved tagged WCR for the $WZ \rightarrow lvqq$ selection, VBF resolved WCR for the $WW \rightarrow lvqq$ selection, and VBF resolved WCR for the $WZ \rightarrow lvqq$ selection. Post-fit event yields for electroweak processes and MJ contributions are shown. The SF column shows the corresponding normalization scale factors for electroweak processes from the fit. R.U. stands for relative uncertainty.	112
13.1 Expected and Measured for DY WW $W+jets$, $t\bar{t}$ control regions and signal regions.	132
13.2 Expected and Measured for DY WZ $W+jets$, $t\bar{t}$ tag and untag control regions.	133
13.3 Expected and Measured for DY WZ $W+jets$, $t\bar{t}$ tag and untag signal regions.	134
13.4 Expected and Measured for VBF WW $W+jets$, $t\bar{t}$ control regions and signal regions.	135
13.5 Expected and Measured for VBF WZ $W+jets$, $t\bar{t}$ control regions and signal regions.	136
13.6 Fitted background normalizations for $t\bar{t}$ and $W+jets$ backgrounds for the DY WW analysis region.	137
13.7 Fitted background normalizations for $t\bar{t}$ and $W+jets$ backgrounds for the DY WZ analysis region.	137
13.8 Fitted background normalizations for $t\bar{t}$ and $W+jets$ backgrounds for the VBF WW analysis region.	137
13.9 Fitted background normalizations for $t\bar{t}$ and $W+jets$ backgrounds for the VBF WZ analysis region.	138

14.1 This table shows the best fit slope and intercept for the 2-d distribution of number of tracks vs. jet $\ln(p_T)$ for the leading jet in the background and HVT Z' samples. The tagging efficiency is shown for the 90% working point in the last column. The background jets contain more gluons than the signal jets. Consequently, the best fit line for the background predicts larger values of the number of tracks in jets for the background than the considered signals. . . . 161

Abstract

Search for WW and WZ Resonances in $\ell\nu qq$ final states in pp collisions at

$\sqrt{s} = 13$ TeV with the ATLAS detector

by

Natasha Woods

This thesis presents a search for WW and WZ resonances using data from pp collisions at $\sqrt{s} = 13$ TeV using the ATLAS detector, corresponding to an integrated luminosity of 139 fb^{-1} . Diboson resonances are predicted in a number of Standard Model (SM) extensions, such as Extended Gauge Models, and Extra dimensional models. This search looks for resonances where one W boson decays leptonically and the other W or Z boson decays hadronically. This search is sensitive to diboson resonance production via vector-boson fusion as well as quark-antiquark annihilation and gluon-gluon fusion mechanisms. No significant excess of events is observed with respect to the Standard Model backgrounds, and constraints on the masses of new W' , Z' , and bulk-RS Gravitons are extended to up to 3.3 TeV, depending on the model. As the dominant backgrounds in this search contain gluons, classifying jets as quark-initiated or gluon-initiated would make this analysis more sensitive to new physics. Towards this end, this thesis provides a calibrated quark-gluon tagger based on the multiplicity of charged particles within a jet.

Loving Dedication

Acknowledgments

Proper acknowledgments of everyone else who helped you graduate. Write later.

Part I

Introduction

³ Chapter 1

⁴ Introduction

⁵ In general, humanity has continually strived to understand the structure and
⁶ dynamics of reality for widely varying reasons. Each academic field uses a spe-
⁷ cific set of concepts and models to describe nature. Physics is one such field,
⁸ that uses mathematical objects to systematically develop testable models about
⁹ the universe. Currently, the most fundamental types particles are fermions and
¹⁰ bosons. Fermions are the particles that make up the "ordinary" matter of the
¹¹ universe, while bosons are the quanta of the fundamental forces. The Standard
¹² Model (SM) of particle physics describes the quantum behavior of three of the
¹³ four fundamental forces: electromagnetic, strong, and weak forces.

¹⁴ The Standard Model has consistently described much of reality to an extreme
¹⁵ degree of accuracy. It has predicted cross sections for strong and electroweak
¹⁶ processes that span over ten orders of magnitude [see Fig. 3.1] and contains no
¹⁷ known logical inconsistencies. Despite the reality of the Standard Model, it still
¹⁸ fails to describe aspects of reality and suffers from aesthetic issues. The SM fails
¹⁹ to account for dark matter, dark energy, neutrino masses, the hierarchy of the
²⁰ fundamental force strengths, and other issues that may have not been noticed
²¹ yet! This incompleteness may indicate that a more fundamental theory exists. It

22 is hoped that such a theory would address the aforementioned phenomena and
23 the ad-hoc structure and parameter values of the SM. In particular the relative
24 scales of the fundamental forces impose oddly fine-tuned SM parameters, unless
25 there is additional structure at higher energies (e.g. between the electroweak and
26 Planck scales). This and other theoretical arguments motivate the search for new
27 physics at the TeV scale. The set of theories that hope to explain more of reality
28 are known as Beyond the Standard Model theories (BSM). Many of these theories,
29 if true, would revolutionize concepts of symmetry and space-time, which would
30 be intrinsically meaningful.

31 To probe the physics at this high energy frontier, physicists often collide ener-
32 getic particles that combine to produce massive particles, such as the Higgs boson
33 and top quark. The more energetic the colliding particles are the more massive
34 produced particles can be. Currently, the world's highest energy particle collider
35 is the Large Hadron Collider (LHC) at the European Organization for Nuclear
36 Research (CERN).

37 This thesis presents a search for WW and WZ resonances using data from pp
38 collisions at $\sqrt{s} = 13$ TeV using the ATLAS detector at CERN, corresponding
39 to an integrated luminosity of 139 fb^{-1} . Diboson resonances are predicted in a
40 number of BSM theories, such as Extended Gauge Models and Extra dimensional
41 models. This search looks for resonances where one W boson decays leptonically
42 and the other W or Z boson decays hadronically. This search is sensitive to
43 diboson resonance production via vector-boson fusion as well as quark-antiquark
44 annihilation and gluon-gluon fusion mechanisms (which will be collectively called
45 non-VBF modes).

46 To search for these new resonances, Monte-Carlo simulations are used to model
47 SM backgrounds and BSM signals. In these simulations, a series of optimized cuts

48 are used to create signal regions (SR) to identify the leptonic and hadronic decay
49 products of the resonance, maximize signal acceptance, and minimize background
50 contamination. In these regions, the resonance mass is calculated as the combined
51 system mass of the leptonic and hadronic system. The expected resonance mass
52 distribution from the simulated backgrounds and anticipated signal are compared
53 to data to search for the existence of these BSM signals (also known as a "bump
54 hunt"). Control regions enriched in the dominant backgrounds, $t\bar{t}$ and $W+\text{jets}$
55 (TCR and WCR, respectively) are constructed to be orthogonal to SRs and used
56 to determine the normalization of the $t\bar{t}$ and $W+\text{jets}$ backgrounds in SRs.

57 The VBF W' and Z' and ggF W' and Z' resonances studied have unique
58 SR and CR selections to maximize analysis sensitivity. RS Graviton signals are
59 probed using the same selections as the ggF Z' signal. Additionally, more mas-
60 sive resonances are more likely to have boosted W/Z bosons. As the boost of
61 the hadronically decaying boson increases the separation of its hadronic decay
62 products decreases. When the hadronically decaying boson has sufficient boost,
63 the two quarks will overlap and not be identified separately. For this reason, a
64 set of "resolved" selections are used when the hadronic decay products are recon-
65 structed separately, and "merged" selections when the decay products overlap and
66 identified as a single object in the event. A W/Z tagger identifies merged jets as
67 originating from a W/Z bosons based on jet substructure and mass cuts. However,
68 the more boosted the jet is the less likely it is to pass the jet substructure cut, due
69 to track merging. Consequently, the merged selection uses a high purity region
70 (HP), which requires that the jet pass both cuts, and low purity (LP) region where
71 the jet can fail the jet substructure cut.

72 The aforementioned SR definitions veto events with b -jets to minimize $t\bar{t}$ con-
73 tamination. However, b -jets are anticipated from W' resonances from the hadron-

74 ically decaying Z boson. To increase the signal acceptance of these resonances,
75 a $Z \rightarrow bb$ tagger is used to construct additional SR and CRs called the "tagged"
76 regions (and "un>tagged" if the event fails the $Z \rightarrow bb$ tagger).

77 For each signal model, the simulated and measured resonance mass distribu-
78 tions in the relevant SR and CRs are combined to construct a likelihood. This
79 likelihood is parameterized by the signal strength parameter, μ and systematic
80 uncertainties of the resonance mass distribution. This likelihood is used to quan-
81 tify the likelihood of a certain signal model given the anticipated backgrounds and
82 measured data.

83 No significant excess of events is observed with respect to the Standard Model
84 backgrounds, and constraints on the masses of new W' , Z' , and bulk-RS Gravi-
85 tons are extended to up to 3.3 TeV, depending on the model. As the dominant
86 backgrounds in this search contain gluons, classifying jets as quark-initiated or
87 gluon-initiated would improve the sensitivity of this analysis to new physics. To-
88 wards this end, this thesis provides a calibrated quark-gluon tagger based on the
89 multiplicity of charged particles within a jet.

90 Part II reviews the SM, its successes and shortcomings, and the aforemen-
91 tioned BSM theories that address the incompleteness of the SM. The structure
92 and performance of the ATLAS detector used is given in Part III. Part IV summa-
93 rizes the search for the diboson resonances using ATLAS data from pp collisions
94 at $\sqrt{s} = 13$ TeV. Finally, Part V examines the prospects for a quark gluon tagger
95 based on the track multiplicity of jets and details the calibration of this tagger.

Part II

96

Theoretical Motivation

97

₉₈ **Chapter 2**

₉₉ **The Standard Model of Particle**

₁₀₀ **Physics**

₁₀₁ **2.1 Introduction**

₁₀₂ By determining the dynamics of the most elementary degrees of freedom, par-
₁₀₃ ticle physics hopes to uncover the fundamental laws of the universe. The definition
₁₀₄ of elementary has evolved through time and currently refers to matter and force
₁₀₅ mediating particles: fermions and bosons, respectively. The Standard Model of
₁₀₆ Particle Physics (SM) describes the quantum behavior of three of the four funda-
₁₀₇ mental forces: weak, strong, and electromagnetic, via boson and fermion interac-
₁₀₈ tions. Gravity is not included in the SM and still under investigation.

₁₀₉ **2.2 Quantum Field Theory**

₁₁₀ In the SM, forces (and particles) are represented as fields. In this context,
₁₁₁ fields are mathematical objects that define a tensor (e.g. scalar, vector, etc) at
₁₁₂ every point on a manifold, here the manifold is space-time. These fields obey laws

₁₁₃ dictated by Quantum Field Theory (QFT). Particles arise naturally in QFT as
₁₁₄ quantized field excitations localized in spacetime.

₁₁₅ According to Noether's theorem, symmetries of a field give rise to conserved
₁₁₆ quantities (e.g. time-translation invariance leads to energy conservation). Often
₁₁₇ in the history of physics, a conserved quantity of a field is found and then the
₁₁₈ underlying symmetry of the field is inferred. Gauge symmetries are symmetries
₁₁₉ among the internal degrees of freedom of the field (components of the tensor),
₁₂₀ which give rise to quantities associated with fields. By specifying the symmetries
₁₂₁ of a system the dynamics and conserved quantities of the system may be succinctly
₁₂₂ defined.

₁₂₃ 2.3 $U(1)_{EM}$ Local Gauge Invariance

₁₂₄ The Lagrangian of Quantum Electrodynamics (QED) describes the electro-
₁₂₅ magnetic force. QED may be derived by requiring local $U(1)_{EM}$ gauge invariance
₁₂₆ of the free dirac fermion Lagrangian, ψ :

$$\mathcal{L} = i\bar{\psi}\gamma^\mu\partial_\mu\psi - m\bar{\psi}\psi \quad (2.1)$$

₁₂₇ This symmetry may be represented as a complex number with unit modulus,
₁₂₈ $e^{i\theta}$. $U(1)$ gauge invariance requires this gauge transformation of ψ will leave the
₁₂₉ Lagrangian unchanged.

$$\psi(x) \rightarrow \psi'(x) = e^{i\theta(x)}\psi(x) \quad (2.2)$$

₁₃₀ NB: This transformation is a local gauge transformation as θ depends on the
₁₃₁ spacetime coordinate.

₁₃₂ By requiring this symmetry of the free Dirac fermion Lagrangian:

$$\mathcal{L} = i\bar{\psi}\gamma^\mu\partial_\mu\psi - m\bar{\psi}\psi \quad (2.3)$$

¹³³ The mass term is unaffected, but the kinetic term is modified due to $\theta(x)$.

$$\mathcal{L} \rightarrow \mathcal{L}' = i\bar{\psi}e^{-i\theta(x)}\gamma^\mu\partial_\mu\psi e^{i\theta(x)} - m\bar{\psi}e^{-i\theta(x)}\psi e^{i\theta(x)} \quad (2.4)$$

¹³⁴

$$= i\bar{\psi}\gamma^\mu(\partial_\mu\psi + i\psi\partial_\mu\theta) - m\bar{\psi}\psi \quad (2.5)$$

¹³⁵ The $\partial_\mu\theta$ terms breaks the gauge invariance of the Lagrangian. By introducing a
¹³⁶ new field, A_μ we can recover the gauge invariance of the derivative. Now redefining
¹³⁷ the derivative as the covariant derivative:

$$D_\mu\psi \equiv (\partial_\mu - iqA_\mu)\psi \quad (2.6)$$

¹³⁸ And letting A_μ transform under $U(1)$ as:

$$A_\mu \rightarrow A_\mu + \delta A_\mu \quad (2.7)$$

¹³⁹ The transformed covariant derivative becomes:

$$D_\mu\psi \rightarrow D_\mu\psi' = (\partial_\mu - iqA_\mu)\psi' \quad (2.8)$$

¹⁴⁰

$$= (\partial_\mu - iq(A_\mu + \delta A_\mu))\psi e^{i\theta} \quad (2.9)$$

¹⁴¹

$$= e^{i\theta}D_\mu + ie^{i\theta}\psi(\partial_\mu\theta - q\delta A_\mu) \quad (2.10)$$

¹⁴² The covariant derivative can be made gauage invariant by setting the last term
¹⁴³ to zero.

$$\delta A_\mu = \frac{1}{q} \partial_\mu \theta \quad (2.11)$$

¹⁴⁴ So now A_μ transforms as:

$$A_\mu \rightarrow A_\mu + \frac{1}{q} \partial_\mu \theta \quad (2.12)$$

¹⁴⁵ Finally, replacing the derivative with the covariant derivative the Dirac La-
¹⁴⁶ grangian we have:

$$\mathcal{L} = i\bar{\psi}\gamma^\mu D_\mu \psi - m\bar{\psi}\psi - \frac{1}{4}F_{\mu\nu}F^{\mu\nu} \quad (2.13)$$

¹⁴⁷

$$= \mathcal{L}_{QED} \quad (2.14)$$

¹⁴⁸ Here $F_{\mu\nu} \equiv \partial_\mu A_\nu - \partial_\nu A_\mu$. This last term in the Lagrangian is the kinetic
¹⁴⁹ energy of the gauge boson field.

¹⁵⁰ So we have derived the QED Lagrangian. By requiring the free Dirac La-
¹⁵¹ grangian to be invariant under local U(1) transformations we have generated a
¹⁵² new gauge boson field, A_μ , which describes the photon. As expected the photon
¹⁵³ interacts with fermions.

¹⁵⁴ Stepping back, a global U(1) gauge symmetry of the free Dirac Lagrangian
¹⁵⁵ implies we cannot measure the absolute phase of a charged particle. A local U(1)
¹⁵⁶ gauge symmetry changes the phase of fields differently across space time. For this
¹⁵⁷ type of transformation to leave the Lagrangian invariant, we had to introduce an
¹⁵⁸ additional field, A_μ , which "communicates" these phase changes across space-time.
¹⁵⁹ In less formal language this effectively means: if the field at one location changes,
¹⁶⁰ this change is conferred to other particles via A_μ .

¹⁶¹ 2.4 Yang-Mills Gauge Theories

¹⁶² Requiring $U(1)_{EM}$ gauge invariance of the free Dirac Lagrangian gave us QED.

¹⁶³ Requiring different gauge symmetries we can derive the structure of other inter-

¹⁶⁴ actions. Any gauge symmetry may be written as:

$$\psi_i \rightarrow \exp(i\theta^a T_{ij}^a) \psi_j \quad (2.15)$$

¹⁶⁵ Here θ is a dimensionless real parameter and T is the generator of the gauge

¹⁶⁶ symmetry group. With this the covariant derivative can be written as:

$$D_\mu \psi_i \equiv \partial_\mu \psi_i + ig A_\mu^a T_{ij}^a \psi_j \quad (2.16)$$

¹⁶⁷ Then the gauge field must transform as:

$$A_\mu^a \rightarrow A_\mu^a - \frac{1}{g} \partial_\mu \theta^a - f^{abc} \theta^b A_\mu^c \quad (2.17)$$

¹⁶⁸ Here f is the structure constant of the gauge group. The field strength tensor

¹⁶⁹ is given by:

$$F_{\mu\nu}^a \equiv \partial_\mu A_\nu^a - \partial_\nu A_\mu^a - g f^{abc} A_\mu^b A_\nu^c \quad (2.18)$$

¹⁷⁰

$$F_{\mu\nu}^a \rightarrow F_{\mu\nu}^a - f^{abc} \theta^b F_{\mu\nu}^c \quad (2.19)$$

¹⁷¹ This gives the Yang-Mills Lagrangian:

$$\mathcal{L}_{YM} = -\frac{1}{4} F_{\mu\nu}^{a\mu\nu} F_{\mu\nu}^a + i \bar{\psi}_i \gamma^\mu D_\mu \psi_i + m \bar{\psi}_i \psi_i \quad (2.20)$$

¹⁷² 2.5 Particles in the Standard Model

¹⁷³ The SM consists of fermions (half-integer spin matter constituents) and bosons
¹⁷⁴ (integer spin force mediators). Fermions are spinor representations of the Poincare
¹⁷⁵ group and can be further separated into leptons and quarks. Bosons are the result
¹⁷⁶ of requiring a particular symmetry among the spinor fields:

$$SU(3)_C \times SU(2)_L \times U(1)_Y \quad (2.21)$$

¹⁷⁷ $SU(3)_C$ is the symmetry group of the strong force and generates eight gluon
¹⁷⁸ fields, G_μ . $SU(2)_L$ is the symmetry group of the Electroweak force and generates
¹⁷⁹ three electroweak boson fields. The mixing of this $SU(2)_L$ and $U(1)_Y$ gives rise
¹⁸⁰ to the photon field, where Y is the weak-hypercharge:

$$Y = 2(Q - T_3) \quad (2.22)$$

¹⁸¹ Q is the electromagnetic charge, and T_3 is the z-component of the weak isospin.
¹⁸² Weak isospin is the charge associated with the $SU(2)_L$ symmetry. The correspond-
¹⁸³ ing covariant derivative is then:

$$D_\mu \phi \equiv (\partial_\mu + ig_1 B_\mu Y_{L/R} + [ig_2 W_\mu^\alpha T^\alpha]_L + [ig_3 G_\mu^\alpha \tau^\alpha]_C) \psi \quad (2.23)$$

¹⁸⁴ It is important to note that the gauge symmetry of the SM yields a particular
¹⁸⁵ structure of the fermion representations. So for a given fermion to interact with
¹⁸⁶ a given gauge field it must have a non-zero corresponding Noether charge for
¹⁸⁷ that gauge symmetry. If the corresponding Noether charge is zero, that fermion
¹⁸⁸ transforms as a singlet and does not participate in that gauge interaction.

¹⁸⁹ Fermions are divided into quarks and leptons based on their transformations
¹⁹⁰ under $SU(3)_C$. Quarks transform as color triplets. Leptons transform as color

singlets and consequently do not interact with gluons. Fermions may be further
 classified by their $SU(2)_L$ interactions. Only the left-chiral part of fermions (denoted by L here) transform as $SU(2)_L$ doublets, the right-chiral part forms singlets under this gauge. Lastly, all these groups of particles come in three generations, each a heavier copy of the previous, but with differing flavor quantum numbers.
 This is summarized in Table 2.1 and shown in Figures 2.1 and 2.2.

SM Fermion Gauge Group	First Generation	Second Generation	Third Generation	$(SU(3)_C, SU(2)_L, U(1)_Y)$ Representations
Left-handed quarks	$\begin{pmatrix} u_L^r & u_L^g & u_L^b \\ d_L^r & d_L^g & d_L^b \end{pmatrix}$	$\begin{pmatrix} c_L^r & c_L^g & c_L^b \\ s_L^r & s_L^g & s_L^b \end{pmatrix}$	$\begin{pmatrix} t_L^r & t_L^g & t_L^b \\ b_L^r & b_L^g & b_L^b \end{pmatrix}$	$(3, 2, \frac{1}{6})$
Right-handed quarks	(u_R^r, u_R^g, u_R^b) (d_R^r, d_R^g, d_R^b)	(c_R^r, c_R^g, c_R^b) (s_R^r, s_R^g, s_R^b)	(t_R^r, t_R^g, t_R^b) (b_R^r, b_R^g, b_R^b)	$(3, 1, \frac{2}{3})$ $(3, 1, -\frac{1}{3})$
Left-handed leptons	$\begin{pmatrix} \nu_e^L \\ e_L \end{pmatrix}$	$\begin{pmatrix} \mu_e^L \\ \mu_L \end{pmatrix}$	$\begin{pmatrix} \tau_e^L \\ \tau_L \end{pmatrix}$	$(1, 2, -\frac{1}{2})$
Right-handed leptons	e_R	μ_R	τ_R	$(1, 1, -1)$

Table 2.1: Representations of the SM fermions under $SU(3)_C \times SU(2)_L \times U(1)_Y$ gauge symmetry group. Rows are correspond to different weak isospin states and columns to different QCD color states.

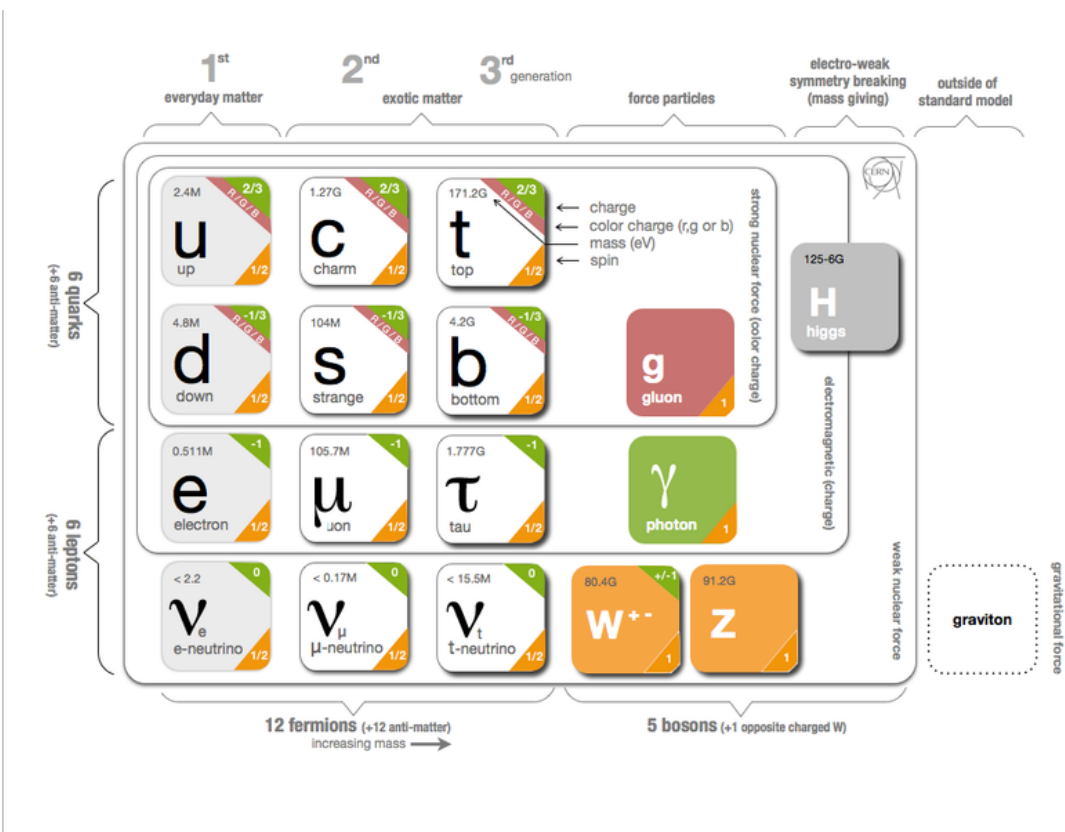


Figure 2.1: The particles of the Standard Model.

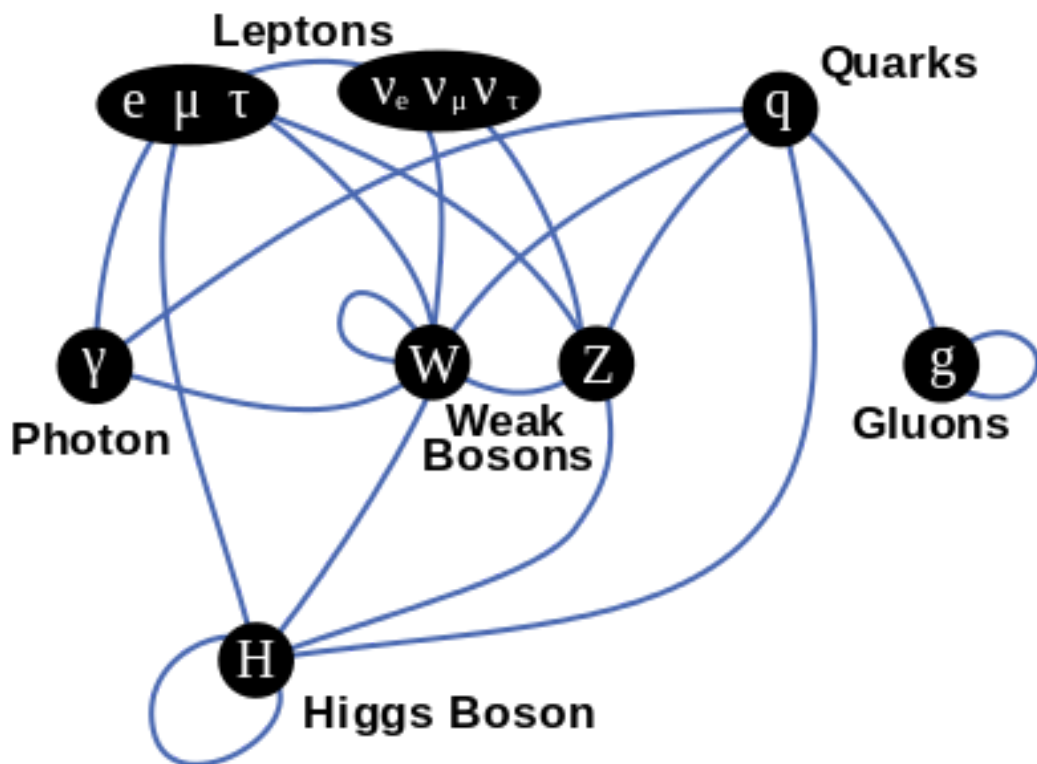


Figure 2.2: Summary of how Standard Model particles interact with other Standard Model particles.

197 Now we can understand the SM Lagrangian density as a Yang-Mills theory
 198 with the gauge group: $SU(3)_C \times SU(2)_L \times U(1)_Y$ with an additional $SU(2)$ complex
 199 scalar Higgs field doublet that will be discussed later.

$$\begin{aligned} \mathcal{L}_{SM} = & \underbrace{-\frac{1}{4}B_{\mu\nu}B^{\mu\nu} - \frac{1}{4}W_{\mu\nu}^a W^{a\mu\nu} - \frac{1}{4}G_{\mu\nu}^\alpha G^{\alpha\mu\nu}}_{\text{Kinetic Energies and Self-Interactions of Gauge Bosons}} \\ & + \underbrace{\bar{L}_i \gamma^\mu (i\partial_\mu - \frac{1}{2}g_1 Y_{iL} B_\mu - \frac{1}{2}g_2 \sigma^a W_\mu^a) L_i}_{\text{Kinetic Energies and EW Interactions of Left-handed Fermions}} \\ & + \underbrace{\bar{R}_i \gamma^\mu (i\partial_\mu - \frac{1}{2}g_1 Y_{iR} B_\mu) R_i}_{\text{Kinetic Energies and EW Interactions of Right-Handed Fermions}} \\ & + \underbrace{\frac{ig_3}{2} \bar{Q}_j \gamma^\mu \lambda^\alpha G_\mu^\alpha Q_j}_{\text{Strong Interactions between Quarks and Gluons}} \\ & + \underbrace{\frac{1}{2} |(i\partial_\mu - \frac{1}{2}g_1 B_\mu - \frac{1}{2}g_2 \sigma^a W_\mu^a)\Phi|^2 - V(\Phi)}_{\text{Electroweak Boson Masses and Higgs Couplings}} \\ & - \underbrace{(y_{kl}^d \bar{L}_k \Phi R_l + y_{kl}^u \bar{R}_k \tilde{\Phi} L_l + h.c.)}_{\text{Fermion Mass terms and Higgs Couplings}} \end{aligned}$$

200 Here several abstract spaces are being spanned:

- 201 – a spans the three $SU(2)_L$ gauge fields with generators expanded in Pauli
 202 matrices, $T^\alpha = \frac{1}{2}\sigma^\alpha$
- 203 – α spans the eight $SU(3)_C$ gauge fields, with generators expanded in Gell-
 204 Mann matrices, $\tau^\alpha = \frac{1}{2}\lambda^\alpha$
- 205 – L/R represent left and right projections of Dirac fermion fields. The Strong
 206 interaction is not chiral, so $Q = L+R$

- 207 – μ and ν are four-vector indices
- 208 – i, j, k are summed over the three generations of SM particles.

209 2.6 Higgs Mechanism

210 The SM Lagrangian without the addition of a Higgs field does not allow for
211 gauge boson and fermion mass terms: $\frac{1}{2}m_A^2 A_\mu A_\mu$ and $m(\bar{\psi}\psi)$, as these terms are
212 not gauge invariant. By introducing the Higgs field, mass terms for these particles
213 may be included in a gauge invariant way. This field is a complex doublet with a
214 potential $V(\Phi)$:

$$\Psi = \begin{pmatrix} \Phi^\dagger \\ \Phi^0 \end{pmatrix} \quad (2.24)$$

215

$$V(\Phi) = \mu^2 \Phi^\dagger \Phi + \lambda |\Phi^\dagger \Phi|^2 \quad (2.25)$$

216 The minima of this field occurs for $|\Phi| = \sqrt{\frac{\mu^2}{2\lambda}} \equiv \frac{v}{2}$. This yields degenerate
217 minima, this symmetry is broken by choosing a specific minima (a.k.a. sponta-
218 neous symmetry breaking). By convention $\Phi_{min} = \frac{1}{\sqrt{2}} \begin{pmatrix} 0 \\ v \end{pmatrix}$ is chosen. This means
219 the ground state of the Higgs field (Higgs vacuum) is non-zero, $\sqrt{\frac{-\mu^2}{\lambda}}$. The Higgs
220 Field may now be expanded around this new ground state:

$$\Phi(x) = \frac{1}{\sqrt{2}} \begin{pmatrix} 0 \\ v + h(x) \end{pmatrix} \quad (2.26)$$

221 This non-zero Higgs vacuum now generates mass terms for the gauge bosons
222 from the following term in the Lagrangian:

$$|(-\frac{1}{2}g_1B_\mu - \frac{1}{2}g_2\sigma^aW_\mu^a)\Phi|^2 = \frac{1}{2}m_W^2W_\mu^+W^{-\mu} + \frac{1}{2}m_Z^2Z_\mu Z^\mu \quad (2.27)$$

223 where:

$$W_\mu^\pm \equiv \frac{1}{\sqrt{2}}(W_\mu^1 \mp iW_\mu^2) \quad (2.28)$$

$$\begin{aligned} \text{224} \quad Z_\mu &\equiv \frac{1}{\sqrt{g_1^2 + g_2^2}}(g_2W_\mu^2 - g_1B_\mu) \end{aligned} \quad (2.29)$$

$$\begin{aligned} \text{225} \quad m_W &= \frac{vg_2}{\sqrt{2}} \end{aligned} \quad (2.30)$$

$$\begin{aligned} \text{226} \quad m_Z &= \frac{v}{\sqrt{2}}\sqrt{g_1^2 + g_2^2} \end{aligned} \quad (2.31)$$

227 The Higgs field also generates a mass term for the Higgs boson and self-
228 interactions for the Higgs boson.

229 2.7 Electroweak Theory

230 $SU(2)_L$ generates W^\pm, W^0 gauge bosons, which would be massless if $SU(2)_L$
231 was a perfect symmetry. These bosons are massive as this symmetry is broken.

232 The mass eigenstates, Z and γ given by:

$$\begin{pmatrix} Z_\mu \\ A_\mu \end{pmatrix} = \begin{pmatrix} \cos\theta_W & -\sin\theta_W \\ \sin\theta_W & \cos\theta_W \end{pmatrix} \begin{pmatrix} W_\mu^3 \\ B_\mu \end{pmatrix} \quad (2.32)$$

233 Here θ_W is the Weinberg angle given by:

$$\cos\theta_W = \frac{g_2}{\sqrt{g_1^2 + g_2^2}} = \frac{m_W}{m_Z} \quad (2.33)$$

²³⁴ 2.8 Quantum ChromoDynamics

²³⁵ As mentioned earlier the Strong Force, which binds the proton together, is
²³⁶ mediated by gluons. Quantum Chromodynamics is the QFT which describes the
²³⁷ interactions of quarks and gluons via $SU(3)_C$ symmetry. QCD contains features
²³⁸ not present in Electroweak Interactions due to $SU(3)_C$ generators not commuting
²³⁹ (a.k.a. $SU(3)_C$ is a non-abelian group) and the number of quark flavors (n_f).
²⁴⁰ For example, in QCD there is color confinement and asymptotic freedom due to
²⁴¹ the structure constants being non-zero. Requiring $SU(3)_C$ local gauge invariance
²⁴² implies:

$$\psi(x) \rightarrow \psi(x)' = \exp[i g_S \alpha(x) \cdot \hat{T}] \psi(x) \quad (2.34)$$

²⁴³ where $\alpha(x)$ is the local phase function, g_S is the strong coupling constant, and
²⁴⁴ \hat{T} are the eight generators of $SU(3)$ (note $\hat{T}^a = \frac{1}{2}\lambda^a a$, where λ^a are the Gell-Mann
²⁴⁵ matrices). As the Gell-Mann matrices are 3x3, this means ψ has three degrees of
²⁴⁶ freedom under these $SU(3)$ rotations. So we represent ψ under $SU(3)$ rotations
²⁴⁷ as:

$$\psi = \begin{pmatrix} \psi_{red} \\ \psi_{green} \\ \psi_{blue} \end{pmatrix} \quad (2.35)$$

²⁴⁸ Consequently, particle fields transforming under $SU(3)$ rotations have three
²⁴⁹ components which physicists describe as color components (red, green, and blue).
²⁵⁰ A particle's corresponding antiparticle has the corresponding anticolor. This color
²⁵¹ is the "charge" of QCD and is conserved under $SU(3)$ rotations. Combining colors,
²⁵² color neutral states (e.g. red and antired, or red, green and blue) may be created.
²⁵³ For the free Dirac Lagrangian to remain invariant under $SU(3)$ transformations,

254 we must again postulate a boson field that modifies the derivative. The gluon
255 field tensor is given by ($\alpha = 1, \dots, 8$):

$$G_{\mu\nu}^k = \partial^\mu G_\alpha^\nu - \partial^\nu G_\alpha^\mu - g_S f^{\alpha\beta\gamma} G_\beta^\mu G_\gamma^\nu \quad (2.36)$$

256 Here $f^{\alpha\beta\gamma}$ are the structure constants of $SU(3)$. Combining all this gives the
257 QCD Lagrangian:

$$\mathcal{L}_{QCD} = \bar{\psi}_q i\gamma^\mu (D_\mu)_{ij} \psi^{qj} - m \bar{\psi}_q \psi_q - \frac{1}{4} G_{\mu\nu}^\alpha G^{\alpha\mu\nu} \quad (2.37)$$

258 Here i are the color indices, and q are the quark flavors. It is important to
259 note that quarks transform under the fundamental representation of $SU(3)$, while
260 gluons transform under the adjoint representation. This means quarks carry a
261 single color charge (red, green, blue, antired, antigreen, antiblue) and gluons carry
262 a color and anticolor charge.

263 Figure 2.3 shows the three dominant QCD interactions. Since gluons carry
264 color charge, they interact with one another. This does not occur in QED, as
265 photons do not have electric charge and therefore do not interact with each other.
266 In QED, a bare electron's effective charge is largest closest to the electron and
267 decreases as a function of distance. This is because the QED vacuum fills with
268 particle antiparticle pairs spontaneously, which screen the charge of the bare elec-
269 tron. The larger the distance from the electron, the smaller the effective charge
270 and therefore the weaker the force.

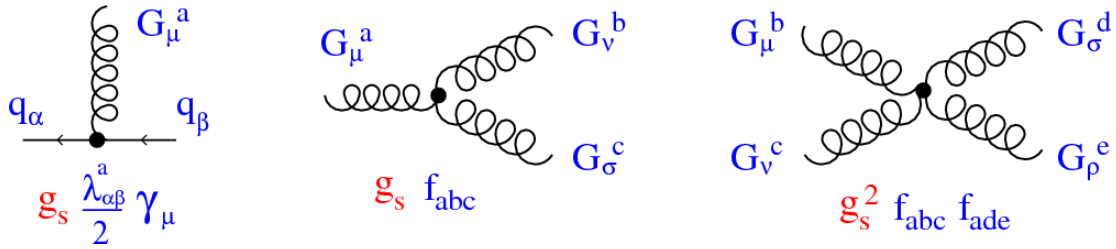


Figure 2.3: This figure shows the three dominant QCD interactions. From Ref. [20]

271 As the distance from a quark increases it's effective color charge increases due
 272 to the vacuum polarization in QCD. Color charge grows as the distance from
 273 the source increases (a.k.a. color is anti-screened in QCD). In this way, strong
 274 interactions become stronger at large distances (low momenta interactions). At
 275 small distances (large momenta interactions) strong interactions are significantly
 276 weaker and considered nearly free. This effect of referred to as asymptotic freedom.
 277 At large distances, a quark's effective charge is large and the strong force is more
 278 significant. This force becomes so strong that quarks form colorless bound states
 279 instead of remaining free particles. This effect is known as color confinement.
 280 This running of all SM fields is shown in Figure 2.4.

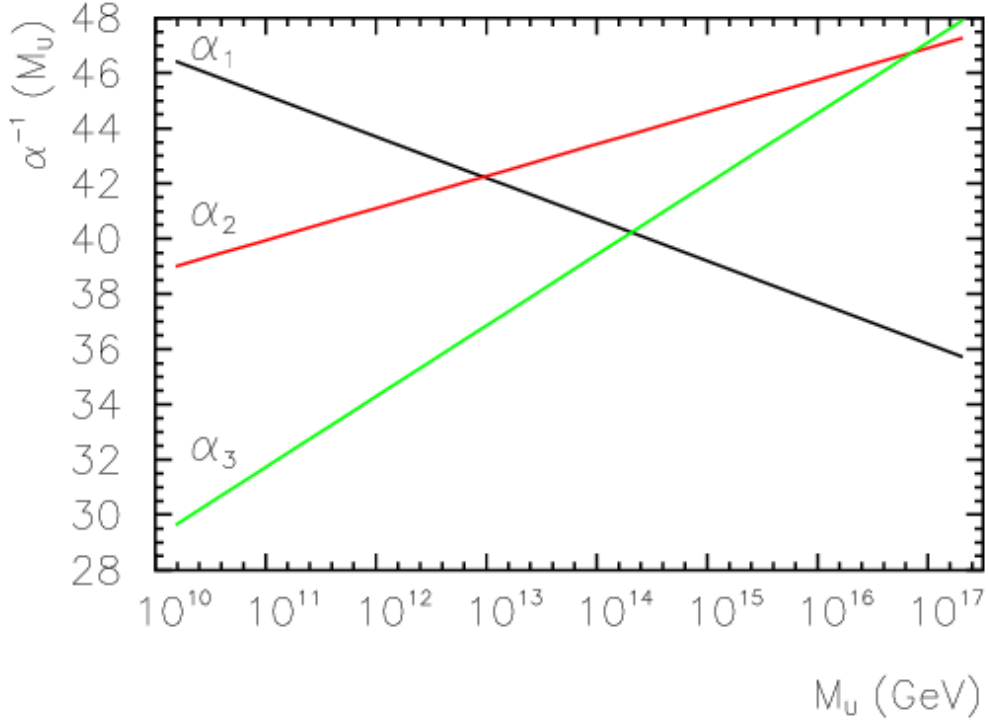


Figure 2.4: Strength of the U(1), SU(2), and SU(3) gauge couplings as a function of the energy scale of the interaction (Q). From Ref. [14]

Commonly the change in a particle's effective charge under a given force is quantified with $\beta(r) \equiv -\frac{de(r)}{d\ln r}$, where $e(r)$ is the effective charge of a given particle under a force. In QED this function is positive but in QCD this function is negative leading to confinement and asymptotic freedom. Moreover, one can calculate how the coupling (α) of a force varies with energies. (More deeply this amounts to incorporating renormalization and vacuum polarization in the boson propagators). For QCD this is:

$$\alpha_s(Q^2) = \frac{\alpha_s(\mu^2)}{1 + \frac{\alpha_s(\mu^2)}{12\pi}(33 - 2n_f)\ln(Q^2/\mu^2)} \quad (2.38)$$

where Q is the momentum of the force is probed at, μ^2 is the renormaliza-

tion scale, n_f is the number of quark flavors. There are six quark flavors in SM QCD, making $33 - 2n_f > 0$. This factor being positive and the $\ln(Q^2/\mu^2)$ being in the denominator means that as Q^2 increases α_s decreases. So for large Q^2 , α_s is small and SM QCD is asymptotically free, while for small Q^2 , α_s is large and SM QCD is confined, as mentioned earlier.

As stated previously, quarks and gluons have not been observed in isolation. Instead they form bound colorless states. Hadronization is the process by which quarks and gluons form hadrons. The process of hadronization is still an active area of research. One qualitative description is show in Figure 2.5. In this figure, as two quarks separate the color field between them is restricted to a tube with energy density of $1\text{GeV}/\text{fm}$. As they separate further, the energy in the color field increases, until there is enough energy to produce $q\bar{q}$ pairs, which breaks the color field. This process repeats until quarks and antiquarks have low enough energy to form colorless hadrons. The resulting spray of hadrons is called a jet.

Since quarks and gluons carry different color charges, their respective jets have different properties. As quarks carry only a single color charge (vs. gluons which have color and anticolor charge), so their jets have less constituent particles. More precisely, the Altarelli-Parisi splitting functions [3] contain a factor C_A for gluon radiation off a gluon and C_F for gluon radiation off a quark ($C_A/C_F = 9/4$). These color factors are the prefactor in the Feynman diagrams for these processes [1], which leads to gluon jets having more constituents and therefore more tracks than quark jets. Gluon jets also tend to have a larger radius with lower momentum constituents than quarks. There are many novel techniques to distinguish quarks from gluons. For this study the number of charged particles will be focused on.

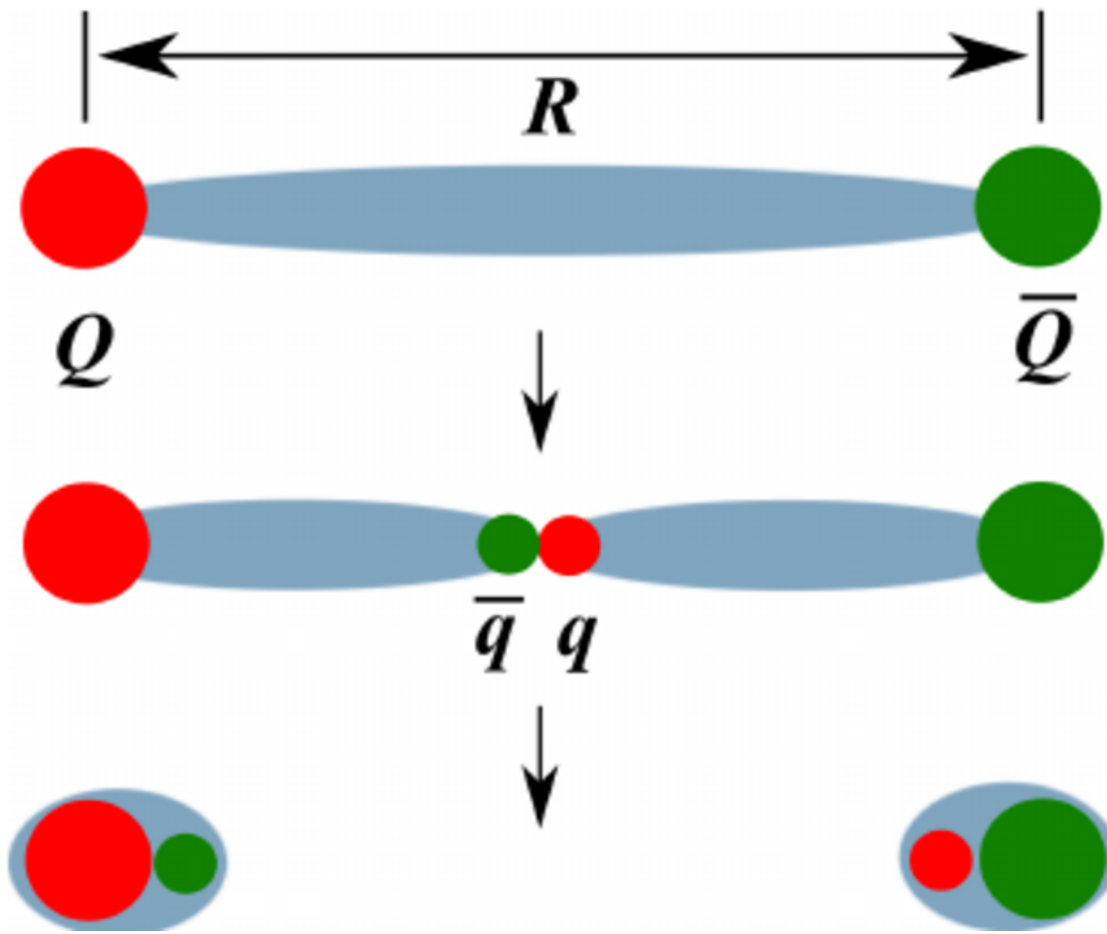


Figure 2.5: A cartoon of string breaking: the QCD string spanned between quark Q and antiquark \bar{Q} breaks due to $q\bar{q}$ creation [5]

³¹³ **Chapter 3**

³¹⁴ **Standard Model Successes and**

³¹⁵ **Limitations**

³¹⁶ The Standard Model has accurately described most of the underlying principles
³¹⁷ of nature. It has predicted cross sections for strong and electroweak processes that
³¹⁸ span over ten orders of magnitude correctly [see Fig. 3.1] and contains no known
³¹⁹ logical inconsistencies. Despite the strength and reality of the Standard Model, it
³²⁰ still fails to describe some important aspects of reality and suffers from aesthetic
³²¹ issues. To date, dark matter and dark energy comprise $\sim 95\%$ of the universe, but
³²² the SM offers no explanation of their nature. Additionally, neutrinos are known
³²³ to have mass, but the SM offers no mass generation mechanism for left-handed
³²⁴ neutrinos without right-handed neutrinos (which do not exist). There are other
³²⁵ mechanisms for introducing massive neutrinos in the SM, but these mechanisms
³²⁶ create hierarchy problems.

³²⁷ Possibly the most significant aesthetic issue is the hierarchy between the elec-
³²⁸ troweak and Planck scales. The electroweak scale is the scale of electroweak
³²⁹ symmetry breaking. The Planck scale is the scale where the gravitational force
³³⁰ is comparable in strength to the other forces. The Planck scale is where the SM

331 breaks down, as there is not an experimentally verified theory of quantum gravity,
332 and at this scale gravity cannot be ignored (like it can at the electro-weak scale).
333 These scales differ by ~ 30 orders of magnitude. Understanding the difference
334 in these energy scales may help explain the weakness of gravity at electroweak
335 scales, and possibly a QFT for gravity. (NB: This hierarchy can also be framed in
336 terms of the corrections to the Higgs mass, which depend on the UV cutoff scale -
337 where the SM is suppose to break, which is taken at the Planck scale. This leads
338 the quantum corrections to the Higgs mass that would force the Higgs mass to
339 $\sim 10^{18}$ TeV.)

340 These stark contrasts in scales may indicate that a more fundamental theory
341 exists. It is hoped that such a theory would explain and motivate some of the
342 ad-hoc features of the SM. In particular, the values of the 19 SM parameters (6
343 quark masses, 3 charged lepton masses, 3 gauge couplings, Higgs parameters (μ^2 ,
344 λ)), the structure of the fermion representations, etc.

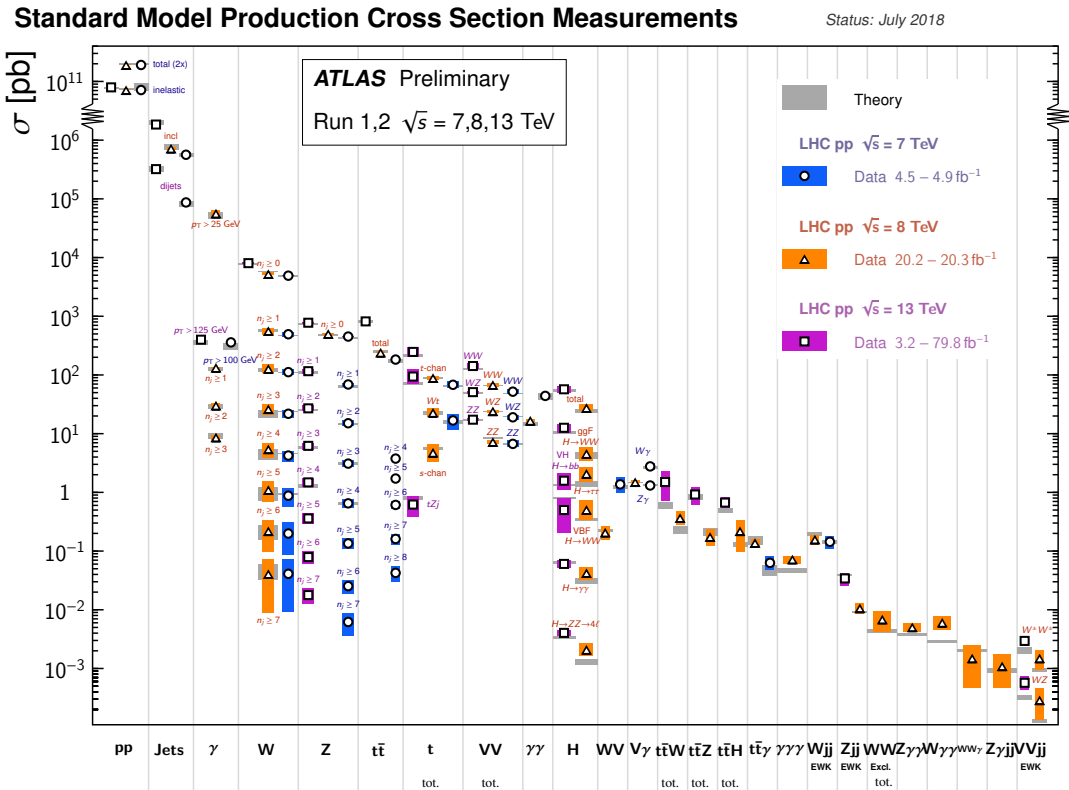


Figure 3.1: A comparison of cross section measurements at $\sqrt{s} = 7,8,13$ TeV from ATLAS compared to theoretical measurements. From Ref. [7]

³⁴⁵ **Chapter 4**

³⁴⁶ **New Physics Models with
347 Diboson Resonances**

³⁴⁸ **4.1 Randall Sundrum Bulk Model**

³⁴⁹ The electroweak-planck hierarchy may be explained by the existence of extra
³⁵⁰ dimensions, like the 5D Randall Sundrum Bulk Model ([21], [2]). In this model,
³⁵¹ there is one extra warped spatial dimension, y , with a metric:

$$ds^2 = e^{-2k|y|} \eta_{\mu\nu} dx^\mu dx^\nu + dy^2 \quad (4.1)$$

³⁵² where $e^{-k|y|}$ is the warp factor of the extra dimension, which is compactified on
³⁵³ a S^1/Z_2 orbifold (a.k.a. a circle where $y \rightarrow -y$). This can be visualized as every
³⁵⁴ point in space time having a line extending from it a distance L , representing
³⁵⁵ this fifth dimension. At the end of this line is the Planck brane. This fourth
³⁵⁶ spatial dimension separates two 4-D branes: Planck brane and TeV brane. We
³⁵⁷ live on the TeV brane, as shown in Figure 4.1. The Higgs field (and to a lesser
³⁵⁸ degree the top quark and graviton fields) is localized near the TeV Brane, while

359 the light fermion fields are localized more near the Planck brane. Fundamental
 360 parameters are set on the Planck brane. The warp factor may be scaled away from
 361 all dimensionless SM terms by field redefinitions. However, the only dimensionful
 362 parameter, $m_H^2 = v^2$ is rescaled by $\tilde{v} \sim e^{-kL} M_{Pl} \sim 1\text{TeV}$ for $kL \sim 35$, explaining
 363 why gravity is so weak on the TeV brane. Also, by localizing the light fermion
 364 fields near the Planck brane and top and graviton fields near the TeV brane, the
 365 light quarks will have smaller masses.

366 The two free parameters of this theory are M_{Pl} and k . Based on this RS Bulk
 367 model, all SM particles should have Kaluza-Klein (KK) excitations. In particular,
 368 the graviton would have KK excitations that prefer to decay to WW or ZZ, which
 369 is why this analysis searches for RS Gravitons.

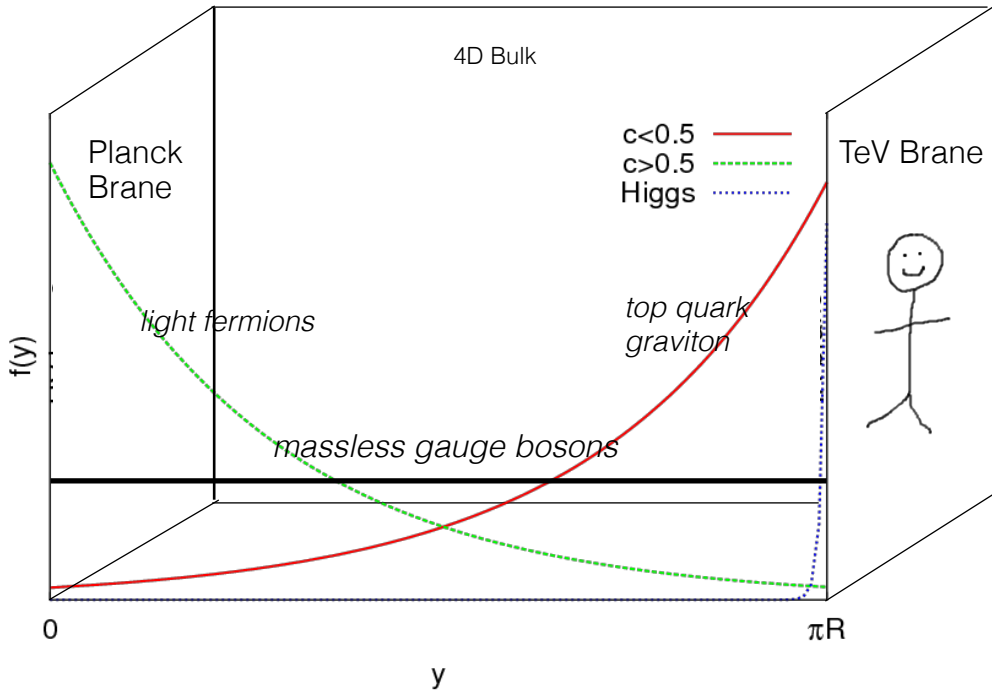


Figure 4.1: Cartoon of RS Bulk Model

³⁷⁰ 4.2 Simple Standard Model Extensions

³⁷¹ The RS Bulk model is motivated by resolving SM hierarchies, but it does not
³⁷² address all of the other SM issues. There are many other interesting and well
³⁷³ motivated new physics frameworks that address these issues, but there is a lack
³⁷⁴ of completely predictive models, due to model flexibility (free parameters). It is
³⁷⁵ difficult for experimentalists to know which theories to search for in data. There-
³⁷⁶ fore, developing a model-independent resonance search that can be reinterperted
³⁷⁷ in the context of a given BSM theory is ideal.

³⁷⁸ This search is sensitive to the resonance mass and its interactions, but not
³⁷⁹ all of a given BSM model's parameters. Therefore, the BSM Lagrangian may be
³⁸⁰ reduced to only retain this information (mass parameters and couplings) following
³⁸¹ the procedure in [19]. In this simplified approach, the new resonance searched for
³⁸² is represented as an additional heavy vector triplet (HVT), which is a real vector
³⁸³ field in the adjoint representation of $SU(2)_L$ with vanishing hypercharge. This
³⁸⁴ results in one neutral and two charged bosons, defined as:

$$\begin{aligned} V^\pm &= \frac{V_\mu^1 \mp iV_\mu^2}{\sqrt{2}} \end{aligned} \tag{4.2}$$

$$V_\mu^0 = V_\mu^3 \tag{4.3}$$

³⁸⁶ The SM Lagrangian is then augmented with the additional terms:

$$\mathcal{L} \supset -\frac{1}{4}D_{[\mu}V_{\nu]}^a D^{[\mu}V^{\nu]}_a + \frac{m_V^2}{2}V_\mu^a V^{a\mu} + ig_V c_H V_\mu^a H^\dagger \tau^a \overset{\leftrightarrow}{D}^\mu H + \frac{g^2}{g_V} c_F V_\mu^a J_F^{\mu a} \tag{4.4}$$

³⁸⁷ In order the terms represent: the kinetic, V mass, Higgs- V interaction, and
³⁸⁸ V -left-handed fermion interaction terms. The g_V coupling factor determines the
³⁸⁹ coupling of the new resonance to left-handed fermions and the Higgs boson.

390 As benchmark models, this search considers resonances from extended gauge
391 symmetry (EGM) and composite Higgs models as discussed in [19] . The EGM
392 model predicts weakly coupled resonances, where $g_V = 1$, referred to later as
393 Model A. The composite Higgs Model is a strongly coupled model, where $g_V = 3$,
394 and later referred to as Model B. As shown in Eq. 4.4, the coupling of these
395 resonances to fermions scales as $g_f = g^2 c_F / g_V$, where g is the SM $SU(2)_L$ gauge
396 coupling and c_F is a free parameter. This then means that for Model B the
397 coupling to fermions is suppressed relative to Model A, leading to a smaller DY
398 production rate and branching ratio (BR) to fermionic final states. The coupling
399 of V to SM bosons scales as $g_H = g_V c_H$, where c_H is a free parameter on the
400 order of one for Model A and B. Consequently Model A resonances have a smaller
401 the BR to gauge bosons than Model B. For the pp collision data used, Model A
402 predicts larger production cross sections decaying to leptons and fermions than
403 Model B which decays primarily to gauge bosons.

404 Model A and B vectors are produced via quark-anti-quark annihilation and
405 the more rare vector-boson-fusion is considered by setting $g_H = 1$ and $g_F = 0$.
406 Both production modes are probed in this resonance search.

407 In summary, V couples most strongly to left-handed fermions and VV depen-
408 dent on g_V .

Part III

409

Experimental Setup

410

⁴¹¹ **Chapter 5**

⁴¹² **LHC**

⁴¹³ The Large Hadron Collider (LHC) is the highest-energy particle collider in the
⁴¹⁴ world. It was designed to expand the frontier of high energy particle collisions in
⁴¹⁵ energy and luminosity. This enables LHC experiments to test the Standard Model
⁴¹⁶ and search for new physics at higher energies than tested with previous colliders.
⁴¹⁷ Collisions at higher energies not only produce more massive particles but also
⁴¹⁸ more weakly interacting particles. Fig. 5.1 shows production cross sections for
⁴¹⁹ various processes at hadron colliders. The rate for electroweak physics processes
⁴²⁰ including W and Z scale with the center-of-momentum energy, \sqrt{s} .

⁴²¹ The LHC consists of a 26.7 km (17 miles) ring, approximately 100 m un-
⁴²² derground, outside Geneva, Switzerland. Counter-circulating proton (and occa-
⁴²³ sionally heavy ions) beams collide inside four experiments along the beam line:
⁴²⁴ ATLAS, CMS, LHCb, ALICE. ATLAS and CMS are general purpose detectors de-
⁴²⁵ signed to explore the high energy frontier. LHCb is designed to study the physics
⁴²⁶ of b -quarks. ALICE specializes in studying heavy ion collisions.

proton - (anti)proton cross sections

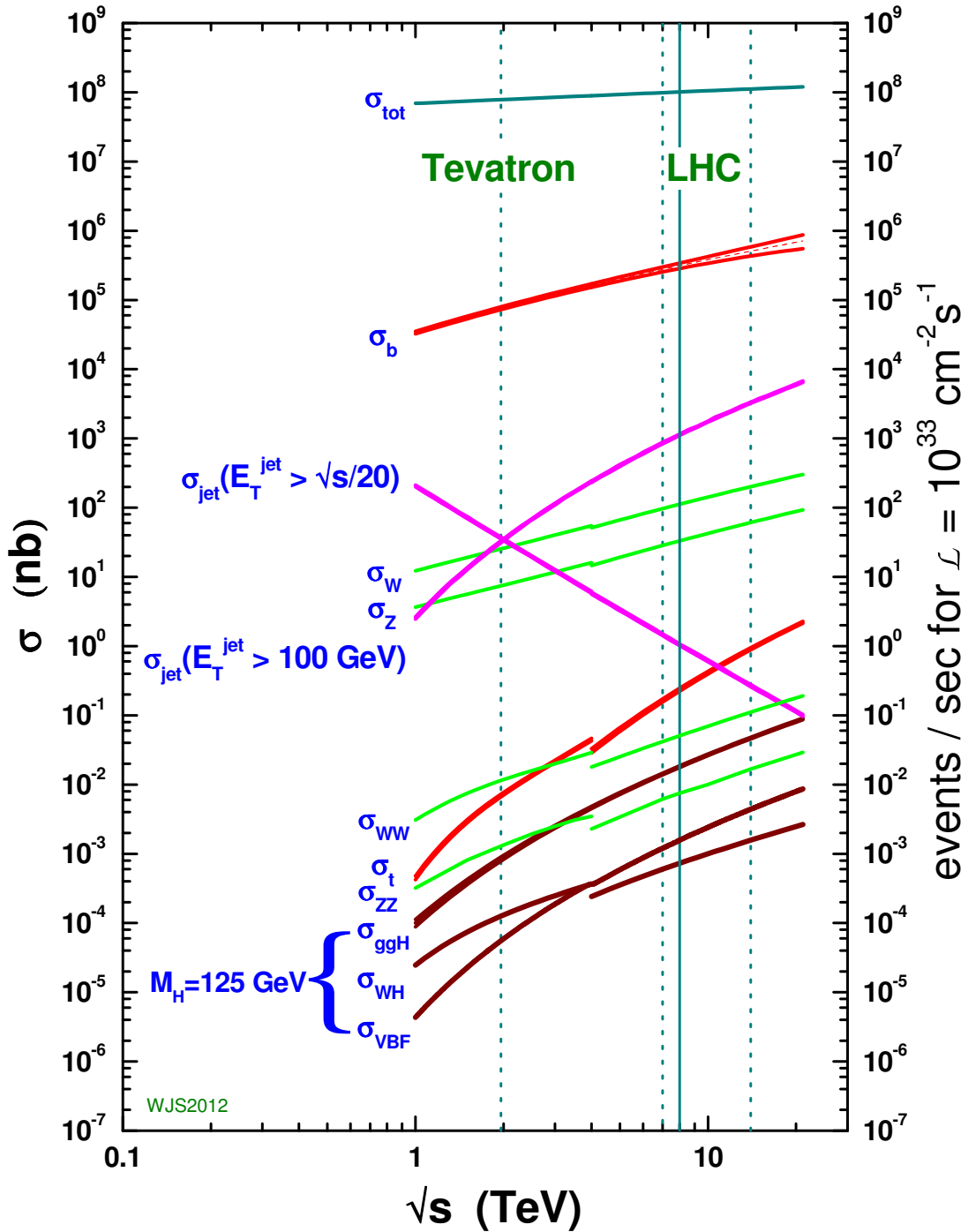


Figure 5.1: Scaling of various SM cross sections with \sqrt{s} .

427 The first proton beams circulated in September, 2008. Nine days later an elec-
428 trical fault lead to mechanical damage and liquid helium leaks in the collider. This
429 incident delayed further operation until November 2009, when the LHC became
430 the world's highest energy particle collider, at 1.18TeV per beam. This first oper-
431 ational run continued until 2013, reaching 7 and 8 TeV collision energies. During
432 this run a particle with properties consistent with the Standard Model Higgs bo-
433 son was discovered. The next run began after a two year shutdown after upgrades
434 to the LHC and experiments. This run lasted from 2013 to 2018 reaching 13 TeV
435 collision energies. This analysis uses data from the second operational run.

436 5.1 LHC Layout and Design

437 The layout of the LHC is shown in Figure 5.2. The red and blue lines in the
438 figure represent the counter-circulating proton beams. The LHC is divided into
439 eight octants. Octant 4 contains the RF cavities that accelerate the protons and
440 octant 6 contains the beam dump system. Octants 3 and 7 house the collimation
441 systems for beam cleaning. The beams collide inside the four aforementioned
442 experiments. Each octant contains a curved and straight section. The LHC
443 magnets are built with NbTi superconductors cooled with super-fluid Helium to
444 2K, creating a 8.3T magnetic field to bend the proton beams.

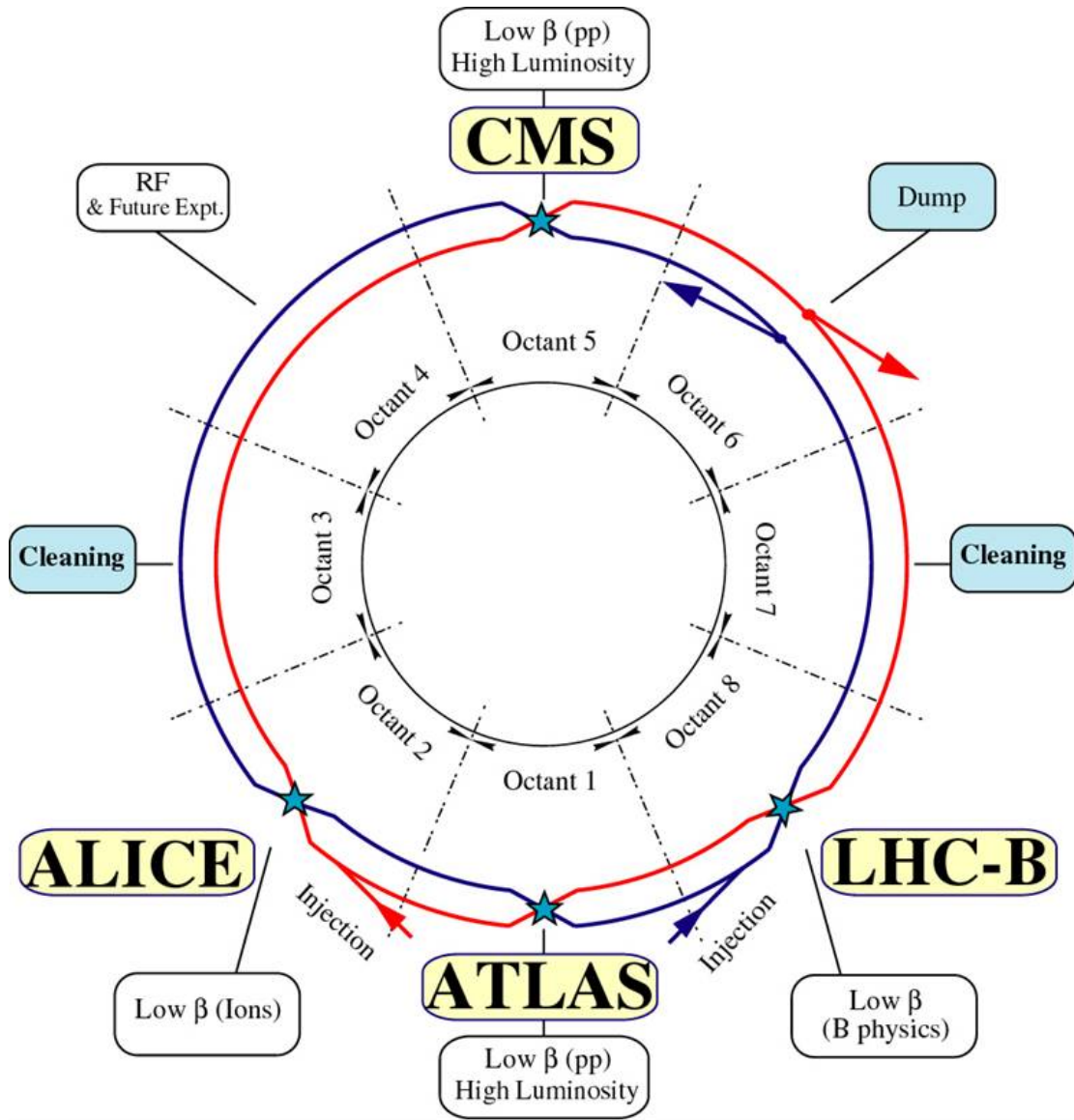


Figure 5.2: The layout of the LHC and the four detectors along the beam line (ATLAS, LHCb, ALICE, CMS).

Four sequential particle accelerators are used to accelerate protons from rest as shown in Figure 5.3. First, Hydrogen gas is ionized to produce protons which are then accelerated to 50 MeV using Linac 2, a linear accelerator. The resulting proton beam is then passed to three circular particle accelerators: Proton Synchrotron Booster, Proton Synchrotron, and Super Proton Synchrotron (SPS),

450 accelerating protons to 1.4, 25, and 450 GeV, respectively. Once the protons exit
 451 the SPS, they are injected into the LHC at octant 2 and 8. Each proton bunch
 452 contains $\sim 10^{11}$ protons. The spacing between bunches is 25 ns, which means
 453 each beam contains 3564 bunches. However, some bunches are left empty due
 454 to injection and safety requirements, yielding 2808 bunches per beam. Once the
 455 proton beams are injected they are accelerated to 13 TeV.

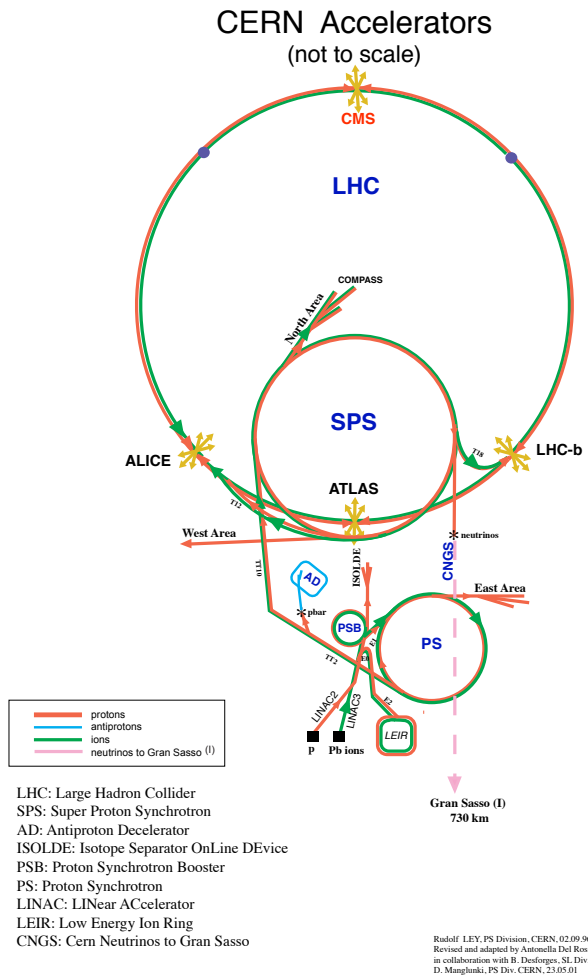


Figure 5.3: An overview schematic of the LHC accelerator subsystems.

456 As many new physics models predict cross-sections below the weak scale it was
 457 important to design the LHC to be capable of collecting enough data, by running

458 in high luminosity conditions. The machine luminosity depends only on beam
459 parameters:

$$L = \frac{N_p^2 f}{4\epsilon\beta^*} F \quad (5.1)$$

460 where N_p is the number of protons per bunch, f is the bunch crossing frequency,
461 ϵ is the transverse beam emittance, β^* is the amplitude function at the collision
462 point, and F is the geometric luminosity reduction factor due to the beams crossing
463 at an angle (rather than head-on).

464 **Chapter 6**

465 **The ATLAS Detector**

466 The ATLAS detector measures the position, momentum and energy of parti-
467 cles produced in the proton collisions by using magnetic fields, silicon detectors,
468 sampling calorimeters, and gaseous wire detectors. It is located approximately
469 100 m underground at Point-1 around the LHC beam line and weighs 7000 metric
470 tons. The detector is 46 m long, 25 m high, 25 m wide as shown in Figure 6.1.
471 The detector can be divided into three subsystems: the Inner Detector (ID), the
472 Calorimeters, and the Muon Spectrometer (MS). Figure 6.2 shows an overview of
473 how different particles interact in the detector.

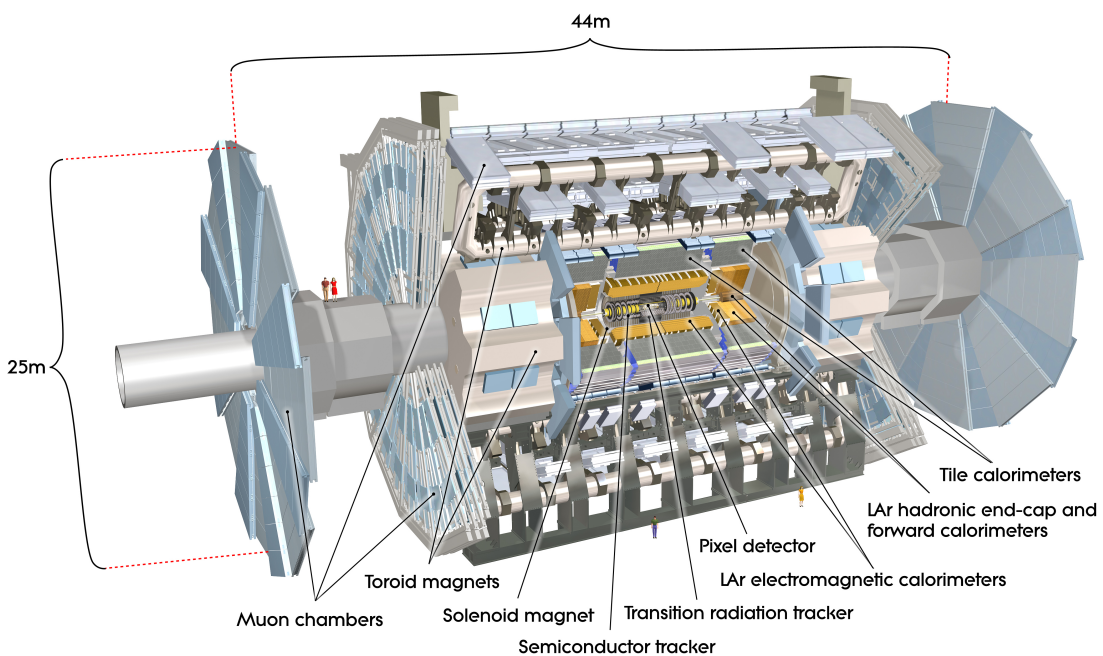


Figure 6.1: Overview schematic of the ATLAS detector.

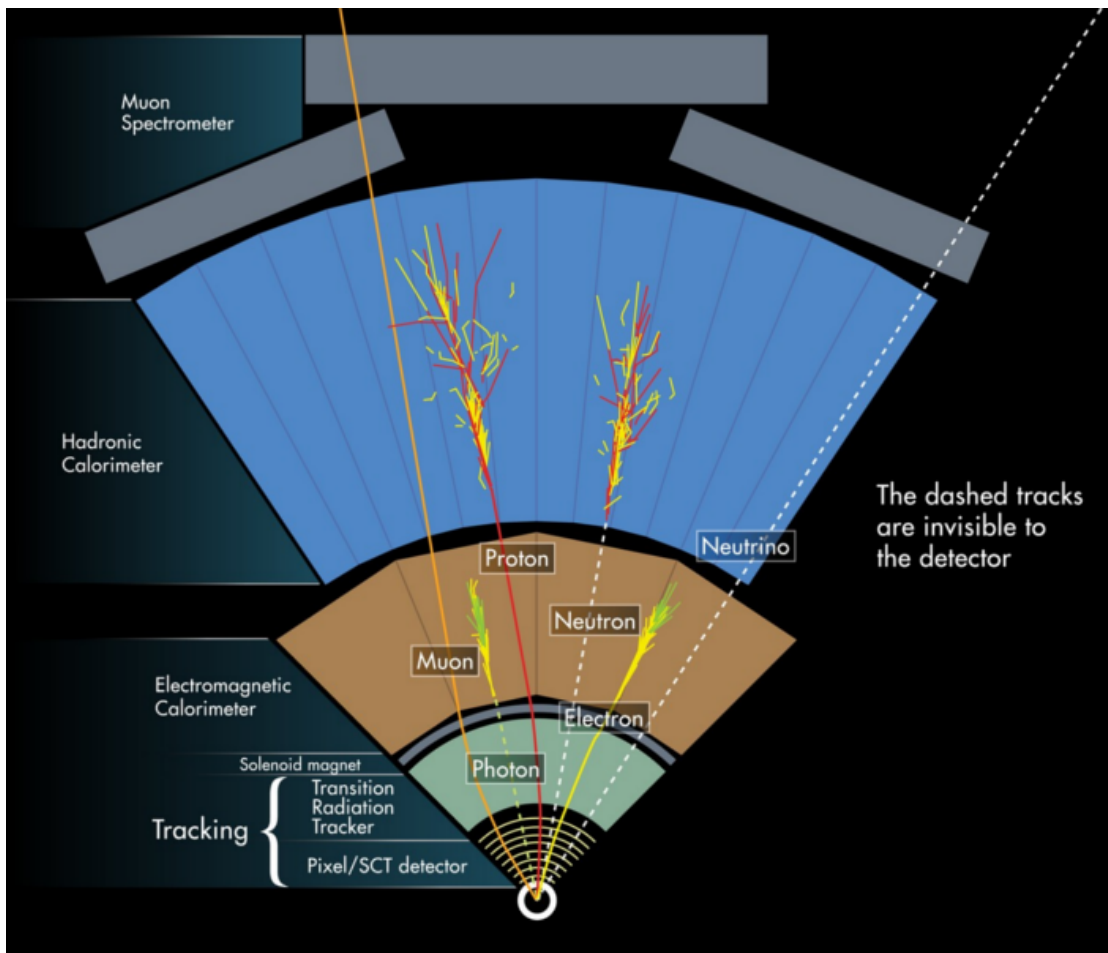


Figure 6.2: A simplified schematic of how different particles interact and are detected within ATLAS.

474 6.1 Coordinate System

475 The trajectory of particles within ATLAS is measured relative to the nominal
476 interaction point. The z -axis points along the beam line, such that when the
477 LHC is viewed from above, the counter-clockwise circulating beam points along
478 the positive- z direction. The $x - y$ plane is transverse to the beam line, with the
479 positive x -axis pointing towards the center of the LHC ring. The positive y -axis
480 points vertically upward. The azimuthal angle, ϕ , is the angular distance about
481 the z -axis, with $\phi = 0$ along the x -axis. The polar angle from the z -axis is denoted
482 as θ . However, this quantity is not Lorentz invariant, like rapidity, $y = \frac{1}{2} \ln \frac{E+p_z}{E-p_z}$,
483 where E is the energy of the particle considered, and p_z , is it's momentum along
484 the z -axis. Pseudorapidity is preferred as $\Delta\eta$ is invariant under boosts along z
485 and particle production is approximately invariant under η . For massless particles,
486 rapidity and a related quantity, pseudorapidity, are the identical. The pseudora-
487 pidity is defined as: $\eta = -\ln \tan(\frac{\theta}{2})$. This quantity is preferred as it is purely a
488 geometric quantity, independent of particle energy. Angular separation between
489 particles in ATLAS are given by $\Delta R = \sqrt{\Delta\eta^2 + \Delta\phi^2}$. The distance from the
490 beamline is given by $r = \sqrt{x^2 + y^2}$

491 6.2 Inner Detector

492 The Inner Detector (ID) was designed to identify and reconstruct vertices,
493 distinguish pions from electrons, and measure the momentum of charged particles.
494 The ID uses three different technologies for particle reconstruction: the Pixel
495 Detector, Semiconductor Tracker (SCT), and the Transition Radiation Tracker
496 (TRT), shown in Figure 6.3 and 6.4. The entire ID is immersed in a 2T solenoidal
497 magnetic field parallel to the $+z$ -axis, causing charged particles to bend in the

⁴⁹⁸ transverse-plane, allowing particle momentum measurements.

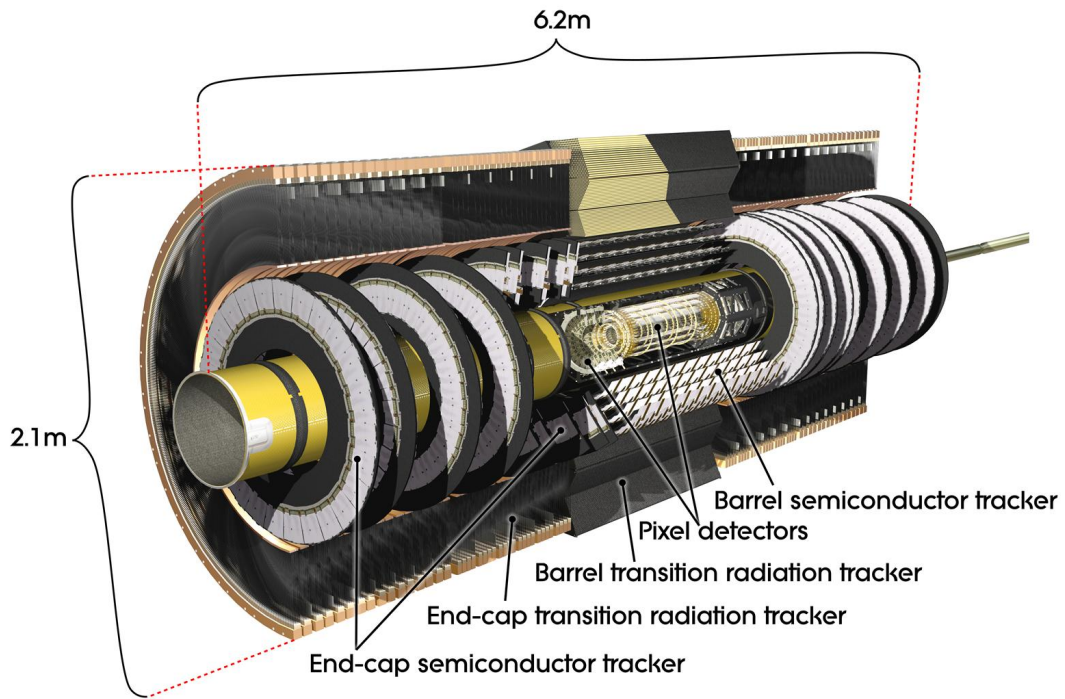


Figure 6.3: Layout of ATLAS Inner Detector

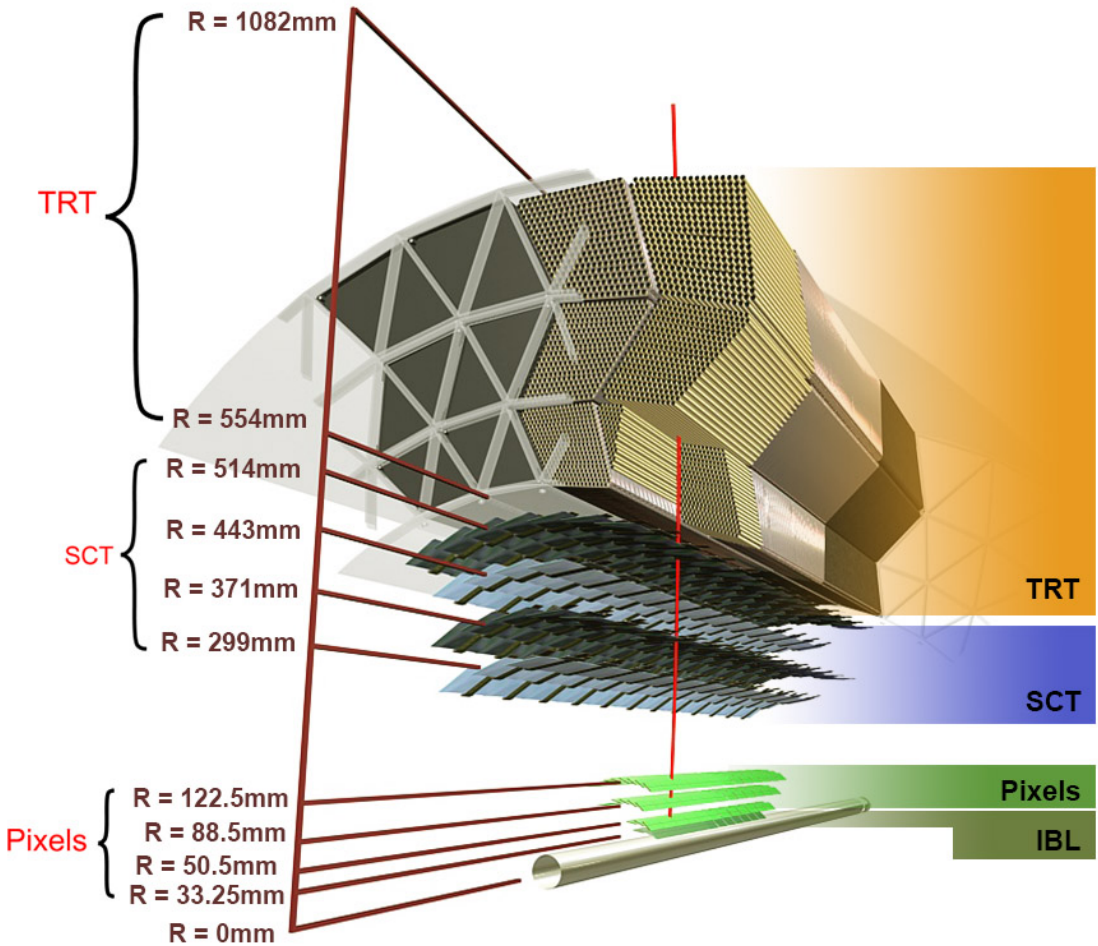


Figure 6.4: Layout of ATLAS ID Barrel System.

499 6.2.1 Pixel Detector

500 The pixel detector consists of four barrel layers between $r = 32.7$ and 122.5
 501 mm, extending to $|z| = 400.5$ mm. The remaining detectors are arranged in bar-
 502 rels and forward and backward rings. The innermost pixel barrel, the Insertable
 503 b-Layer (IBL), only extends to $|z| = 332$ mm. The pixel detectors closer to the
 504 beam line (larger η values) consists of six parallel cylindrical rings of pixel de-
 505 tectors transverse to the beam line. The entire pixel detector consists of 1744
 506 identical pixel sensors each with 46080 readout channels, totaling about 80 mil-
 507 lion individual pixels. Most of the pixel sensors are $50 \times 400 \mu\text{m}^2$. Each pixel has

508 a position resolution of $14\mu\text{m}$ in ϕ and $115\mu\text{m}$ in the z direction.

509 **6.2.2 Semiconductor Tracker**

510 The SCT is located outside the pixel detector and has the same barrel and
511 endcap geometry as the pixel detector. SCT sensors are $80\mu\text{m} \times 12\text{ cm}$ with
512 a $80\mu\text{m}$ strip pitch. In the barrel the strips are parallel to the z -axis and are
513 segmented in ϕ . In the endcaps, the strips extend radially. Sensors are grouped in
514 modules containing two layers of strips rotated 40 mrad with respect to each other.
515 This offset allows for the two-dimensional position of a track to be determined by
516 identifying the crossing point of the strips that registered a hit. SCT modules
517 measure tracks with an accuracy of $17\mu\text{m}$ in $r - \phi$ and $580\mu\text{m}$ in $z(r)$ in the
518 barrel (end-cap) region.

519 **6.2.3 Transition Radiation Tracker**

520 The transition radiation tracker (TRT), enveloping the SCT, is a gaseous
521 straw-tube tracker mainly used for electron/pion track separation. Each straw
522 is 4 mm in diameter and filled with a Xe- CO_2 - O_2 gas mixture. An anode wire at
523 the center of the straw is held at ground potential, while the walls of the straw
524 are kept at -1.4kV. When a charged particle passing through the TRT ionizes the
525 gaseous mixture, the resulting ions form an avalanche on the anode wire with a
526 gain of $\sim 10^4$. The signal from the anode wire is then digitized and discriminated.
527 Signals passing a low threshold cutoff are used to distinguish noise from tracks.
528 Signals passing a high threshold cutoff are sensitive to transition radiation (TR).
529 TR photons are emitted when charged particles pass between materials with dif-
530 ferent dielectric constants. The probability that a charged particle with energy E
531 and mass m passing between two materials emits a TR photon in the keV range

532 is proportional to $\gamma = E/m$. In the TRT straws these often then convert via the
533 photoelectric effect, causing a large avalanche triggering the high-threshold. Since
534 electrons have a smaller mass than pions, electron tracks are more likely to trig-
535 ger the high threshold. This then provides discrimination between electrons and
536 charged hadrons.

537 The barrel region of the TRT extends from $r = 563\text{-}1066$ mm and $|z| < 712$
538 mm. Barrel Straws are 144 cm long (divided $\sim \eta \approx 0$) and orientated parallel to
539 the beam direction. End-cap straws extend radially and are 37 cm long. There
540 are 53,544 straws in the barrel and 160,000 straws in the end-caps. Radiator mats
541 of polypropylene/polyethylene fibers in the barrel are aligned perpendicular to the
542 barrel straws (with holes for the straws to pass through). In the end-cap region,
543 radiator foils are layered between the radial TRT straws.

544 The arrival time of the signal pulse is sensitive to the distance between the
545 charged particle track and the anode wire and allows for a hit resolution of $130\mu\text{m}$.
546 The TRT extends to $|\eta| = 2.0$ and provides about 36 hits per track.

547 6.3 Calorimeters

548 The ATLAS electromagnetic and hadronic calorimeters (EMC and HCAL,
549 respectively) absorb and measure the energy of high energy hadrons, photons,
550 and electrons with $|\eta| < 4.9$. Both systems use sampling calorimeters which
551 consist of alternating layers of dense absorbing and active layers. In the absorbing
552 layer particles interact and lose energy, creating showers. These showers are then
553 detected and measured in the active layer. The amount of charge measured in the
554 active material scales with the energy of the incident particle, and thus provides a
555 measurement of the particle's energy. An overview of the layout of the calorimeter
556 system is shown in Figure 6.5.

557 The EMC measures and contains the energy of electromagnetically interacting
558 particles. It consists of layered accordion-shaped Lead absorber plates and elec-
559 trodes immersed in liquid Argon with 170k channels.. Using accordion-shaped
560 electrode and absorbers ensures ϕ symmetry and coverage. The EMC is com-
561 posed of a barrel part ($|\eta| < 1.475$), two end-caps ($1.375 < |\eta| < 3.2$), and a
562 presampler ($|\eta| < 1.8$). The presampler, containing only liquid Argon, corrects
563 for upstream energy losses of electrons and photons. The EMC barrel is segmented
564 into three layers. The first layer has finest segmentation with readout cells ex-
565 tending $\Delta\eta \times \Delta\phi = 0.025/8 \times 0.1$. This provides a precise shower measurements
566 used to separate prompt photons from $\pi^0 \rightarrow \gamma\gamma$ decays. The second layer has
567 coarser segmentation and is approximately 16 radiation lengths long. A radiation
568 length is the average distance an electron travels before losing all but $1/e$ of its
569 energy to bremsstrahlung. The last layer is the most coarse and measures the tail
570 of the electromagnetic shower. A schematic of the ECAL is shown in Figure 6.6.

571 The hadronic calorimeter located outside the EMC and is used to contain
572 and measure the energy of hadronically interacting particles. It consists of a tile
573 calorimeter (TileCal), hadronic end-cap calorimeter (HEC), and liquid Argon for-
574 ward calorimeter (FCAL). TileCal is located behind the LAr EMC and uses steel
575 absorbers and liquid Argon as the active material. TileCal consists of three barrel
576 layers in the central and forward regions, extending up to $|\eta| < 1.7$. Photons
577 generated from hadronic interactions are collected via wavelength-shifting fibers
578 connected to photomultiplier tubes, as shown in Figure 6.7. The HEC lies behind
579 the EMC endcap wheels. It uses copper absorbers and liquid Argon as the active
580 material and covers $1.5 < |\eta| < 3.2$. Finally, the FCAL covers $3.1 < |\eta| < 4.9$
581 and consists of three modules all using liquid Argon as the active material. The
582 first module uses copper absorber and was designed for electromagnetic measure-

583 ments. The second and third modules consist of tungsten absorber and are used
584 to measure the kinematics of hadronically interacting particles. A schematic of
585 the HCAL is shown in Figure 6.7.

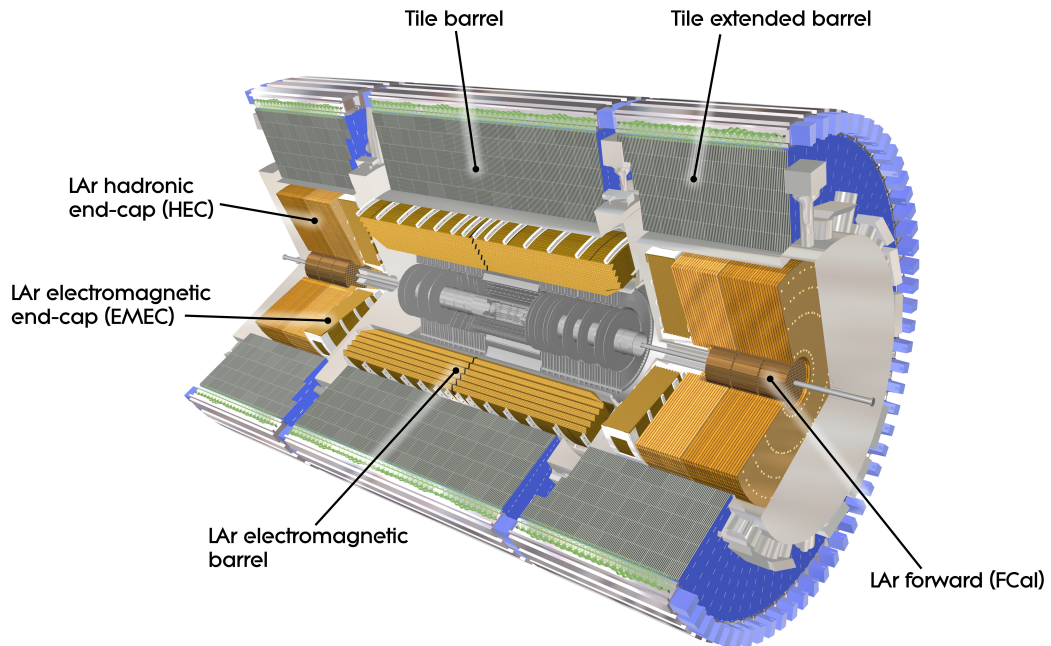


Figure 6.5: Overview of ATLAS electromagnetic and hadronic calorimeters.

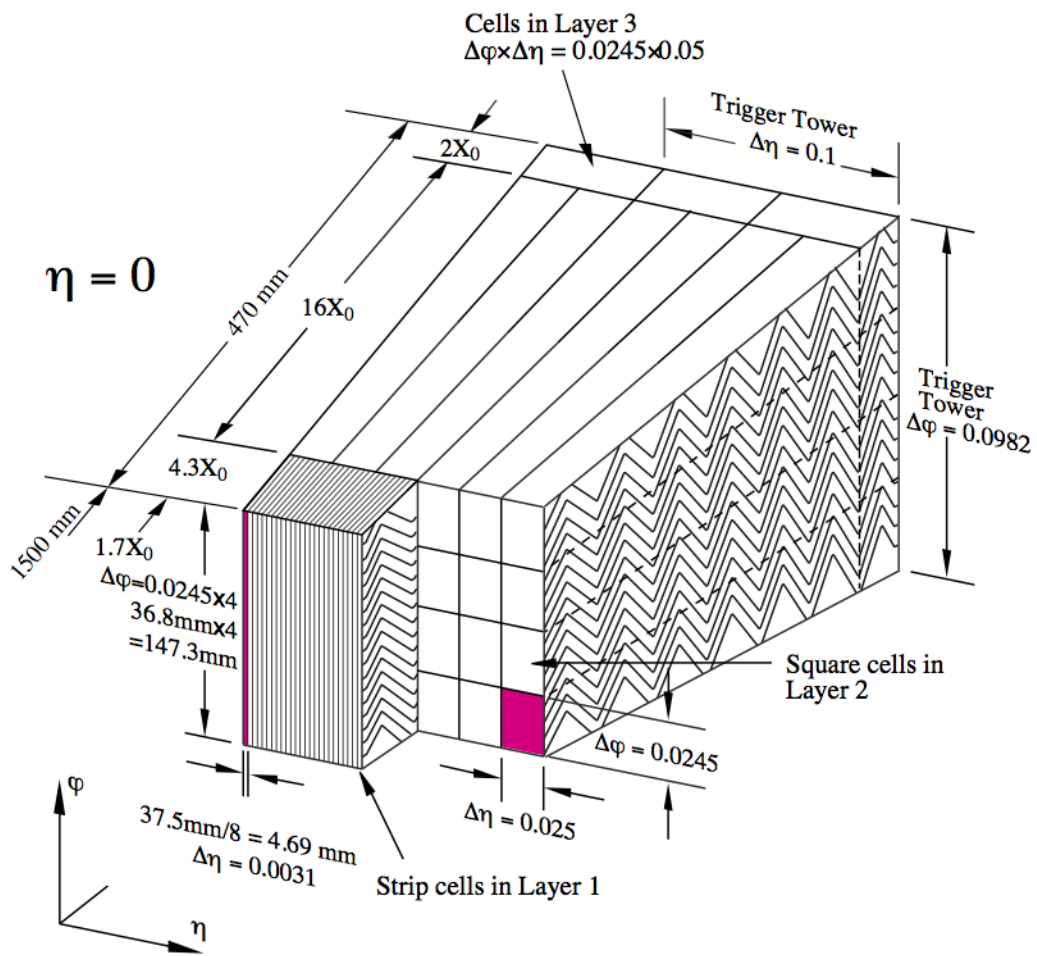


Figure 6.6: Schematic of ECAL.



Figure 6.7: Schematic of HCAL.

586 The energy resolution of the calorimeter subsystems are:

$$587 \quad \frac{\sigma_E}{E} = \frac{10\%}{\sqrt{E}} \oplus \frac{0.3\%}{E} \oplus 0.4\% \text{ Electromagnetic Calorimeter}$$

$$588 \quad \frac{\sigma_E}{E} = \frac{50\%}{\sqrt{E}} \oplus \frac{1.8\%}{E} \oplus 3\% \text{ Hadronic Calorimeter}$$

589 **6.4 Muon Spectrometer**

590 The muon spectrometer (MS) is the outermost detector system in ATLAS.

591 Muons with a $p_T > 4$ GeV are energetic enough to reach the MS. To measure the
592 momentum of these muons barrel and end-cap toroid magnets are used covering
593 $|\eta| < 1.4$ and $1.6 < |\eta| < 2.7$. For $1.4 < |\eta| < 1.6$, a combination of the barrel
594 and end-cap toroidal magnetic fields bend muon trajectories. The detector in the
595 barrel region form three concentric rings at $R = 5, 7.5, 10$ m and are segmented
596 in ϕ to accommodate the magnets. The end-cap region consists of three circular
597 planes perpendicular to z and located at $|z| = 7.4, 14, 21.5$ m from the interaction
598 region. An additional detector at $|z| = 10.8$ m covers the transition region between
599 the barrel and end-cap.

600 The MS readout consists of four subsystems: Monitored Drift Tubes (MDT),
601 Cathode Strip Chambers (CSC), Resistive Plate Chambers (RPC), and Thin Gap
602 Chambers (TGC). The first two subsystems are used primarily for measuring
603 muon track parameters, while the RPC and TGC subsystems are used for muon
604 triggering. A schematic of this system is shown in Figure 6.8.

605 The MDT subsystem consists of precision tracking chambers for $|\eta| < 2.7$,
606 except for the inner most end-cap layer ($2.0 < |\eta| < 2.7$), where CSCs are used.
607 The basic unit of MDT chambers are thin walled Aluminum tubes with a diameter
608 of 3 cm and length of 0.9-6.2 m. These tubes are filled with a mixture of Ar-CO₂
609 gas with a 50μm W-Rn wire running down the center of the tube, which is kept at
610 3080 V. Since the maximum drift time of these chambers is ∼ 700 ns, they are not

611 used for triggering. MDT chambers consist of 3-4 layers of tubes mounted on a
612 rectangular support system, as seen in Figure 6.9, orientated along ϕ to measure
613 the coordinate in the bending plane of the magnetic field with a resolution of 35
614 μm .

615 The MDT subsystem can only handle hit rates below 150 Hz/cm². For this
616 reason, CSCs are used in the innermost end-cap layer where hit rates are larger.
617 CSCs can handle hit rates up to 1000Hz/cm². CSC are multiwire proportional
618 chambers. These chambers are filled with a Ar-CO₂ gas mixture and evenly spaced
619 wires kept at 1900 V. These wires are orientated in the radial direction but not
620 read out. Instead on one side of the cathode are copper strips parallel to the wires,
621 measuring η , while on the other side of the cathode are strips parallel to the wires
622 measuring ϕ . The width between strips is approximately 1.5 mm providing a
623 resolution of 60 μm in the bending-plane and 5 mm in the non-bending plane.

624 Since the CSC and MDT systems do not have prompt timing signals, the RPC
625 and TGC systems are used for triggering. The RPC system is used in the barrel
626 region ($|\eta| < 1.05$). RPC consist of two parallel resistive plates separated by a
627 2 mm insulated spacer with 100 mm spacing kept at 9.8 kV, as shown in Figure
628 6.10. A gaseous mixture of C₂H₂F₄, C₄H₁₀, and SF₆ fills the space between the
629 two plates. Metallic strips on the outer faces of the plates are used to read out
630 signals produced by the gas ionizing. The middle barrel layer consists of two layers
631 of RPCs on either side of the MDT layer and one layer on the outermost MDT
632 layer. Each layer contains two orthogonal sets of metallic strips providing η and
633 ϕ measurements. The timing resolution of RPCs is 1.5 ns, and therefore may be
634 used to identify bunch crossings.

635 Finally, the TGCs are used in the end-cap regions and are primarily used to
636 provide L1 trigger decisions and ϕ measurements. TGCs are multi-wire propor-

637 tional chambers consisting of arrays of gold-coated tungsten wires placed between
 638 two cathode planes. These wires are separated by 1.8 mm and cathodes are 1.4 mm
 639 from the wires. Orthogonal to the wires, on the opposite side of the cathode plane
 640 are copper strips held at 2900 V. The chambers are filled with a mixture of CO₂
 641 and n-pentane gas, the latter acts as a quenching gas to prevent avalanches initi-
 642 ated by secondary γ -rays from the primary avalanche. Figure 6.11 is a schematic
 643 of a TGC. The timing resolution of TGCs is less than 25 ns and therefore they
 644 are used for bunch crossing measurements.

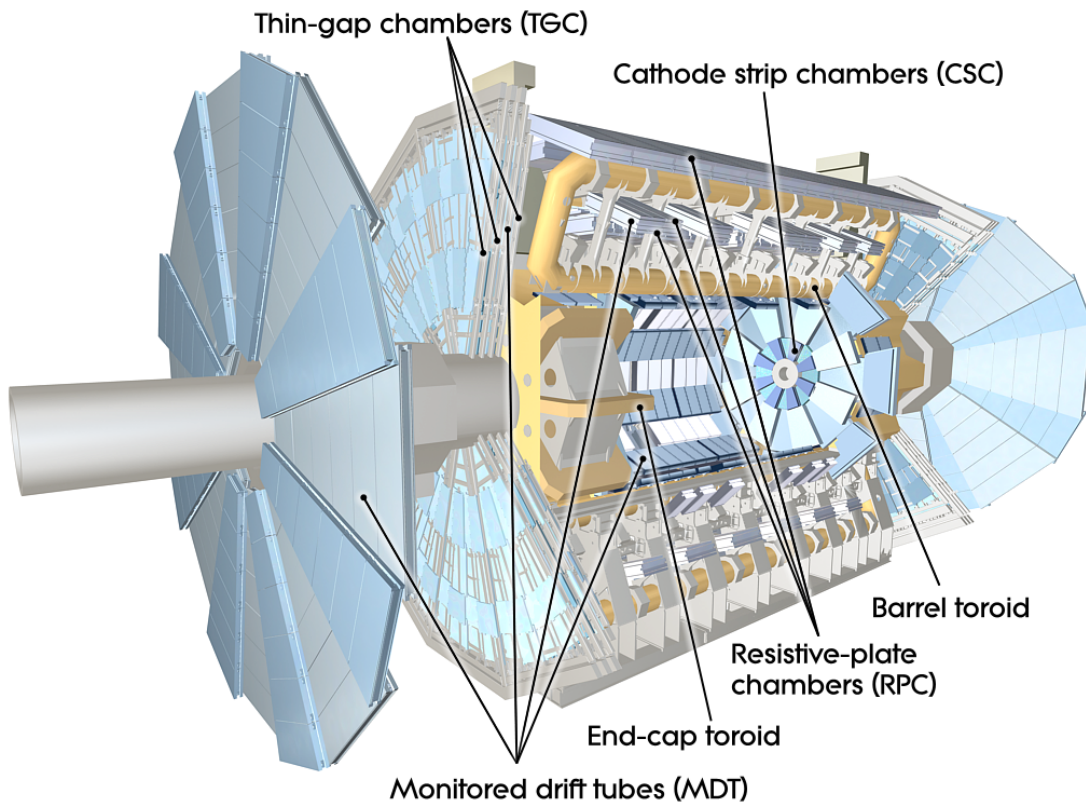


Figure 6.8: Schematic of Muon Spectrometer [cite G35]

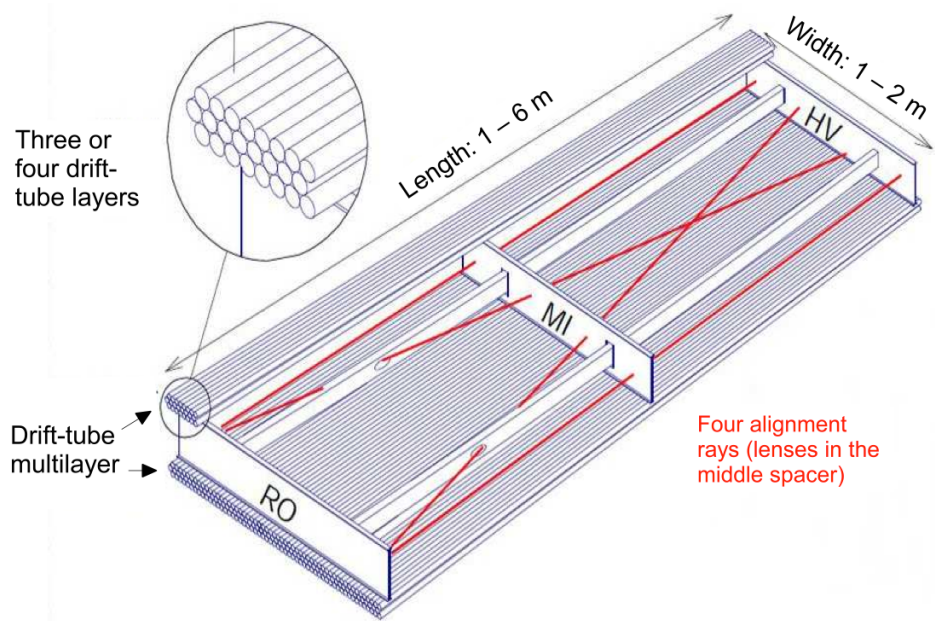


Figure 6.9: Schematic of MDT chamber. [cite G35]

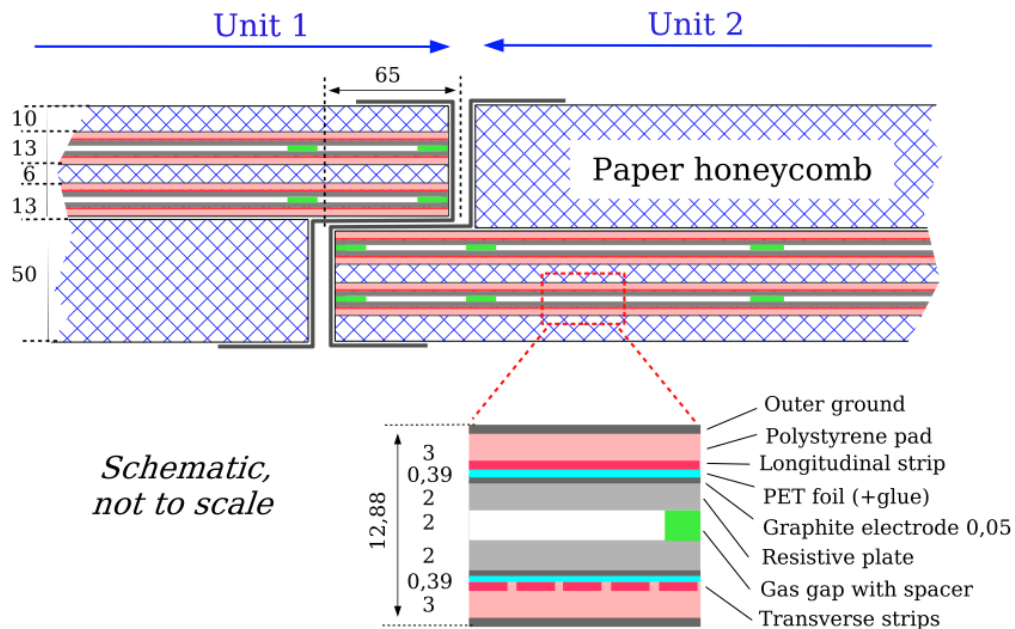


Figure 6.10: Schematic of RPC chamber, which is used for triggering in the central region of the detector [cite G35].

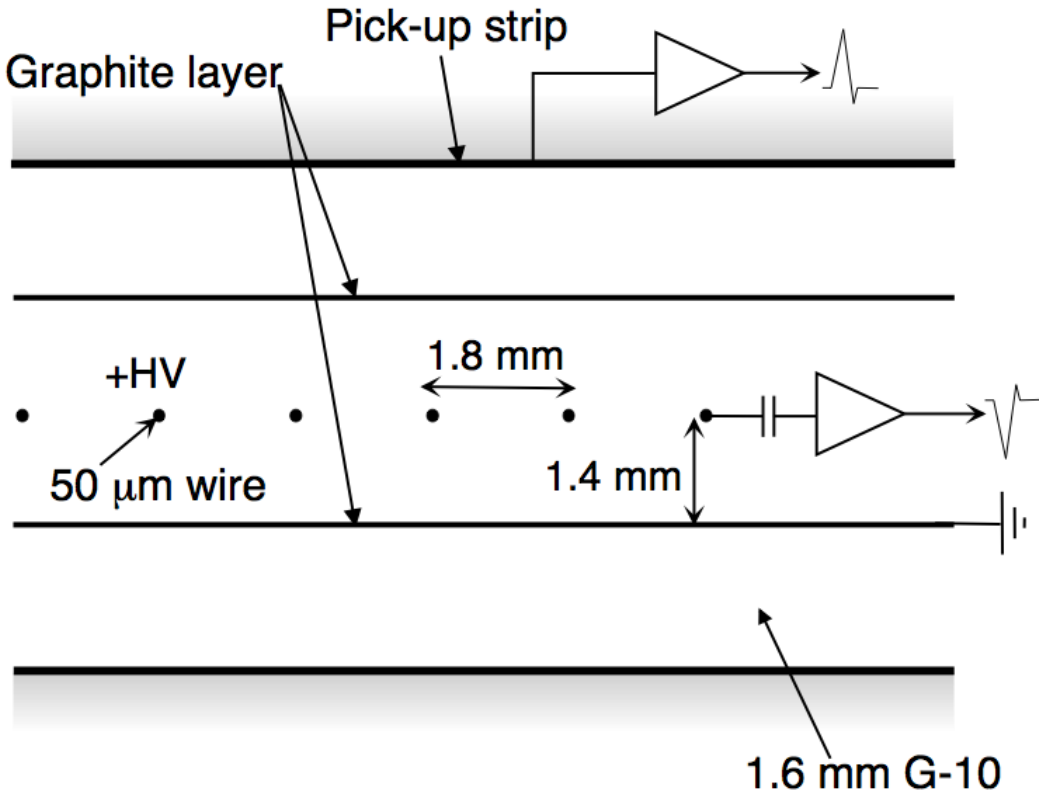


Figure 6.11: Schematic of TGC chamber, which is used for triggering in the muon end-cap region. [cite G35]

645 6.5 Magnet System

646 A particles with charge, q , and velocity v , moving in magnetic field, B , ex-
 647 periences a force, $F = qv \times B$. This force can cause charged particles to have a
 648 curved trajectory in magnetic fields, which the ID and MS use to determine the
 649 particles p_T . The central solenoid provides the magnetic field for the ID and the
 650 toroidal magnets provide the magnetic field for the MS.

651 The layout of the magnet system is shown in Figure 6.12. The central solenoid
 652 consists of a single-layer Al-stabilized NbTi conductor coil wound inside an Al

653 support cylinder. The solenoid is 5.8 m long, 50 cm thick and has an inner radius
654 of 1.23 m. It is cooled to 4.5 K to reach superconducting temperatures and shares
655 the liquid argon calorimeter vacuum vessel to minimize material in the detector.
656 A current of 7.730 kA produces a 1.998 T solenoidal magnetic field, pointing in
657 the $+z$ direction.

658 The toroidal magnet system consists of a barrel and two end-cap toroidal
659 magnets used to create a magnetic field outside the calorimeters that is orientated
660 along ϕ . Each barrel toroid is 25.3 m long with an inner and outer diameter of 9.4
661 and 20.1 m and weighs 830 tonnes. Endcap toroids are 5 m long with an inner and
662 outer radius of 1.65 and 10.7 m. Both toroid systems use Al-stabilized Nb/Ti/Cu
663 conductors. The magnetic field strength in the barrel and endcap regions are 0.5
664 and 1 T, respectively.

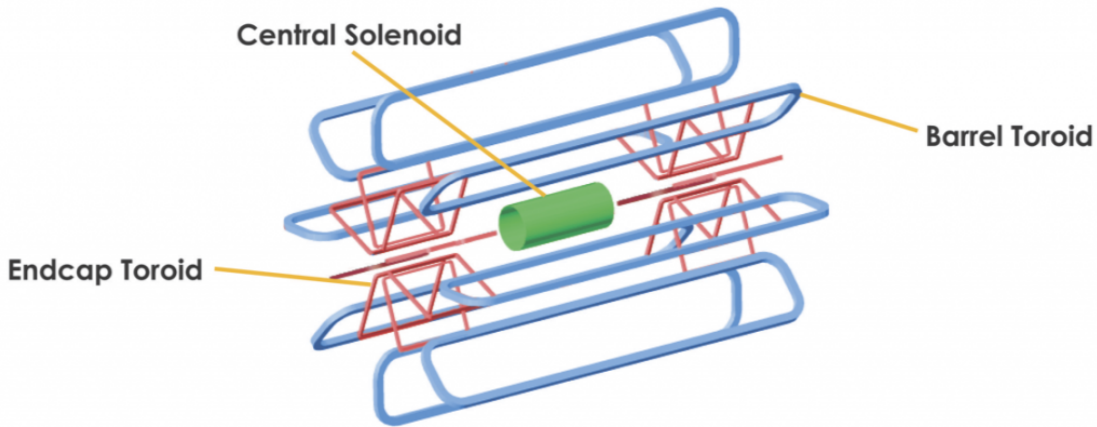


Figure 6.12: Layout of ATLAS magnet systems.

665 **6.6 Trigger System**

666 Since collisions occur every 25 ns and reading out all detector channels and
667 storing that information is not currently feasible (would require saving 60 million
668 megabytes per second), the majority of events are not kept for analysis. ATLAS

669 uses a multi-stage trigger system to select approximately 1,000 of the 1.7 billion
670 collisions that occur each second (corresponding to a rate of 1 kHz from the 40
671 MHz proton collision rate). The first stage of the trigger system is the hardware
672 level (L1) trigger. This trigger reduces the event rate to \sim 100 kHz by identifying
673 Regions-of-Interest (ROIs) containing high p_T leptons, photons, jets, or E_T^{miss} by
674 using information from RPCs, TGCs, and calorimeters to make a $2.5 \mu\text{s}$ decision.
675 This information is then passed to a high-level trigger (HLT) which further de-
676 creases event rates to \sim 1 kHz. The HLT uses finer granularity measurements
677 from the MS and ID to perform simplified offline reconstruction to decide which
678 events to keep.

679

Part IV

680

The Search for WW and WZ

681

Resonances in $\ell\nu qq$ final states

682 **Chapter 7**

683 **Dataset and Simulated Samples**

684 **7.1 Dataset**

685 This analysis uses pp collision data collected from 2015 to 2018 at $\sqrt{s} = 13$
686 TeV, corresponding to 139/fb of data as shown in Figure 7.1 and 7.2. From this
687 dataset, only those events in which the tracker, calorimeters, and muon spectrom-
688 eter have good data quality are used. For a given event, the solenoid and toroidal
689 magnets must also be operating at their nominal field strengths. In addition to
690 this, events must pass further quality checks to reject events where detector sub-
691 systems may have failed. These selections reject events that containing LAr noise
692 bursts, saturation in the electromagnetic calorimeter, TileCal errors, and failures
693 in event recovery due to tracker failures. Events with information missing from
694 subsystems (usually due to busy detector conditions) are rejected. Events must
695 also contain a primary vertex with at least two associated tracks, where the pri-
696 mary vertex is selected as the vertex with the largest $\sum p_T^2$ over tracks associated
697 with the vertex and $p_T > 0.5$ GeV.

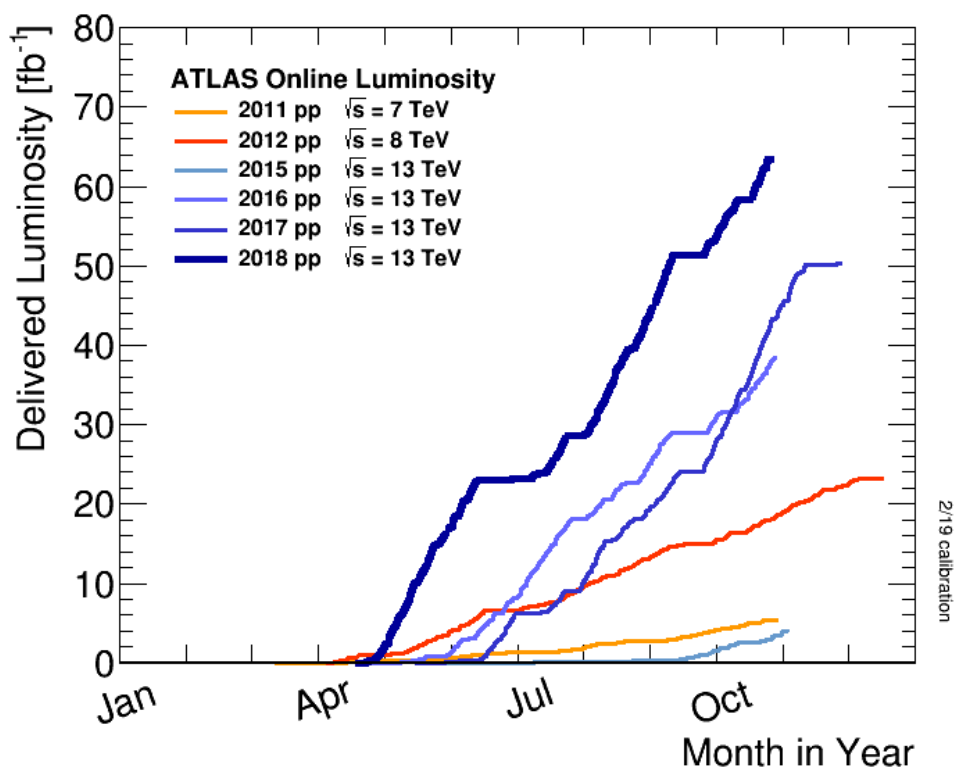


Figure 7.1: Integrated luminosity for data collected from ATLAS from 2011 - 2018



Figure 7.2: Mean number of interactions per crossing for data collected from ATLAS from 2011 - 2018

698 **7.2 Simulated Samples**

699 Samples are simulated in order to model backgrounds, evaluate signal ac-
700 ceptance, optimize event selection and estimate systematic and statistical uncer-
701 tainties. The dominant backgrounds for this analysis are $W/Z + \text{jets}$, diboson
702 (WZ/WW), $t\bar{t}$, single top and multijet production.

703 $W/Z+\text{jet}$ events are simulated using Sherpa 2.2.1 at NLO [cite [29]] and merged
704 with the Sherpa parton shower using the ME+PS@NLO prescription [15]. These
705 events are then normalized to NNLO cross sections. The $t\bar{t}$ and single-top back-
706 grounds are generated with Powheg-Box with NNPDF3.0NLO PDF sets in the
707 matrix element calculation [cite[35]]. For all processes, the parton shower, frag-
708 mentation, and underlying event are simulated using Pythia 8.320 with the A14
709 tune set[cite[ATL-PHYS-PUB-2014-02]]. Diboson processes are generated using
710 Sherpa 2.2.1.

711 Signal samples are simulated using MadGraph 5-2.2.2 [cite 42] and Pythia
712 8.186 with NNPDF230LO. RS Graviton samples are generated with $k/M_{PL}=1$.
713 HVT Model A (B) samples are simulated with $g_V = 1(3)$, as the difference in
714 the width of the samples is smaller than detector resolution. To model VBF
715 production of HVT signals, $g_H = 1$ and $g_f = 0$. Signals are generated for masses
716 between 300 GeV and 5 TeV.

717 **Chapter 8**

718 **Objects**

719 **8.1 Electrons**

720 Electrons are reconstructed from electromagnetic showers in the LAr EM
721 calorimeter. During reconstruction cells of $\Delta\eta \times \Delta\phi = 0.025 \times 0.025$ are grouped
722 into 3×5 clusters. These clusters are then scanned for local maxima that seed
723 electron clusters. These clusters must then be matched to ID track from the PV.
724 This requirement minimizes non-prompt electron and fake electron backgrounds.
725 Electrons must pass identification and isolation requirements. Electron identifica-
726 tion (loose, medium, tight) classification is based on a multivariate discriminant
727 that identifies electrons using a likelihood based method. For this analysis, events
728 are required to have one tight electron and no additional loose electrons. Elec-
729 trons are also required to be isolated. The electrons are considered isolated if the
730 quotient of the sum of the transverse momentum (of calorimeter energy deposits)
731 in a cone around the electron of size $\Delta R = 0.2$ and the transverse momentum
732 of the electron to be less than $0.015 * p_T$ or 3.5 GeV, whichever is smaller. This
733 requirement rejects non-prompt photons and other fake leptons. Electrons in this
734 analysis are also required to have $p_T > 30$ GeV and $|\eta| < 2.47$. Electrons are also

735 required to have $p_T > 30$ GeV.

736 Electrons are calibrated to determine data-driven scale factors using $J/\Psi \rightarrow$
737 ee , $Z \rightarrow ee$, $Z \rightarrow \ell\ell\gamma$ processes. These corrections account for the non-uniform
738 response of the detector which introduces modeling and reconstruction uncertain-
739 ties.

740 8.2 Muons

741 As muons traverse the entire detector, they are reconstructed from ID and
742 MS tracks. For this analysis the muon identification and isolation working points
743 are chosen to minimize the contributions from non-prompt muons. Towards this
744 end, each selected event must contain exactly one muon that passes the medium
745 identification working point, and no additional muons (that pass the loose working
746 point). For the medium working point, two types of reconstructed muons are
747 used: combined and extrapolated muons (CB and ME, respectively). For CB
748 muons, ID and MS tracks are reconstructed independently and a combined track
749 fit is performed by adding or removing MS tracks to improve the fit quality.
750 ME muons are reconstructed from only MS tracks with hits in at least two layers,
751 which ensures the track originates from the PV. ME muons extend the acceptance
752 for muon reconstruction outside the ID from $2.5 < |\eta| < 2.7$. The medium
753 identification working point uses CB and ME tracks. CB tracks must have at
754 least 3 hits in two MDT layers. ME tracks are required to have at least three
755 MDT/CSC hits. To further minimize contributions from fake muons, the selected
756 muons are required to be isolated from other tracks, as muons from W, Z decays are
757 often isolated from other particles. To insure the selected muons are isolated, the
758 scalar sum of the transverse momentum of tracks in a cone of $\Delta R = 0.3$ compared
759 to the transverse momentum of the muon must be less than 0.06. Muons are also

760 required to have $p_T > 30$ GeV.

761 Muons are calibrated using well-studied resonances $J/\Psi \rightarrow \mu\mu$ (for $p_T^\mu < 10$
762 GeV), $Z \rightarrow \mu\mu$ (for $p_T^\mu > 10$ GeV). Figure 8.1 shows the combined muon p_T
763 uncertainty from this calibration. The total systematic uncertainty is less than
764 1% for all p_T ranges considered in this analysis.

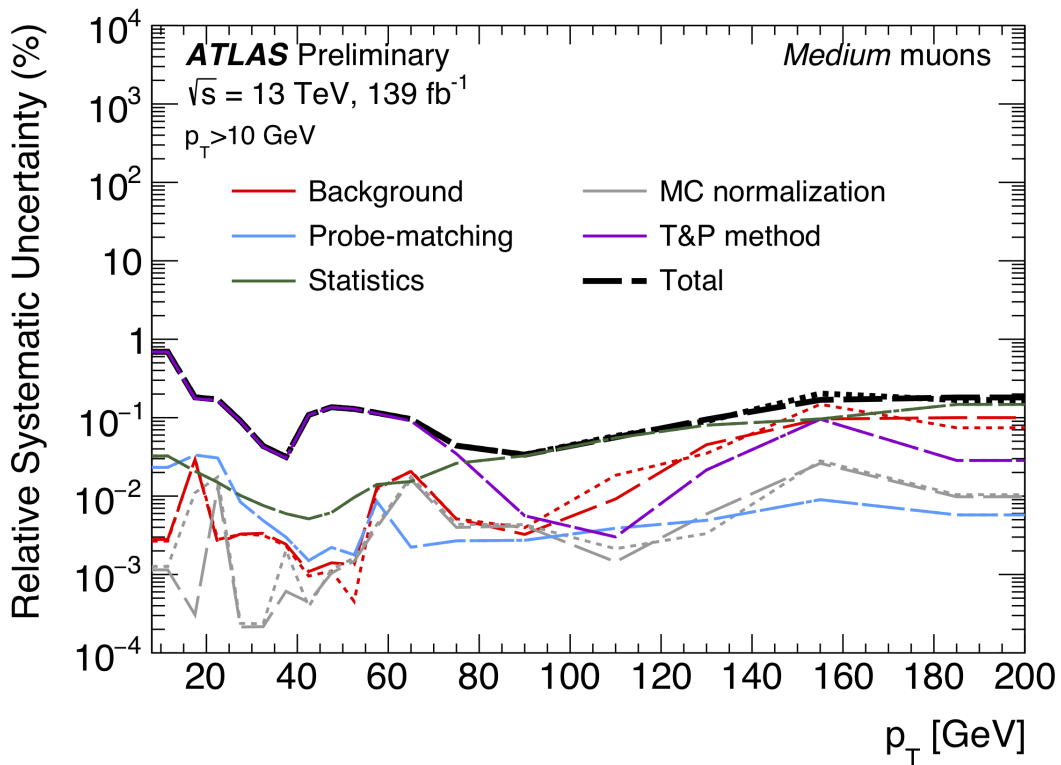


Figure 8.1: This figure shows the breakdown of the muon reconstruction efficiency scale factor measured in $Z \rightarrow \mu\mu$ as a function of p_T [6].

765 8.3 Jets

766 Three types of jets are used in this analysis: variable radius, small-R and
767 large-R jets. Variable radius jets are used to reconstruct Z bosons decaying to
768 two b -jets in the jet catchment area of large-R jet in the Merged regime. Small-R

769 jets are used to reconstruct the hadronically decaying W/Z candidates in the
770 resolved analysis and the forward jets from resonances produced through vector
771 boson fusion. Large-R jets are used to reconstruct the hadronically decaying boson
772 in the merged regime.

773 For these jet collections, the jet energy is calibrated sequentially as shown in
774 Figure 8.2. After the jet direction is corrected to point to the PV, the energy
775 of the jet is corrected. First, the jet energy is corrected to account for pileup
776 contributions based on the p_T and area of the jet (these corrections are extracted
777 from a $pp \rightarrow jj$ sample). Following this, another pileup correction is applied that
778 scales with μ and N_{PV} .

779 MC-based corrections are then applied that are meant to transform the jet
780 energy and η back to truth level as detailed in [9]. Therefore, these corrections
781 account for the non-compensating nature of the ATLAS calorimeters and inho-
782 mogeneity of the detector. Following this, the Global Sequential Calibration is
783 applied that reduces flavor dependence of jet calibrations and accounts for energy
784 leakage of jets outside the calorimeters. Finally, in-situ corrections are applied that
785 account for differences in jet responses between data and simulation ($\gamma/Z+jet$ and
786 fake lepton samples are used). These differences can be due to mismodelling of
787 the hard scatter event, pile-up, jet formation, etc.

788 To further reject fake jets, jets must pass quality requirements based on the
789 following variables ([cite P42]):

- 790 - f_Q^{LAr} : fraction of energy of jet's LAr cells with poor signal shape
- 791 - f_Q^{HEC} : fraction of energy of jet's HEC cells with poor signal shape
- 792 - E_{neg} : sum of cells with negative energy
- 793 - f_{EM} : fraction of jet's energy deposited in EM calorimeter

- 794 - f_{HEC} : fraction of jet's energy deposited in HEC calorimeter
- 795 - f_{max} : maximum energy fraction in any single calorimeter layer
- 796 - f_{ch} : ratio of the scalar sum of the p_T of a jet's charged tracks to the jet's p_T
- 797 Jets selected for the resolved analysis must pass one of the following criteria:
- 798 - $f_{HEC} > 0.5$ and $|f_Q^{HEC}| > 0.5$ and $\langle Q \rangle > 0.8$
- 799 - $|E_{neg}| > 60$ GeV
- 800 - $f_{EM} > 0.95$ and $f_Q^{LAr} > 0.8$ and $\langle Q \rangle > 0.8$ and $|\eta| < 2.8$
- 801 - $f_{max} > 0.99$ and $|\eta| < 2$
- 802 - $f_{EM} < 0.05$ and $f_{ch} < 0.05$ and $|\eta| < 2$
- 803 - $f_{EM} < 0.05$ and $|\eta| > 2$

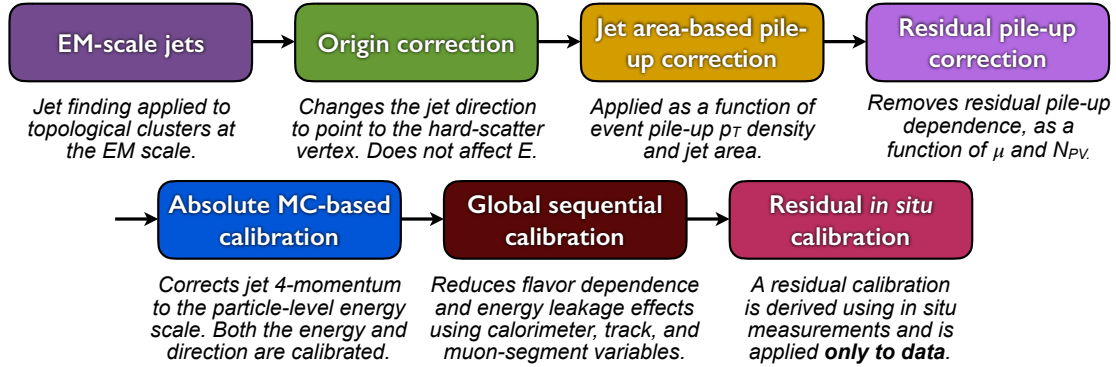


Figure 8.2: [10] This diagram shows the calibration stages for EM jets.

804 **8.3.1 Small-R jets**

805 Small-R jets are used to reconstruct the hadronically decaying W/Z candi-
806 date when the two resulting jets are well-separated in $\eta\text{-}\phi$ space. Small-R jets
807 are also used to identify forward jets from resonances produced through vector
808 boson fusion. Small-R jets are constructed from topologically connected clusters
809 of calorimeter cells (topoclusters), seeded from calorimeter cells with energy de-
810 posits significantly above the noise threshold. These cells are then used as inputs
811 to the $anti-k_t$ algorithm [18] with a radius parameter, $R = 0.4$, implemented in
812 the FastJet package [4].

813 Jets used in this analysis must have $p_T > 30$ GeV and $|\eta| < 2.5$. To further
814 reduce fake jets the jet-vertex-tagger (JVT) is used to reject pile-up jets [8]. The
815 JVT uses two track-based variables, corrJVF and R_{p_T} to calculate the likelihood
816 that the jet originated from the PV. The corrJVF compares the scalar sum of the
817 p_T of tracks associated with the jet and PV to the scalar sum of the p_T of tracks
818 associated with the jet. This variable also includes a correction that reduces the
819 dependency of corrJVF with the number of reconstructed vertices in the event.
820 The other discriminant, R_{p_T} , is given by the ratio of the scalar sum of the p_T of
821 tracks associated with the jet and PV to the p_T of the jet. Both of these variables
822 peak around zero for pileup jets, as these jets are unlikely to have tracks associated
823 with the PV. JVT cuts are applied to all jets with $p_T > 120$ GeV. Central jets
824 ($|\eta| < 2.4$) are required to have a $JVT > 0.59$ and forward jets ($2.4 < |\eta| < 2.5$)
825 are required to have $JVT > 0.11$.

826 **8.3.2 Large-R jets**

827 Large-R ($R = 1.0$) jets are used to reconstruct the hadronically decaying W/Z
828 candidate when the resulting jets are not well-separated in $\eta\text{-}\phi$ space, and overlap

forming one large-R jet. Track-Calorimeter Clusters (TCCs) are used to reconstruct these jets [cite ANA 50]. These jets are constructed using a pseudo particle flow method using ID tracks matched to calorimeter clusters. To remove contamination in the jet from pileup and the underlying event, jets are trimmed using a re-clustering algorithm. This algorithm removes subjets with $p_T^{subjet} < 0.1 p_T^{jet}$.

The angular resolution of the calorimeter degrades sharply with jet p_T , but the jet energy resolution improves. The tracker has excellent angular resolution which improves with p_T . Therefore, by matching tracks to jets, TCCs have more precise energy and angular resolution than jets constructed from calorimeter information only. These jets are required to have $p_T > 200$ GeV, $|\eta| < 2.0$ and $m_J > 50$ GeV.

TCC jets are trimmed as detailed in [cite ANA 45], which suppresses pileup and soft radiation in the jet, the jet mass is calculated as the four-vector sum of the jet's constituents (assuming massless constituents). The jet mass peaks around the W/Z boson mass for $W/Z \rightarrow qq$ jets, and more broadly for quark and gluon induced jets.

These jets are then tagged as W jet if it passes optimized jet mass and substructure (D_2) cuts for W bosons, and a Z jet if it passes the cuts for the Z boson. The jet substructure variable D_2 is given by the ratio of energy correlation functions. These functions are derived from the energies and pair-wise angles of a jet's constituents [cite ANA 46, 47]:

$$D_2^{\beta=1} = E_{CF3} \left(\frac{E_{CF1}}{E_{CF2}} \right)^3 \quad (8.1)$$

where the energy correlation functions are defined as:

$$E_{CF1} = \sum_i p_{T,i} \quad (8.2)$$

850

$$E_{CF2} = \sum_{ij} p_{T,i} p_{T,j} \Delta R_{ij} \quad (8.3)$$

851

$$E_{CF3} = \sum_{ijk} p_{T,i} p_{T,j} p_{T,k} \Delta R_{ij} \Delta R_{jk} \Delta R_{ki} \quad (8.4)$$

852 A two-dimensional optimization of the jet mass and D_2 thresholds was per-
 853 formed to provide maximum sensitivity for this analysis. This optimization was
 854 done by maximizing the signal sensitivity (using HVT W' and G_{KK} samples)
 855 against the single quark and gluon jet backgrounds in jet p_T bins. Figure 8.3
 856 shows the optimized thresholds on D_2 and jet mass as a function of p_T . Figure
 857 8.4 shows the efficiency of the optimized W/Z taggers as a function of jet p_T .

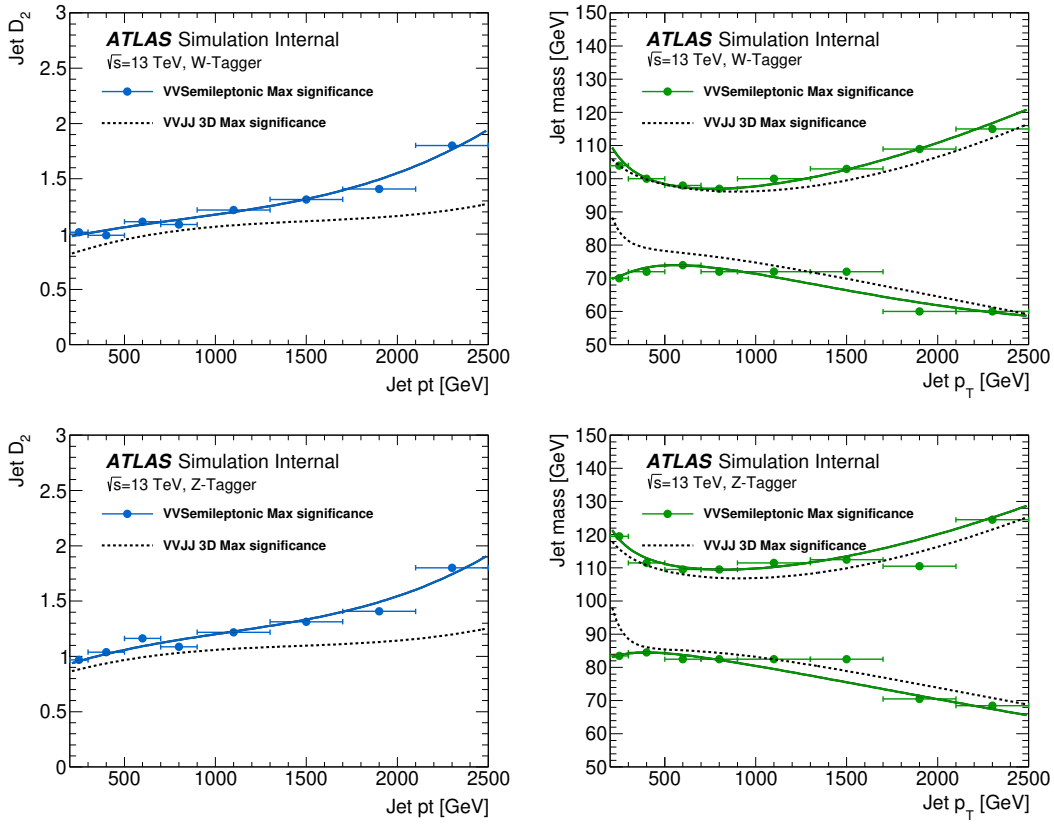


Figure 8.3: The upper cut on D_2 (a) and jet mass window cut i.e. the upper and lower boundary of the mass (b) of the W -tagger as a function of jet p_T . Corresponding values for Z -tagger are shown in (c) and (d). The optimal cut values for maximum significance are shown as solid markers and the fitted function as solid lines. Working points from $VV \rightarrow JJ$ [ATLAS-HDBS-2018-31-002] is also shown as dashed lines as a reference. Natasha reword?

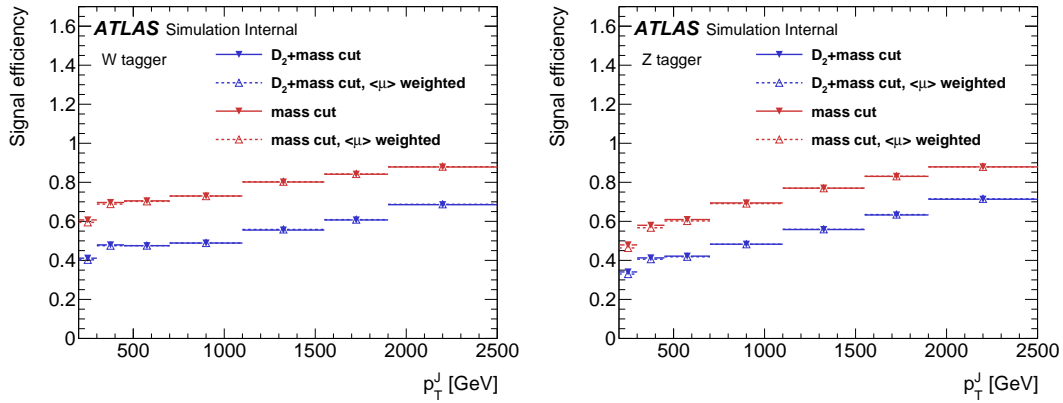


Figure 8.4: Natasha write caption

858 **8.3.3 Variable Radius jets**

859 To more accept more boosted Z bosons decaying to $b\bar{b}$ that would normally be
860 rejected due to topological cuts discussed 9.4 variable radius (VR) track jets are
861 used to identify b -jets (discussed in 8.3.4) within the catchment area of large-R
862 jets [17]. VR jets are constructed from ID tracks using the anti- k_t algorithm with
863 a radius parameter that depends on the p_T of the track, shown in Equation 8.5.

$$R_{eff}(p_{T,i}) = \frac{\rho}{p_{T,i}} \quad (8.5)$$

864 For this search $\rho = 30$ GeV and an lower and upper limit on cone size are set
865 to 0.02 and 0.4, respectively, to prevent unphysical asymptotic behavior of ρ .
866 Collinear VR jets are possible, so track jets that are not separated by the the
867 smaller jet's cone size are not used. Additionally, VR jets are required to have
868 $p_T > 10$ GeV and $|\eta| < 2.5$.

869 **8.3.4 Jet Flavor Tagging**

870 To further classify events, the small-R and VR jets originating from a b-quark
871 are classified using a multivariate b -tagging algorithm (BDT), MV2c10 [cite G 210
872 199]. This algorithm uses the impact parameters of the jet's ID tracks, secondary
873 vertices (if they exist), and reconstructed flight paths of b and c hadrons in the
874 jet to determine if the jet was induced by a b -quark. For this analysis the 85%
875 efficient working point of this algorithm is used giving c , τ , and light-flavor jet
876 rejection of 3, 8, and 34 respectively in simulated $t\bar{t}$ samples.

877 **8.4 MET/Neutrinos**

878 As neutrinos are uncharged and colorless they do not leave tracks or jets in
879 the detector. For this reason, neutrinos are reconstructed as the missing energy
880 in the event, E_T^{miss} . Mathematically, E_T^{miss} is the negative vector sum of p_T all
881 the physics objects and an extra "soft" term. The "soft" term accounts for energy
882 deposits not associated with any of the objects in the event. For this analysis
883 the soft term is given by the sum p_T of all ID tracks not associated with objects
884 in the event. The selected tracks must be matched to the primary vertex, which
885 decreases pile-up contamination [cite G 217 218].

886 **8.5 Overlap Removal**

887 Reconstructed jets and leptons in this analysis can arise from the same energy
888 deposits. For instance, a cluster of energy from an electron can also be a valid
889 calorimeter seed for a jet. To mitigate this confusion of multiple objects originating
890 from a single jet or lepton overlapping objects are removed via a procedure referred
891 to as overlap removal. In this procedure the separation of the two objects, $\Delta(R)$,
892 determines which object is removed from the event.

893 The overlap selections used in this analysis are:

- 894 - when an electron shares a track with another electron with the lower p_T
895 electron is rejected, as it is more likely to be a fake electron
- 896 - when a muon and electron share a track the muon is rejected if it is a
897 calo-muon, otherwise the electron is rejected
- 898 - when $\Delta R < 0.2$ for an electron and jet, the jet is rejected to maximize signal
899 acceptance

- 900 - when $\Delta R > 0.2$ for an electron and jet, the electron is rejected as likely
 901 originated from decays within the jet
- 902 - when $\Delta R < \min(0.4, 0.04 + 10\text{GeV}/p_T^\mu)$ the muon is rejected, again maximiz-
 903 ing signal acceptance, otherwise the jet is rejected
- 904 - when $\Delta R < 1.0$ for the a large-R jet and electron, the jet is rejected

905 8.6 Reconstructed Resonance Mass (m_{WV})

906 The WV system mass, m_{WV} is reconstructed from the lepton, neutrino, and
 907 hadronically-decaying boson candidate. The momentum of the neutrino along the
 908 z -direction is obtained by constraining the W boson mass of the lepton neutrino
 909 system to be $80.3 \text{ GeV}/c^2$. For complex solutions to this constraint, p_Z is taken
 910 as the real component of the solution. For real solutions, the one with the smaller
 911 absolute value is used. For the resolved analysis, m_{WV} is reconstructed by con-
 912 straining the $W(Z)$ dijet system in the SRs, which improves the mass resolution:

$$913 \quad p_{T,jj}^{corr} = p_{T,jj} \times \frac{m_{W/Z}}{m_{jj}} \quad (8.6)$$

$$913 \quad m_{jj}^{corr} = m_{W/Z} \quad (8.7)$$

914 where m_{jj} and $m_{W/Z}$ are the reconstructed invariant mass of the hadronically-
 915 decaying W/Z boson and the PDG values of the W/Z boson masses, respectively.
 916 The reconstructed resonance mass is the final discriminating variable in this anal-
 917 ysis. The distribution of this variable in the CR and SRs are used in the final
 918 likelihood fit to search for evidence of an excess of events due to BSM resonances.
 919 The distribution of m_{WV} are shown in Figures 13.1-13.9.

920 **Chapter 9**

921 **Event Selection and**

922 **Categorization**

923 To search for these new resonances, the simulated background and signal sam-
924 ples are analyzed to determine a series of optimized cuts are used create signal
925 regions (SR) to identify the leptonic and hadronic decay products of the reso-
926 nance. In these regions, the resonance mass is calculated as the combined system
927 mass of the leptonic and hadronic systems as described in 8.6. The expected res-
928 onance mass distribution from the backgrounds and signal samples are compared
929 to data to search for the existence of these BSM signals (also known as a "bump
930 hunt"). Control regions enriched in the dominant backgrounds, $t\bar{t}$ and $W+\text{jets}$
931 (TCR and WCR, respectively) are constructed to be orthogonal to SRs and used
932 to determine the normalization of the $t\bar{t}$ and $W+\text{jets}$ backgrounds in SRs.

933 Events are classified as produced via non-VBF or VBF modes using a Re-
934 curisve Neural Network described in 9.3. VBF W' and Z' and ggF W' and Z'
935 resonances studied have unique SR and CR selections to maximize analysis sen-
936 sitivity. RS Graviton signals are probed using the same selections as the ggF Z'
937 signal. Additionally, more massive resonances are more likely to have boosted

938 W/Z bosons. As the boost of the hadronically decaying boson increases the sepa-
939 ration of its hadronic decay products decreases. When the hadronically decaying
940 boson has sufficient boost, the two quarks will overlap and not be identified sep-
941 arately. For this reason, a set of "resolved" selections are used when the hadronic
942 decay products are reconstructed separately, and "merged" selections when the
943 decay products overlap and identified as a single object in the event. A W/Z
944 tagger identifies merged jets as originating from a W/Z bosons based on jet sub-
945 structure and mass cuts. However, the more boosted the jet is the less likely it is
946 to pass the jet substructure cut, due to track merging. Consequently, the merged
947 selection uses a high purity region (HP), which requires that the jet pass both
948 cuts, and low purity (LP) region where the jet can fail the jet substructure cut.
949 These selections are summarized in 9.4.

950 The aforementioned SR definitions veto events with b -jets to minimize $t\bar{t}$ con-
951 tamination. However, b -jets are anticipated from W' resonances from the hadron-
952 ically decaying Z boson. To increase the signal acceptance of these resonances,
953 a $Z \rightarrow bb$ tagger is used to construct additional SR and CRs called the "tagged"
954 regions (and "untagged" if the event fails the $Z \rightarrow bb$ tagger).

955 9.1 Pre-selection

956 Before applying topological cuts, preselection cuts are applied which include
957 trigger and event requirements to reduce background contamination and the dataset
958 size. Events must contain exactly one tight lepton (no additional loose leptons),
959 the $p_T^{\ell\nu} > 75$ GeV, and there must be at least two small-R jets or one large-R jet,
960 so the event is able to pass the resolved or merged selections.

961 **9.2 Trigger**

962 The data were collected using the lowest unprescaled single-lepton or E_T^{miss}
963 triggers, as summarized in Table 9.1. Since the muon term is not considered in the
964 trigger E_T^{miss} calculation, the E_T^{miss} trigger is fully efficient to events with high- p_T
965 muons. For this reason, the E_T^{miss} trigger is used for events where $p_T^\mu > 150 \text{ GeV}$, to
966 compensate for the poor efficiency of the single muon trigger above $p_T^\mu > 150 \text{ GeV}$.

≈

Table 9.1: The list of triggers used in the analysis.

Data-taking period	$e\nu qq$ channel	$\mu\nu qq$ ($p_T(\mu\nu) < 150$ GeV) channel	$\mu\nu qq$ ($p_T(\mu\nu) > 150$ GeV) channel
2015	HLT_e24_lhmedium_L1EM20 OR HLT_e60_lhmedium OR HLT_e120_lhloose	HLT_mu20_iloose_L1MU15 OR HLT_mu50	HLT_xe70
2016a (run < 302919) $(L < 1.0 \times 10^{34} \text{ cm}^{-2} \text{s}^{-1})$	HLT_e26_lhtight_nod0_ivarloose OR HLT_e60_lhmedium_nod0 OR HLT_e140_lhloose_nod0 HLT_e300_etcut	HLT_mu26_ivarmedium OR HLT_mu50	HLT_xe90_mht_L1XE50
2016b (run ≥ 302919) $(L < 1.7 \times 10^{34} \text{ cm}^{-2} \text{s}^{-1})$	same as above	same as above	HLT_xe110_mht_L1XE50
2017	same as above	same as above	HLT_xe110_pufit_L1XE55
2018	same as above	same as above	HLT_xe110_pufit_xe70_L1XE50

967 **9.3 non-VBF/VBF RNN**

968 To classify events as originating from non-VBF or VBF production a recursive
969 neural network (RNN [24]) is used. This approach is more powerful than a cut-
970 based classification as it improves signal efficiency and analysis sensitivity by
971 exploiting correlations between variables that the RNN learns. In particular, a
972 RNN architecture is ideal as it can handle variable numbers of jets in the events.

973 The RNN uses the four-momentum of candidate VBF jets to classify events
974 as VBF or non-VBF topologies. Sometimes jets are incorrectly reconstructed,
975 so the number of jets in the event is expected to vary across the input samples.
976 VBF candidate jets are identified by removing jets from the event that are likely
977 from $W/Z \rightarrow qq$. For the resolved regime this means removing the two leading
978 small-R jets from the VBF candidate jet list. For the merged regime this means
979 removing small-R jets separated by less than 1.0 in dR from the large-R jet. VBF
980 candidate jets are also required to be within $|\eta| < 4.5$. From the list of remaining
981 VBF candidate jets, the two highest- p_T jets are chosen.

982 The architecture of the RNN is shown in Figure 9.2. The RNN is composed
983 of Long Short Term Memory Cells (LSTM) that extract meaningful information
984 and retain it. The logic embedded in the LSTM is shown in Figure ???. LSTMs
985 are useful for VBF event classification for events with two jets, where using the
986 kinematic properties of both jets (and their correlations) will lead to more efficient
987 event classification.

988 In this RNN architecture, the VBF candidates are first passed to a masking
989 layer which checks the number of jets in the event. If there is only one jet, only one
990 vertical LSTM layer is used. The output of masking is then passed to a LSTM,
991 with a tanh activation function. The output of the LSTM is then passed to a
992 second horizontal LSTM layer (and vertical LSTM layer if there are two jets in

993 the event). Finally the output of the last LSTM cell is passed to a dense layer
994 and then to a sigmoid activation layer, leading to an overall RNN score.

995 The weights and other parameters of the network are learned by training the
996 network with HVT VBF and non-VBF signals and all simulated backgrounds over
997 200 epochs with an Adam Optimizer [16]. To prevent overfitting during training,
998 dropout is applied to RNN weights and training is truncated if the network pa-
999 rameters are unchanged after ten iterations [26]. Figure 9.4 shows the ROC curve
1000 for the RNN using k-fold cross validation [22].

1001 Figure 9.3 shows the RNN discriminant for backgrounds, non-VBF signals,
1002 and VBF signals. The RNN score is ~ 0 for non-VBF signals and background
1003 processes and ~ 1 for VBF processes. Figure 9.5 shows the limits for various signal
1004 processes based on the RNN cut applied. Requiring the RNN score to be > 0.8
1005 was chosen as it provided the best analysis significance for this final state and
1006 the $\nu\nu qq$ and $\ell\ell qq$ channels, which this channel will be combined with for future
1007 publications.

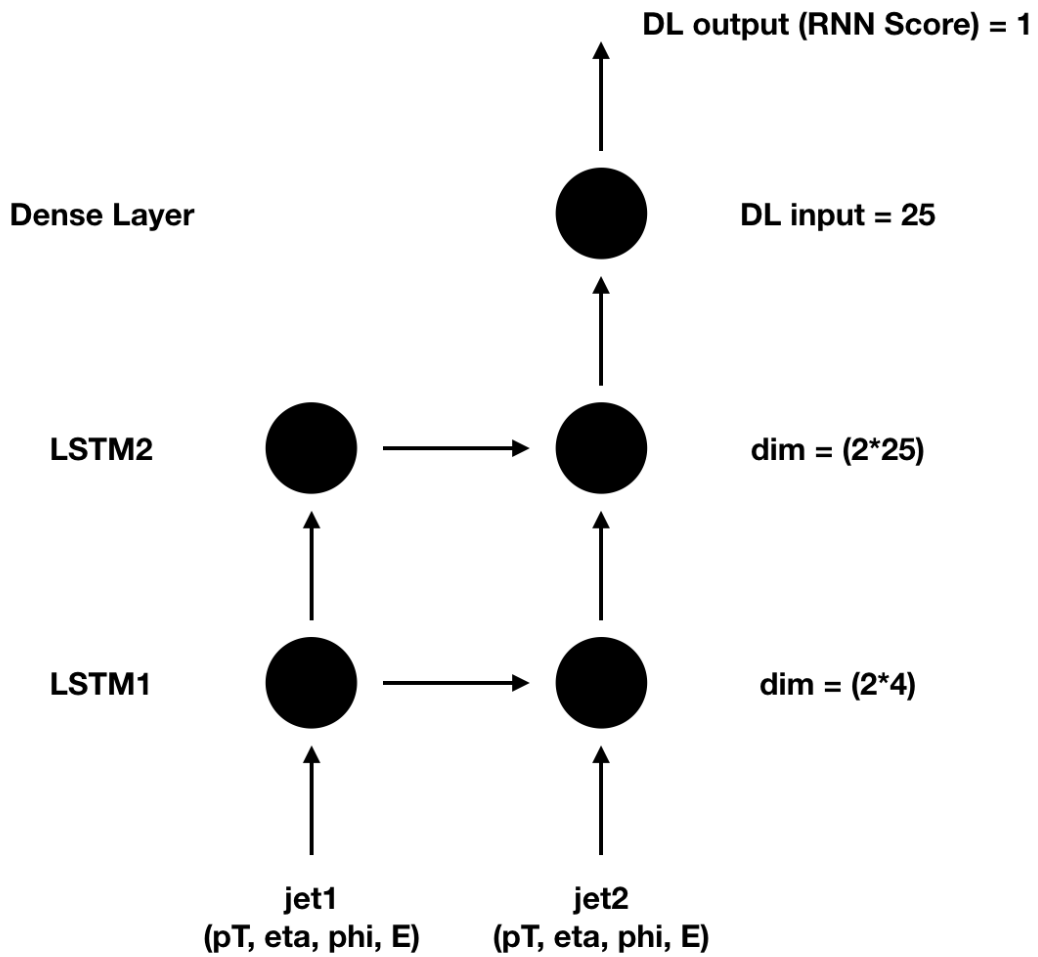


Figure 9.1: RNN architecture. Natasha add caption

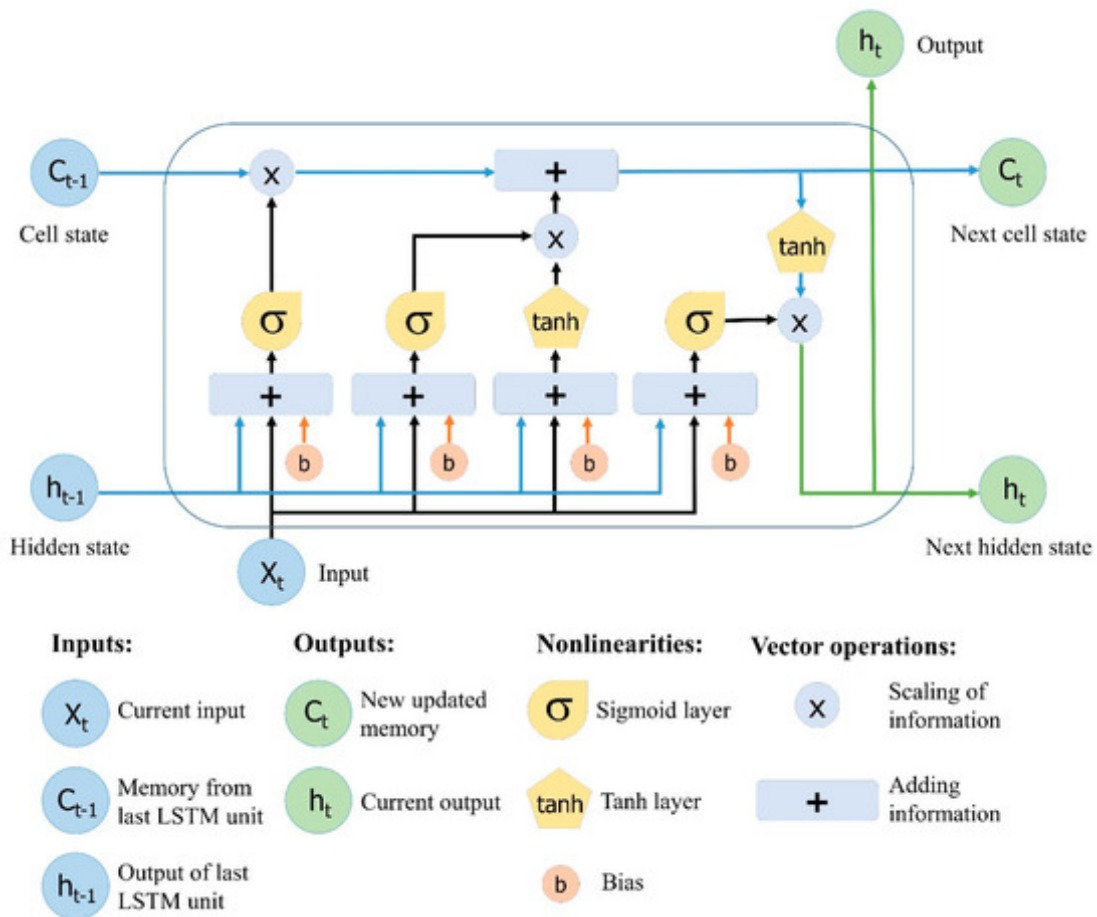


Figure 9.2: This figure shows the embedded logic in LSTM cells. This image was taken from [25], where a more in depth discussion about LSTMs may be found.

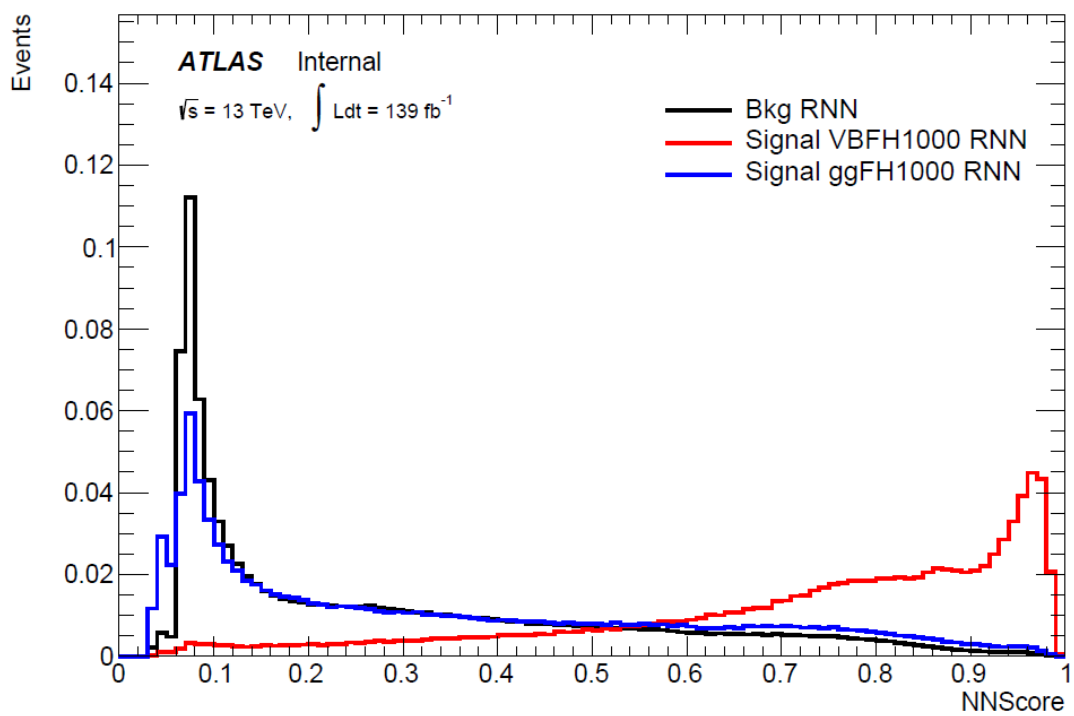


Figure 9.3: RNN Score distribution for ggF and VBF signals and backgrounds.

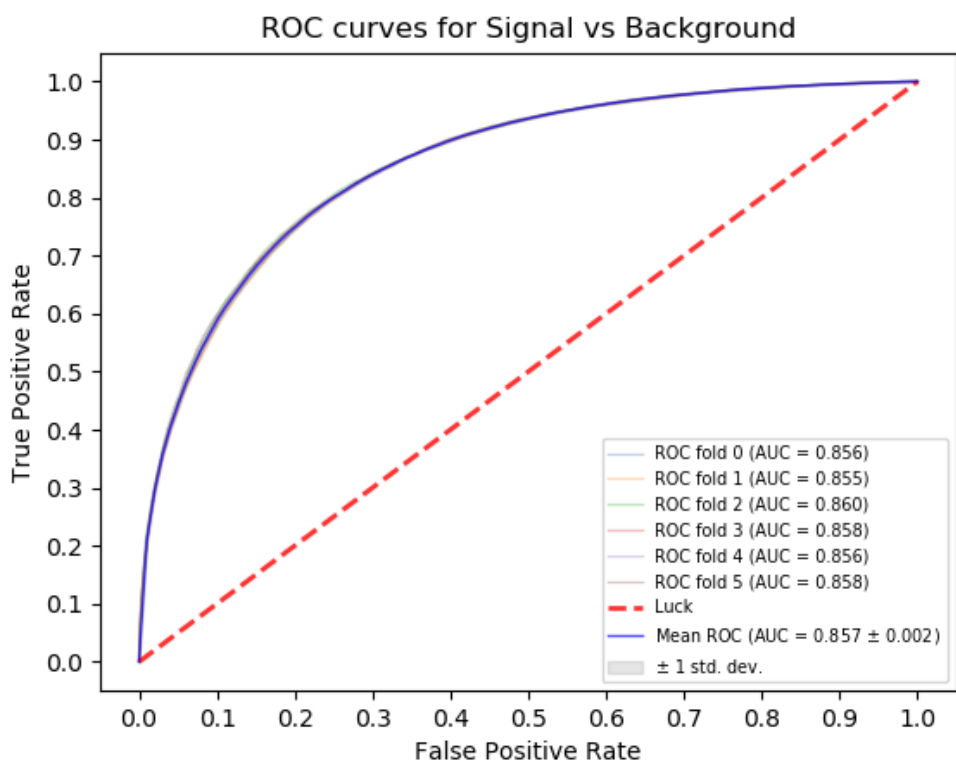


Figure 9.4: ROC curve using k-fold validation for RNN.

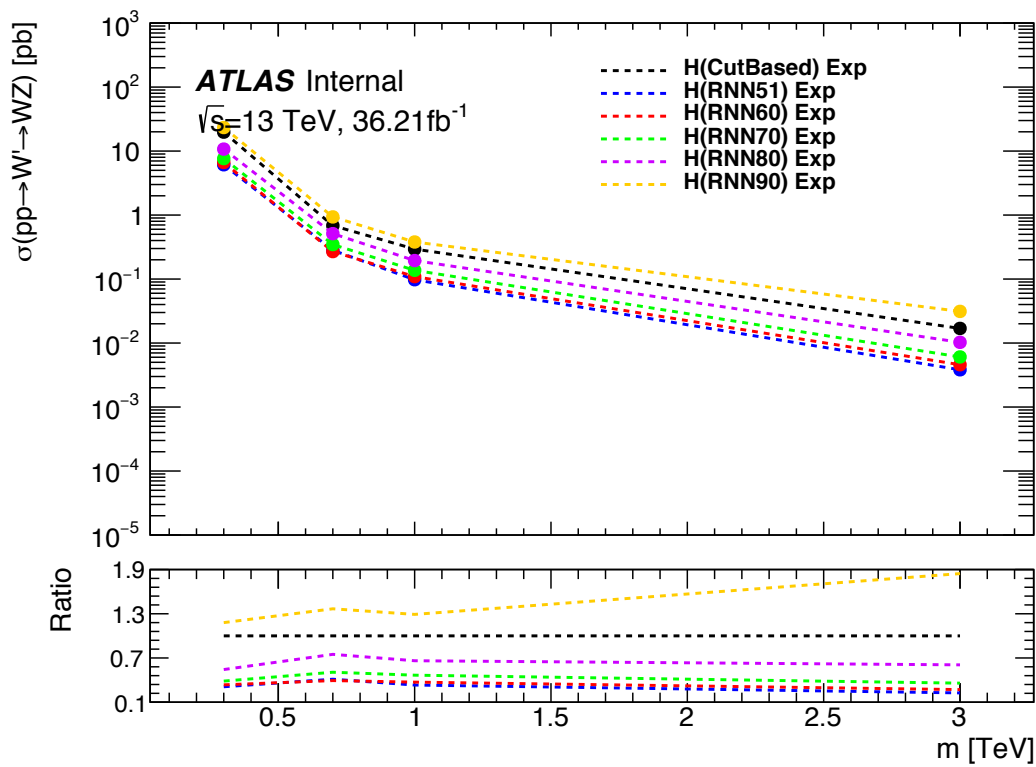


Figure 9.5: Comparison of GGF Z' limits for different RNN score selections. The bottom panel shows the ratio of the upper limits set for different RNN cuts to the cut-based analysis. In this panel smaller numbers, indicate that the expected upper limit is smaller than the cut-based analysis, which is desired.

1008 9.4 Signal Region Definitions

1009 Signal regions are constructed to be dominated by signal and used in the final
1010 likelihood fit to look for a bump in the reconstructed resonance mass distribution.
1011 Once an event is classified by the RNN, it must pass topological cuts that maximize
1012 S/\sqrt{B} . To efficiently select events with a $W \rightarrow \ell\nu$ candidate exactly one tight
1013 lepton is required and $E_T^{miss} > 100(60)$ GeV and $p_{T,\ell\nu} > 200(75)$ GeV in the
1014 merged (resolved) analysis to suppress the fake lepton backgrounds.

1015 The resonances this search probes are expected to be produced approximately
1016 at rest with the two resulting bosons produced back-to-back. For this reason,
1017 it is required that the minimum value of $(p_{T,\ell\nu}, p_{T,J})/m_{WV} > 0.35(0.25)$ for the
1018 non-VBF (VBF) category.

1019 To reduce $t\bar{t}$ contamination in the merged HVT Z' and G_{KK} analyses, events
1020 with at least one b -jet with $\Delta R > 1.0$ from the large-R jet are excluded. High
1021 purity signal regions require the D_2 and W/Z mass window cut to be passed,
1022 whereas the low purity region only requires the W/Z mass window cut to be
1023 passed. More boosted jets, are more likely to fail the D_2 cut due to track merging.
1024 Therefore, by using high and low purity regions, the signal acceptance is increased.

1025 The HVT W' resonance search uses tagged and untagged regions to minimize
1026 backgrounds and increase signal acceptance. For events to be classified as tagged
1027 the large-R jet must contain exactly two b -tagged VR jets. Untagged events must
1028 have no more than one b -tagged jet matched to the large-R jet. These selections
1029 are shown in Table 9.2.

1030 Events failing the merged selection are then re-analyzed in the resolved cat-
1031 egory. To enhance resolved signals, the event should contain two high- p_T boson
1032 candidates that are back-to-back in the ϕ as shown by the selections in Table 9.3.
1033 Again, to suppress the $t\bar{t}$ backgrounds, events are required to have no additional

Table 9.2: Summary of selection criteria used to define the signal region (SR), W +jets control region (W CR) and $t\bar{t}$ control region ($t\bar{t}$ CR) for merged 1-lepton channel.

Selection		SR		W CR (WR)		$t\bar{t}$ CR (TR1)	
		HP	LP	HP	LP	HP	LP
$W \rightarrow \ell\nu$	Num of Tight leptons	1					
	Num of Loose leptons	0					
	E_T^{miss}	$> 100 \text{ GeV}$					
	$p_T(\ell\nu)$	$> 200 \text{ GeV}$					
$W/Z \rightarrow J$	Num of large- R jets	≥ 1					
	D_2 cut	pass	fail	pass	fail	pass	fail
	W/Z mass window cut	pass	pass	fail	fail	pass	pass
	Numb. of associated VR track jets b -tagged	For $Z \rightarrow J$: ≤ 1 ($= 2$) for untagged (tagged) category					
	$\min(p_{T,\ell\nu}, p_{T,J}) / m_{WV}$	$> 0.35(0.25)$ for DY/ggF (VBF) category					
	Top-quark veto	Num of b -tagged jets outside of large- R jet	0	≥ 1			
Pass VBF selection			no (yes) for DY/ggF (VBF) category				

1034 b -jets for the HVT Z' and G_{KK} analyses. A summary of the resolved selections
 1035 is shown in Table 9.3.

1036 The analysis cutflow in Figure 9.6 shows how the different categories are pri-
 1037 oritized. Events classified as VBF events are classified as merged high purity, low
 1038 purity or resolved signal region selections sequentially. If the event does not pass
 1039 any of these selections but passes a VBF control region selection it is classified as
 1040 a VBF CR event.

1041 If the event fails all VBF categories, it is then checked if it passes the merged
 1042 high purity, low purity or resolved signal region selections (NB: for the WZ decay
 1043 modes all the regions have tagged and untagged categories). If the event fails all
 1044 the non-VBF signal region selections, it is then kept for non-VBF control region
 1045 selections, if it passes those selections. Control region selection are discussed more
 1046 in 10.1.

1047 Overall, for the Drell-Yan HVT Z' and gluon-gluon fusion G_{KK} signals there
 1048 are 3 signal regions. For the Drell-Yan HVT W' signal there are 6 signal regions.
 1049 For VBF HVT W' and Z' signals there are 3 signal regions.

Table 9.3: The list of selection cuts in the resolved analysis for the WW and WZ signal regions (SR), $W+jets$ control region (WR) and $t\bar{t}$ control region (TR).

cuts	SR	W CR (WR)	$t\bar{t}$ CR (TR1)		
$W \rightarrow \ell\nu$	Number of Tight leptons	1			
	Number of Loose leptons	0			
	E_T^{miss}	> 60 GeV			
	$\cancel{p}_T(\ell\nu)$	> 75 GeV			
$W/Z \rightarrow jj$	Number of small-R jets	≥ 2			
	Leading jet p_T	> 60 GeV			
	Subleading jet p_T	> 45 GeV			
	$Z \rightarrow q\bar{q}$	$78 < m_{jj} < 105$ GeV	$50 < m_{jj} < 68$ GeV or $68 < m_{jj} < 98$ GeV	$105 < m_{jj} < 150$ GeV	$50 < m_{jj} < 150$ GeV
	Num. of b -tagged jets	For $Z \rightarrow jj$: ≤ 1 ($= 2$) for untagged (tagged) category			
Topology cuts	$\Delta\phi(j, \ell)$	> 1.0			
	$\Delta\phi(j, E_T^{\text{miss}})$	> 1.0			
	$\Delta\phi(j, j)$	< 1.5			
	$\Delta\phi(\ell, E_T^{\text{miss}})$	< 1.5			
	$\min(p_{T,\ell\nu}, p_{T,jj}) / m_{WV}$	> 0.35(0.25) for DY/ggF (VBF) category			
Top veto	Number of additional b -tagged jets	0	≥ 1		
	Pass VBF selection	no (yes) for DY/ggF (VBF) category			

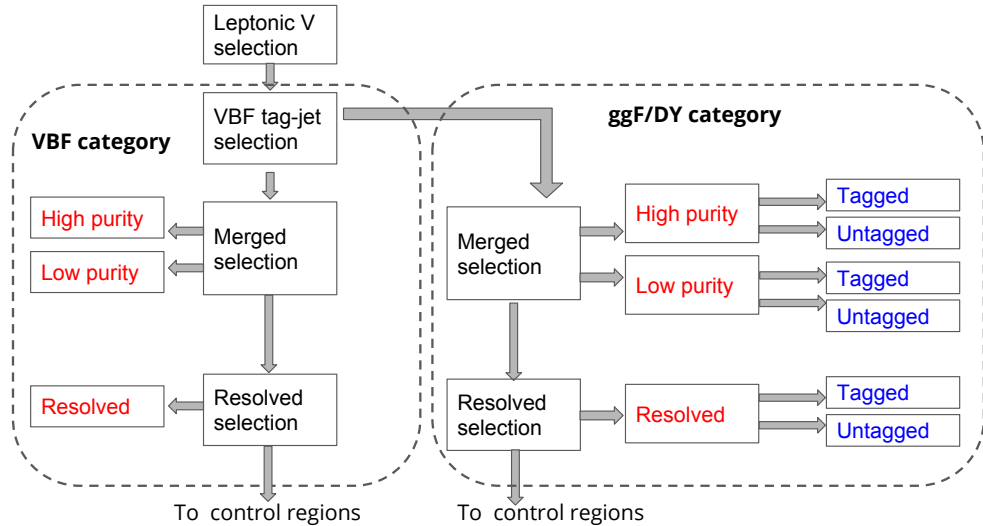


Figure 9.6: Event Categorization. Natasha write more.

1050 9.5 Selection Acceptance and Efficiency

1051 The signal acceptance is the ratio of the number of signal events selected to
 1052 the number of signal events generated at truth level, which does not account for

1053 detector effects. The signal efficiency is the ratio of the number of reconstructed
 1054 events selected and the number of truth events selected, which accounts for de-
 1055 tector effects. The expected number of signal events is given by the product of
 1056 these two quantities:

$$A \cdot \epsilon = \frac{N_{\text{events selected}}^{\text{truth}}}{N_{\text{events generated}}^{\text{truth}}} \cdot \frac{N_{\text{events selected}}^{\text{reco}}}{N_{\text{events selected}}^{\text{truth}}} = \frac{N_{\text{events selected}}^{\text{reco}}}{N_{\text{events generated}}^{\text{truth}}} \quad (9.1)$$

1057 The distributions of $A \cdot \epsilon$ as a function of the resonance mass for the different spin
 1058 models are shown in Figures 9.7 - 9.8.

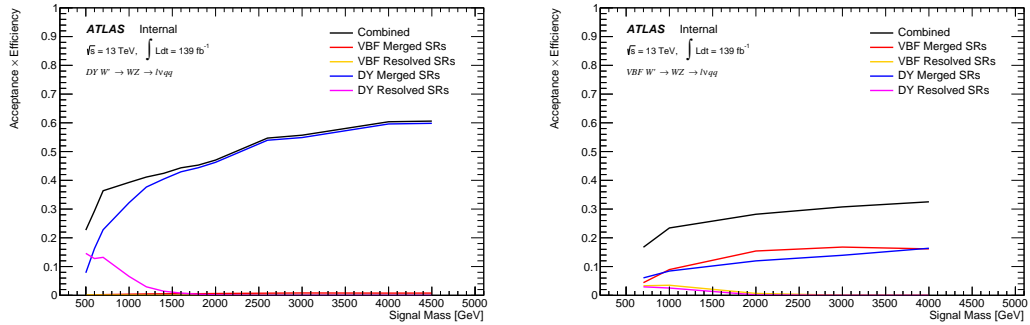


Figure 9.7: Selection acceptance times efficiency for the $W' \rightarrow WZ \rightarrow \ell\nu qq$ events from MC simulations as a function of the W' mass for Drell-Yan (left) and VBF production (right), combining the merged HP and LP signal regions of the $WV \rightarrow \ell\nu J$ selection and the resolved regions of the $WV \rightarrow \ell\nu jj$ selection. Note: the VBF selection acceptance for the DY W' is approximately zero in the left plot.

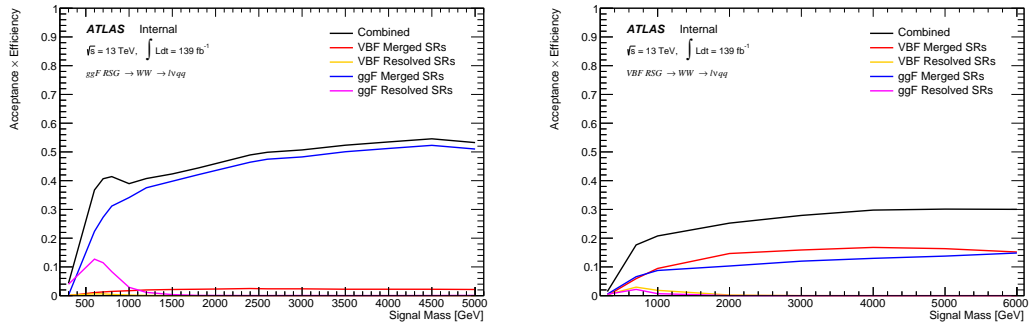


Figure 9.8: Selection acceptance times efficiency for the $G \rightarrow WW \rightarrow \ell\nu qq$ events from MC simulations as a function of the G mass for (a) Drell-Yan and (b) VBF production, combining the merged HP and LP signal regions of the $WW \rightarrow \ell\nu J$ selection and the resolved regions of the $WW \rightarrow \ell\nu jj$ selection. Note: the VBF selection acceptance for the ggF G''_{KK} is approximately zero in the left plot.

1059 **Chapter 10**

1060 **Background Estimate**

1061 Backgrounds from VV , $t\bar{t}$, single-top, $W+\text{jets}$, $Z+\text{jets}$ are simulated as de-
1062 scribed in 7.2. The dominant backgrounds for this search are from $W+\text{jet}$ and
1063 $t\bar{t}$ processes. To more accurately model the m_{VV} distribution from these back-
1064 grounds in the SRs, control regions are constructed for each as described in 10.1.
1065 The $t\bar{t}$ and $W+\text{jets}$ control regions are called TCR and WCR, respectively. There
1066 are separate control regions for VBF and non-VBF regions as well as for each
1067 region (merged HP, merged LP, resolved). For the HVT W' search there are also
1068 tagged and untagged control regions (where tagged refers to events with two b -jets
1069 inside the large-R jet).

1070 The aforementioned backgrounds containing real leptons and are well-modeled
1071 with simulated samples. Backgrounds with fake leptons (also referred to as the
1072 multijet background) are not well-modeled with simulation. For this reason, the
1073 multijet background is extracted from data as described in 10.2.

1074 10.1 Control Regions

1075 The TCRs have the same selections as the SRs, but at least one b -jet in the
1076 event (that is not within the catchement area of the large-R jet for the merged
1077 analysis). The WCR shares the SR selections, but has different jet mass require-
1078 ments. For the merged analyses, the large-R jet must fail the W/Z tagger jet mass
1079 cut. In the resolved analyses, m_{jj} must be $50 < m_{jj} < 68$ GeV or $105 < m_{jj} < 150$
1080 GeV.

1081 The distributions for some the variables used in merged analysis (e.g. reso-
1082 nance mass, $p_T(\nu)$, $p_T(J)$) for top control regions (non-VBF and VBF HP and LP
1083 regions) are shown in Figure 10.1-10.4. The distributions for the variables used
1084 in the resolved analysis (e.g. resonance mass, $p_T(\nu)$, $p_T(j_1/j_2)$) in the TCR are
1085 shown in Figure 10.5, 10.6. In general, in these plots the simulated distributions
1086 match the data well, which is necessary to have confidence in the prediction yields
1087 in the signal regions.

1088 To more accurately model the two dominant backgrounds in this analysis,
1089 W +jets and $t\bar{t}$, control regions are constructed for each. These control regions
1090 are dominated by these processes and used to extract normalization factors in
1091 the final likelihood fit that are then used in the signal region estimates. For the
1092 $t\bar{t}$ control region the event must contain at least one such b jet. The WCR is
1093 constructed using the $m_{jj/J}$ mass window sidebands. All other backgrounds are
1094 estimated using simulation, except fake lepton backgrounds, which are derived
1095 using a data-driven method.

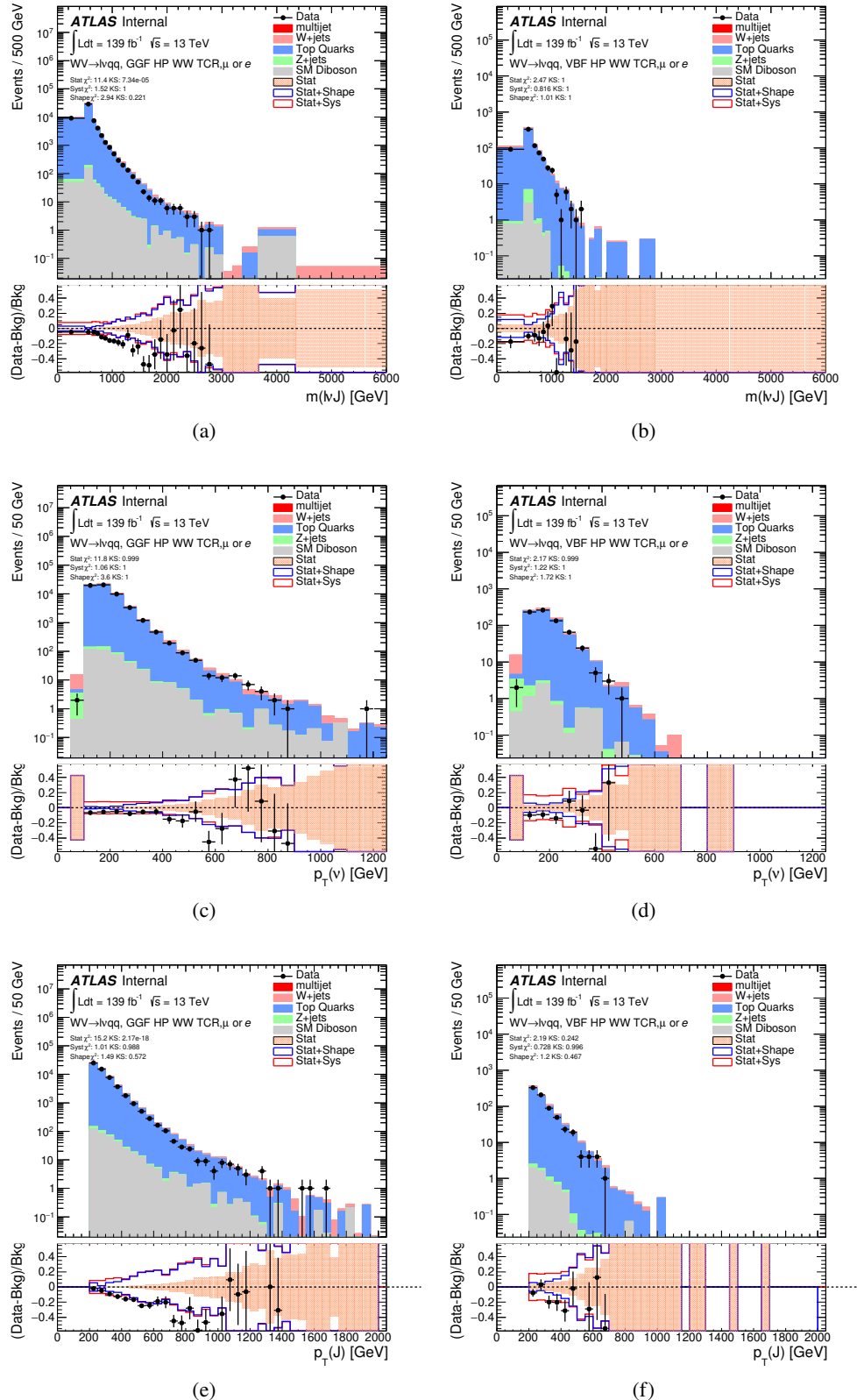


Figure 10.1: Data MC comparison for the merged WW HP TCR. The bottom panel shows the ratio of the difference between data and simulation to simulation. The red bands include the all systematic and statistical uncertainties on the background.⁹³

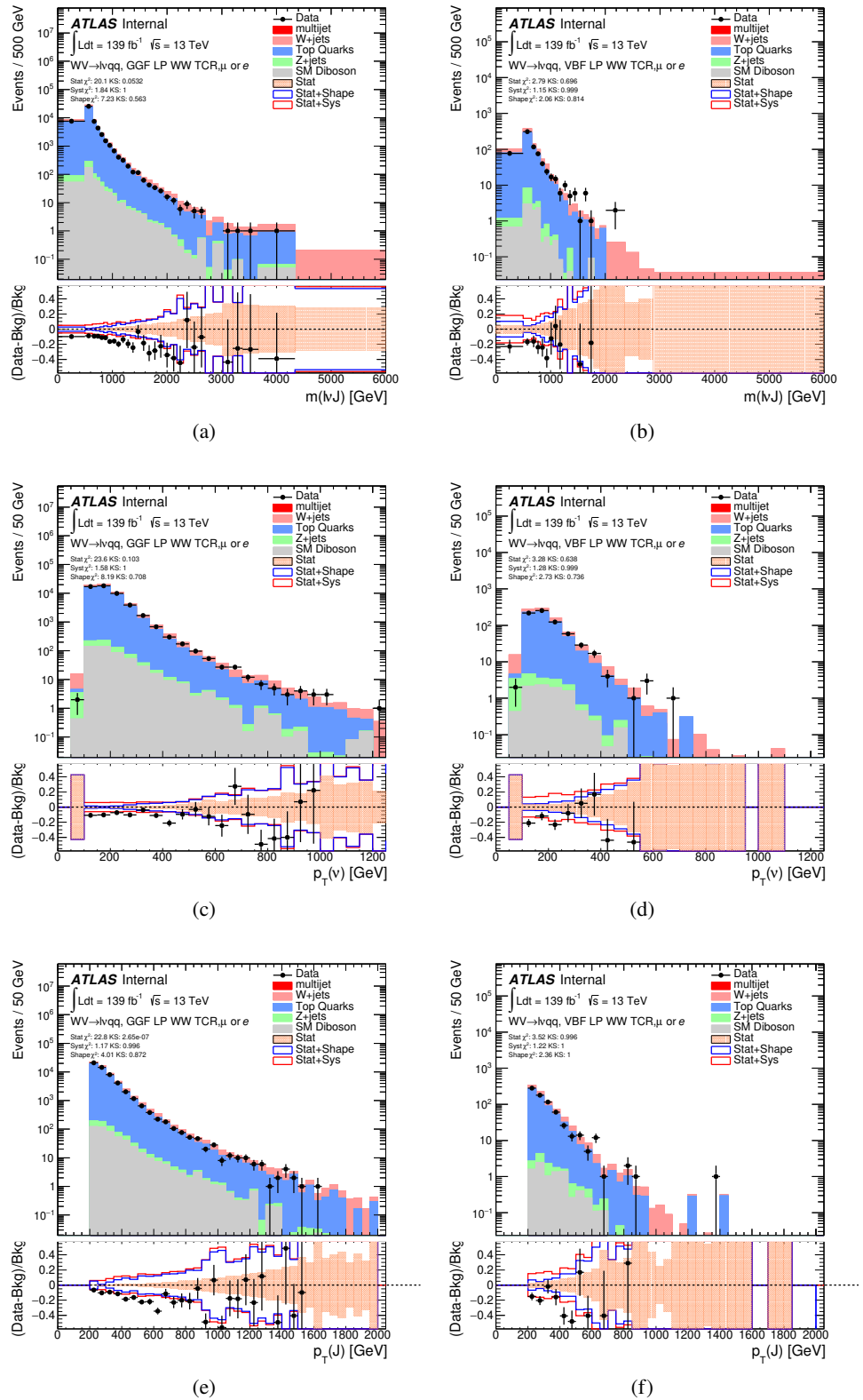


Figure 10.2: Data MC comparison for the merged WW LP TCR. The bottom panel shows the ratio of the difference between data and simulation to simulation. The red bands include the all systematic and statistical uncertainties on the background.

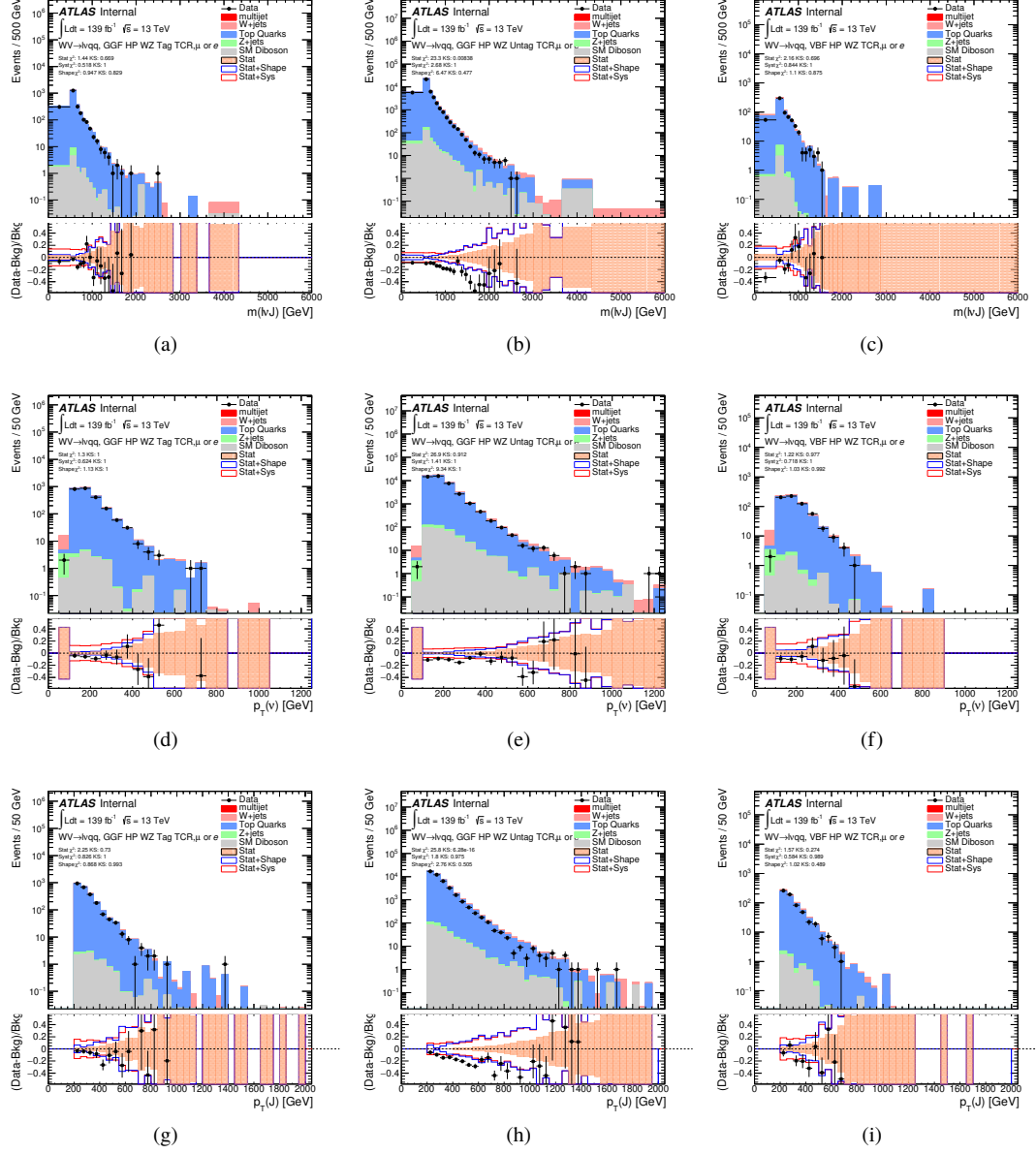


Figure 10.3: Data MC comparison for the merged WZ HP TCR. The bottom panel shows the ratio of the difference between data and simulation to simulation. The red bands include the all systematic and statistical uncertainties on the background.

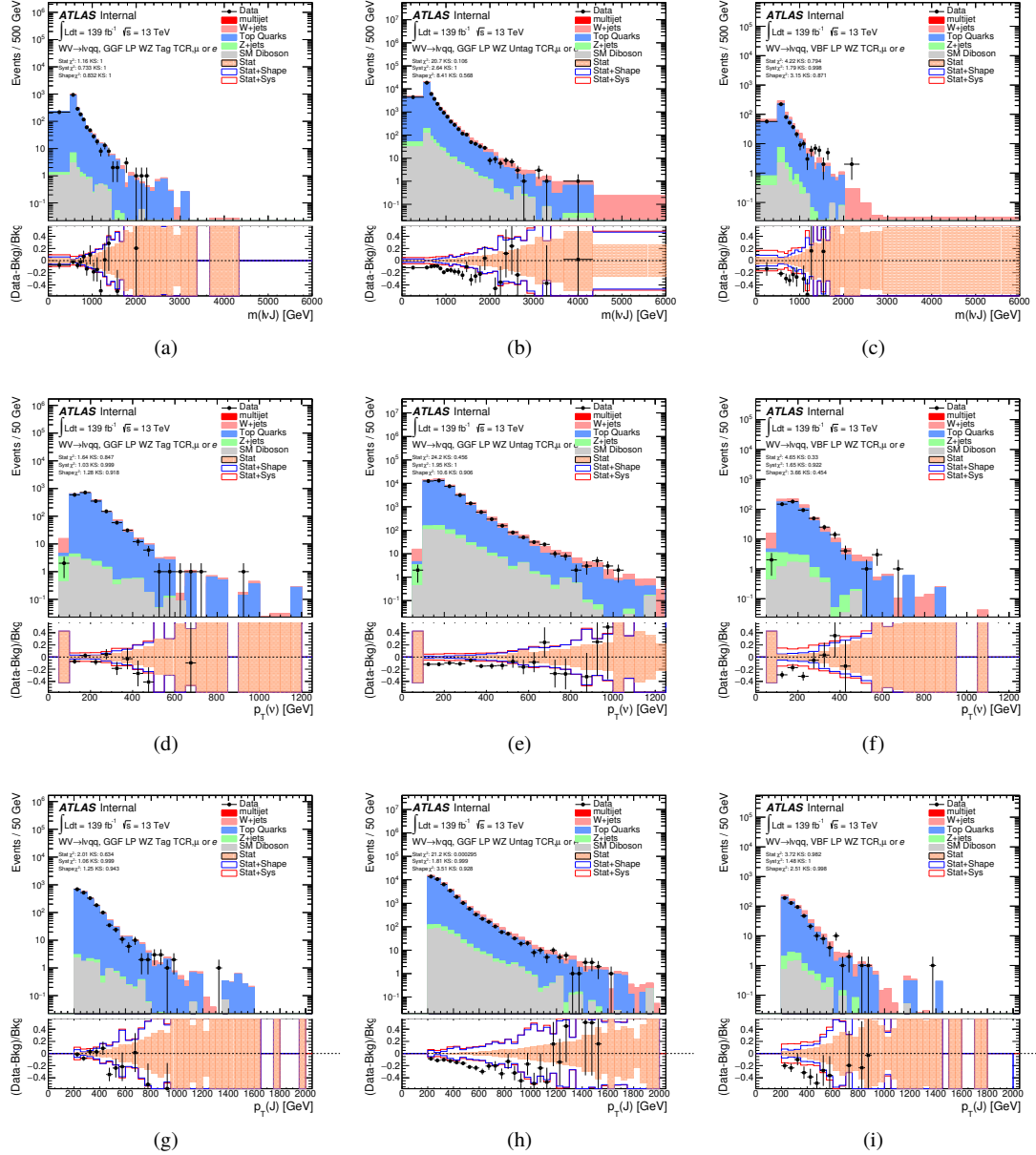


Figure 10.4: Data MC comparison for the merged WZ LP TCR. The bottom panel shows the ratio of the difference between data and simulation to simulation. The red bands include the all systematic and statistical uncertainties on the background.

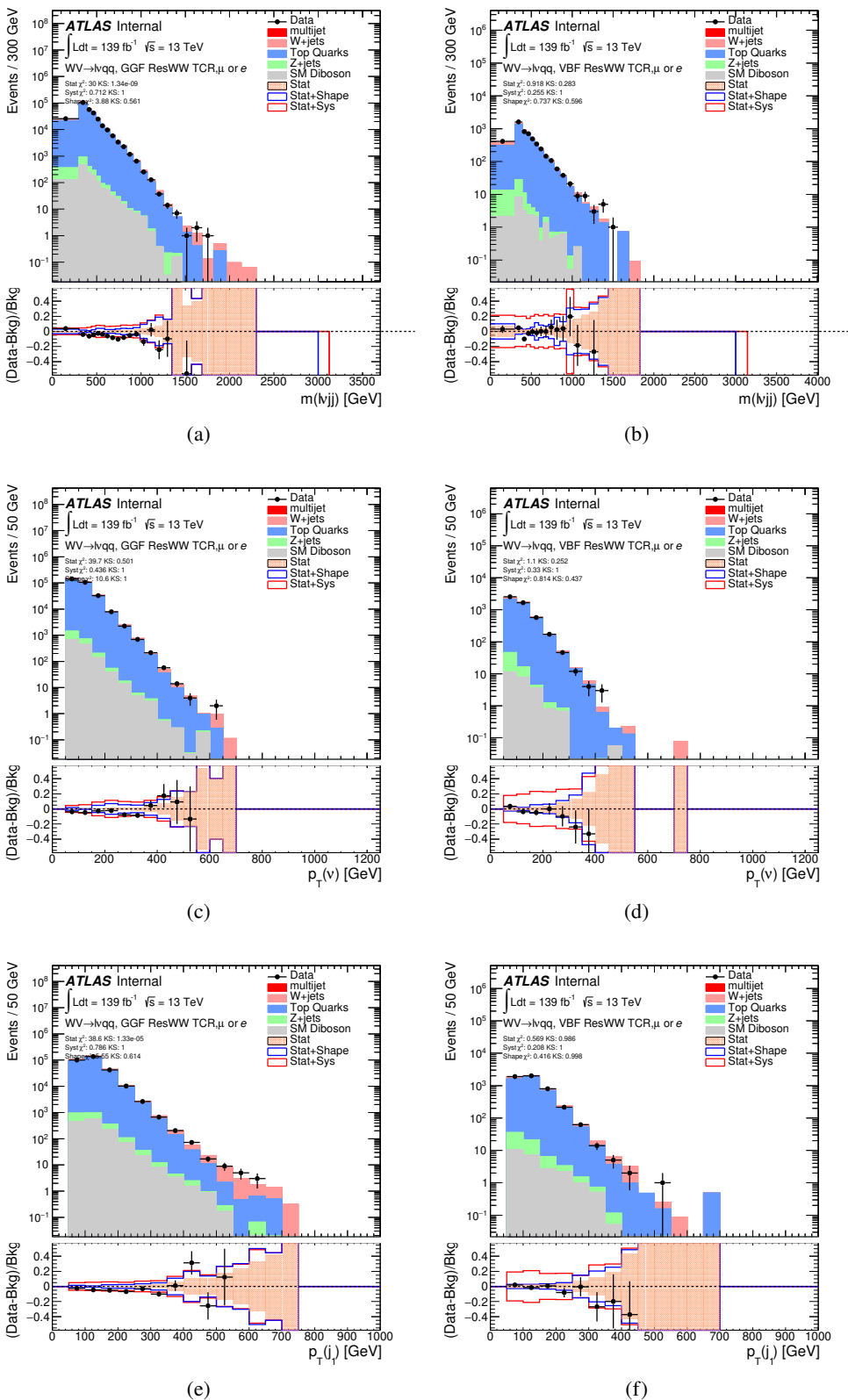


Figure 10.5: Data MC comparison for the resolved WW TCR. The bottom panel shows the ratio of the difference between data and simulation to simulation. The red bands include the all systematic and statistical uncertainties on the background.

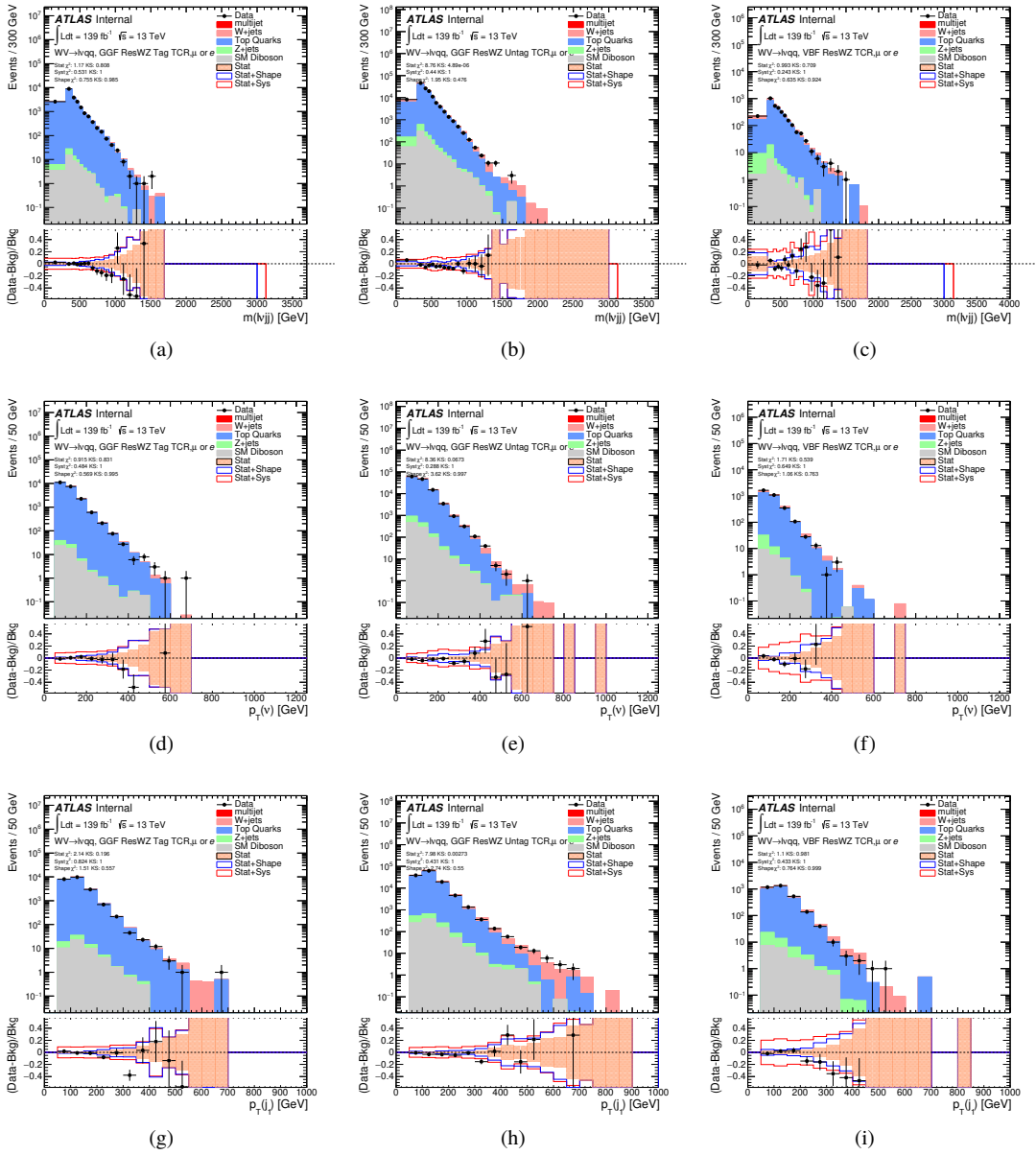


Figure 10.6: Data MC comparison for the resolved WZ TCR. The bottom panel shows the ratio of the difference between data and simulation to simulation. The red bands include the all systematic and statistical uncertainties on the background.

1096 10.2 Fake Lepton Backgrounds

1097 The fake lepton backgrounds for this search are not well-modeled with simu-
1098 lation. For this reason, this background is extracted from data. Fake electrons
1099 often arise from fake jets and converted photons while non-prompt muons usually
1100 arise from heavy flavor decay products. This predominately occurs at lower lepton
1101 momentums, and therefore is only considered in the resolved analysis.

1102 Fake electrons generally fail the electron ID criteria and fake muons fail the
1103 muon isolation requirement. Therefore, separate multijet samples are derived for
1104 the fake electron and muon samples. For each sample the m_{WV} template shape
1105 is derived for the SR and WCR selections using the same SR and WCR cuts but
1106 with inverted lepton requirements as seen in Table 10.1. NB: By inverting the
1107 lepton isolation/identification criteria the SRs and CRs are orthogonal.

1108 To derive the multijet template in a given SR, first the multijet template in
1109 the WCR is derived, called the MJCR template. This template is calculated using
1110 events that pass the WCR selection but with the inverted lepton criteria. The
1111 E_T^{miss} distribution for the MJCR is given by the difference between data and the
1112 simulated samples in the MJCR. The E_T^{miss} distribution of those events is then
1113 added to the simulated backgrounds in the WCR. The floating background and
1114 multijet normalizations of the MJCR in this region are then fit to the data. The
1115 fitted MJCR is then used as the multijet sample in the WCR.

1116 The fitted normalizations from the MJCR template are then used to construct
1117 the multijet template in the SR (MJSR). The MJSR is constructed from events
1118 that pass the SR selections but with the inverted lepton criteria. Again, the
1119 difference between the data and simulated backgrounds in this region gives MJSR
1120 template shape in m_{WV} . This shape is then scaled by the fitted normalizations
1121 from the MJCR. These fitted electron and muon multijet templates are then

1122 used as the multijet samples in the SRs. The normalizations of the electron and
1123 muon multijet samples are parameters in the final likelihood fit.

1124 This template method was validated using WCR and full Run 2 data. The
1125 results of the fit are shown in Table 10.2. The multijet contribution in the muon
1126 channel for $p_T^W > 150$ GeV is consistent with zero, and therefore neglected in
1127 the final fit. Applying the extracted normalization factor to MJCR in WCRs for
1128 various kinematic variables such as E_T^{miss} , W transverse mass, lepton p_T , and the
1129 invariant mass as show in Figures 10.8 -10.17. These figures show good agreement
1130 between the data and background estimate.

Table 10.1: Definitions of “inverted” leptons used in multijet control region. For the inverted muon selection, $ptvarcone30$ is given by sum of the p_T of tracks in a cone around the muon candidate divided by the muon p_T . The size of the cone, δR used is $10\text{GeV}/p_T^\mu$ or 0.3, whichever is smaller. So, as the p_T of the muon increases, the cone size used decreases. This is useful as more boosted muons are more likely to be produced in dense environments and using a smaller cone size more accurately determines the quality of the muon.

	Criterion	signal lepton	inverted lepton
Electron	ID	TightLH	MediumLH !TightLH
	Calo Isolation	FixedCutHighPtCaloOnlyIso	FixedCutHighPtCaloOnlyIso
Muon	ID	WHSignalMuon	WHSignalMuon
	Track Isolation	FixedCutTightTrackOnlyIso	!FixedCutTightTrackOnlyIso $ptvarcone30/p_T < 0.07^*$

*Only applied to events with $pTW < 150\text{GeV}$

1131

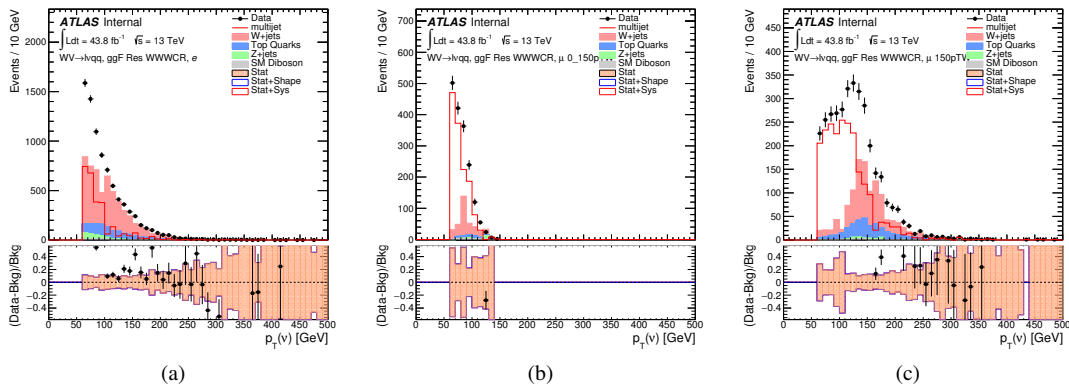


Figure 10.7: The E_T^{miss} distribution in MJCR for 2017 data in the electron channel(left), muon channel with W-boson $p_T < 150$ GeV (center) and > 150 GeV (right). Multi-jet templates are given by the difference between the data and simulated distributions.

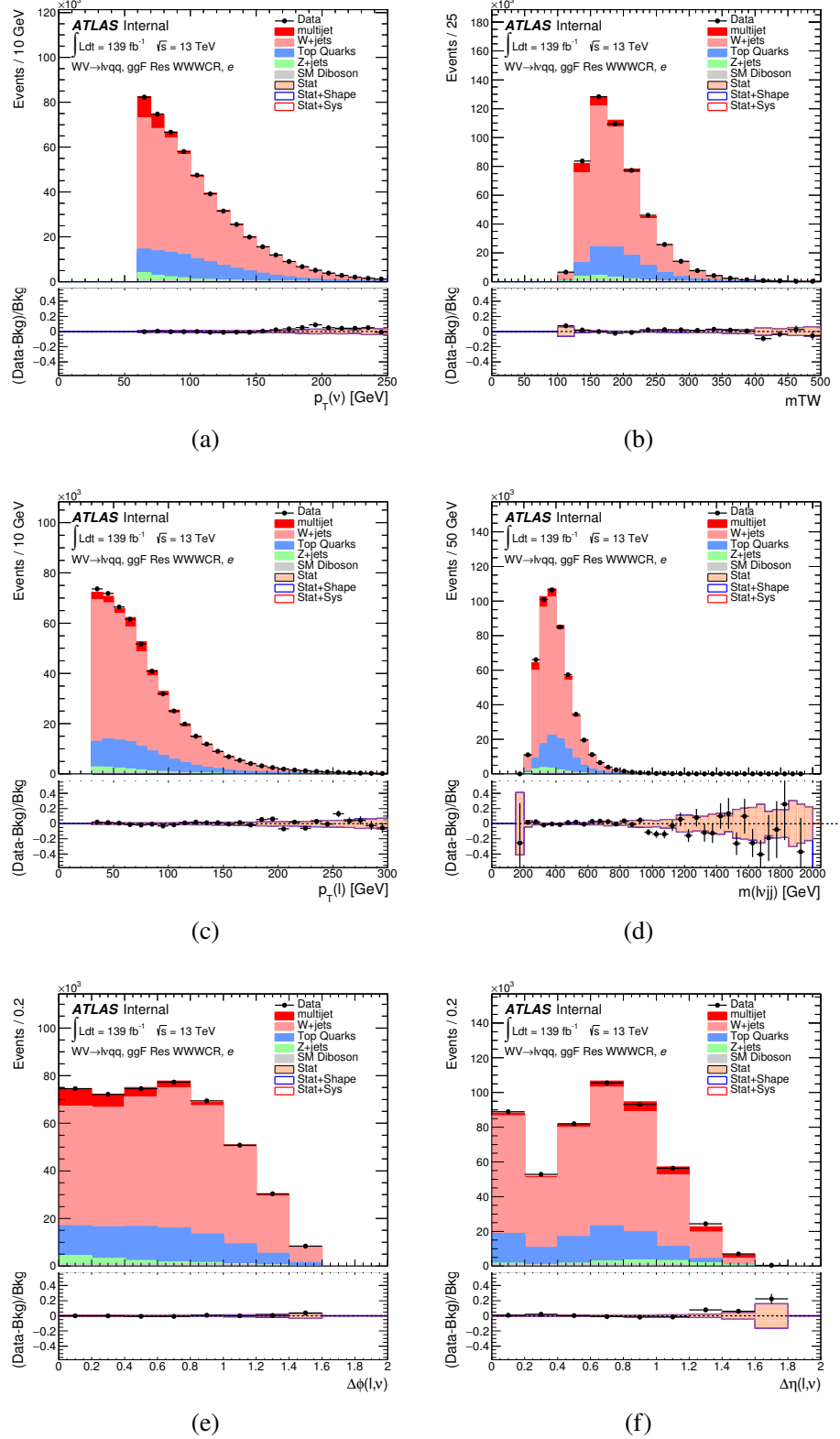


Figure 10.8: Postfit Data/MC comparison of distributions of E_T^{miss} , m_T^W , lepton and neutrino p_T , $m_{\ell\nu jj}$, lepton- ν angular distance in the WW electron channel. The MJ template is obtained from the pre-MJ-fit.

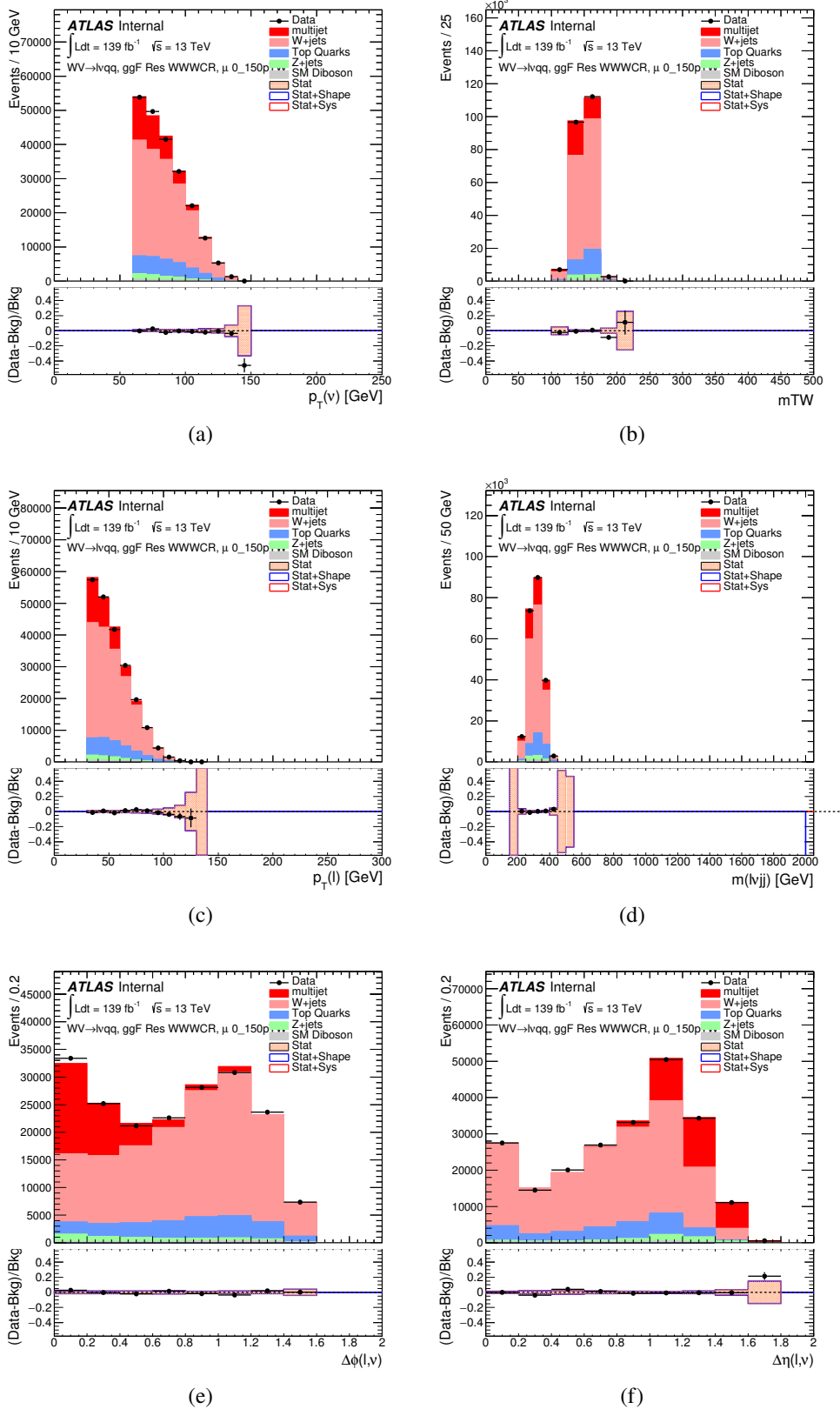


Figure 10.9: Postfit Data/MC comparison of distributions of E_T^{miss} , m_T^W , lepton and neutrino p_T , $m_{l\nu jj}$, lepton- ν angular distance in the WW muon channel. The MJ template is obtained from the pre-MJ-fit.

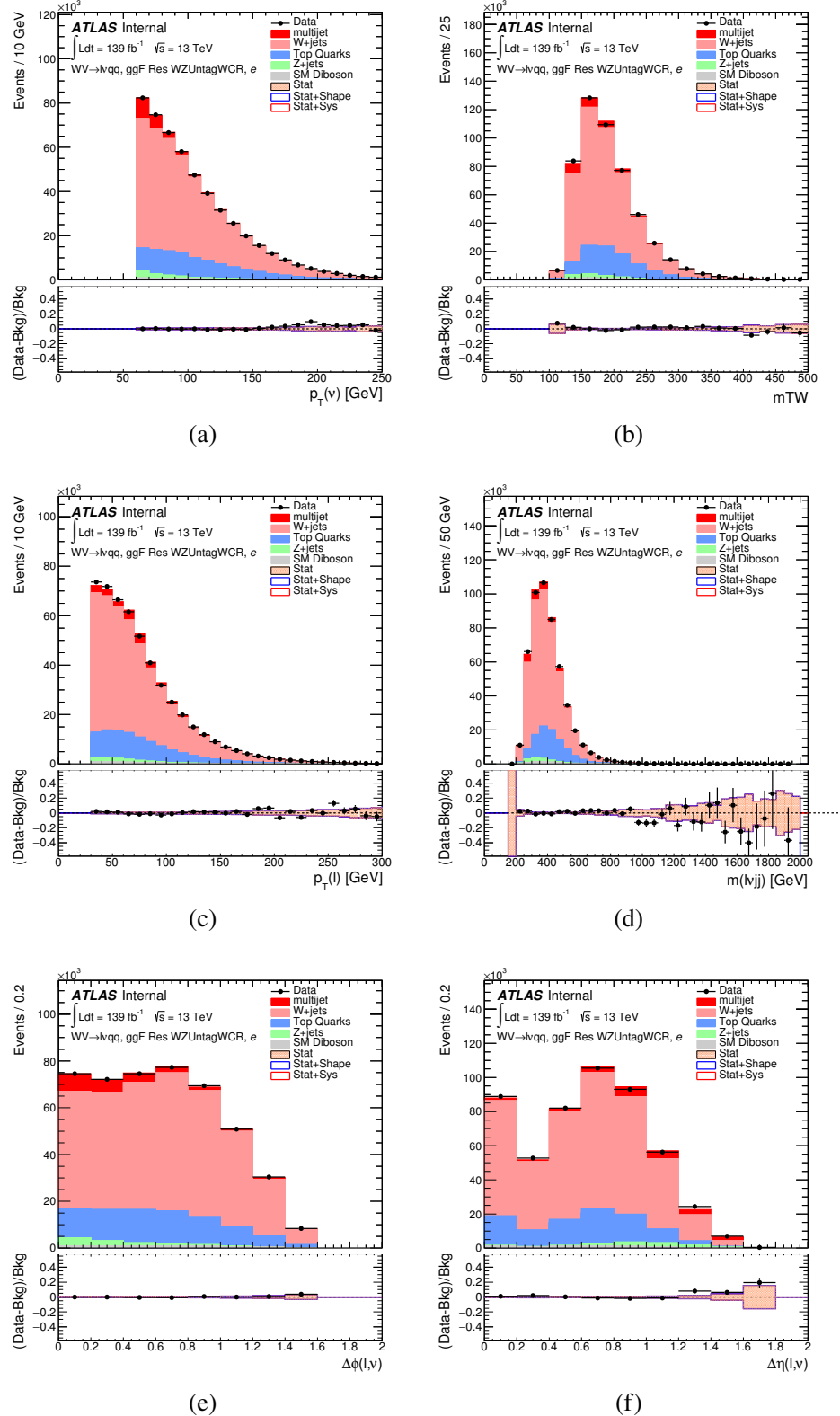


Figure 10.10: Postfit Data/MC comparison of distributions of E_T^{miss} , m_T^W , lepton and neutrino p_T , $m_{\ell\nu jj}$, lepton- ν angular distance in the WZ untag electron channel. The MJ template is obtained from the pre-MJ-fit.

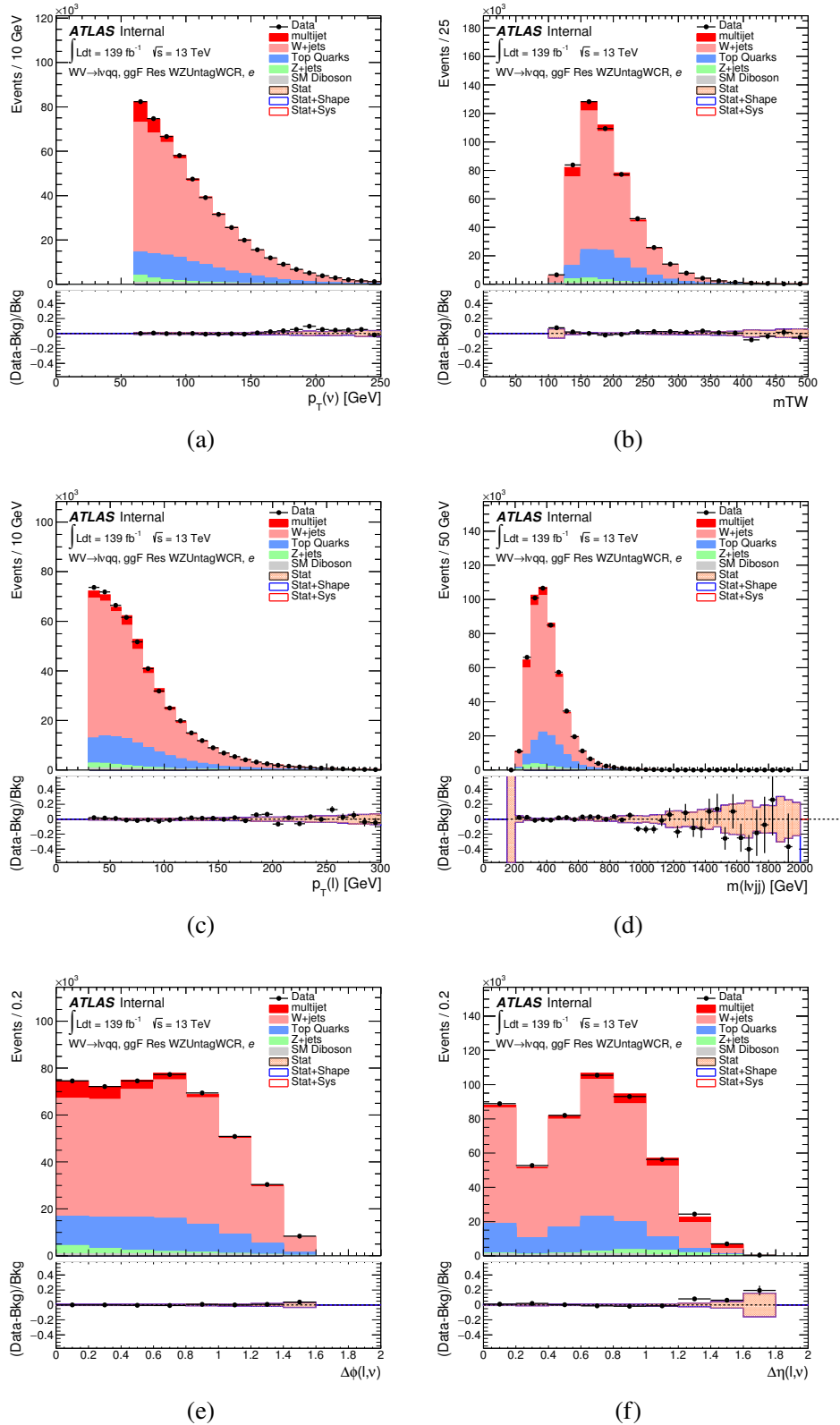


Figure 10.11: Postfit Data/MC comparison of distributions of E_T^{miss} , m_T^W , lepton and neutrino p_T , $m_{\ell\nu jj}$, lepton- ν angular distance in the WZ untag muon channel. The MJ template is obtained from the pre-MJ-fit.

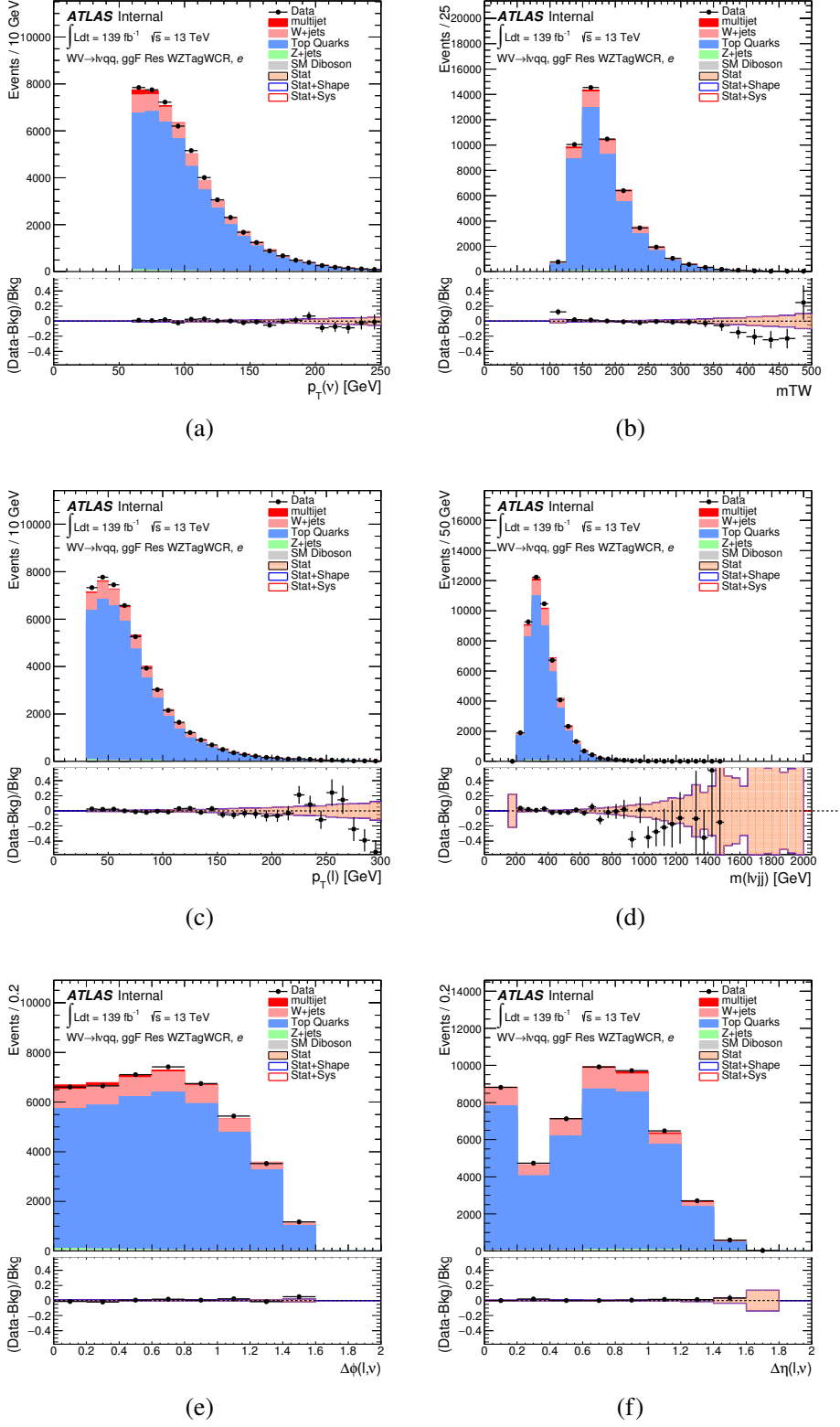


Figure 10.12: Postfit Data/MC comparison of distributions of E_T^{miss} , m_T^W , lepton and neutrino p_T , $m_{l\nu jj}$, lepton- ν angular distance in the WZ untag electron channel. The MJ template is obtained from the pre-MJ-fit.

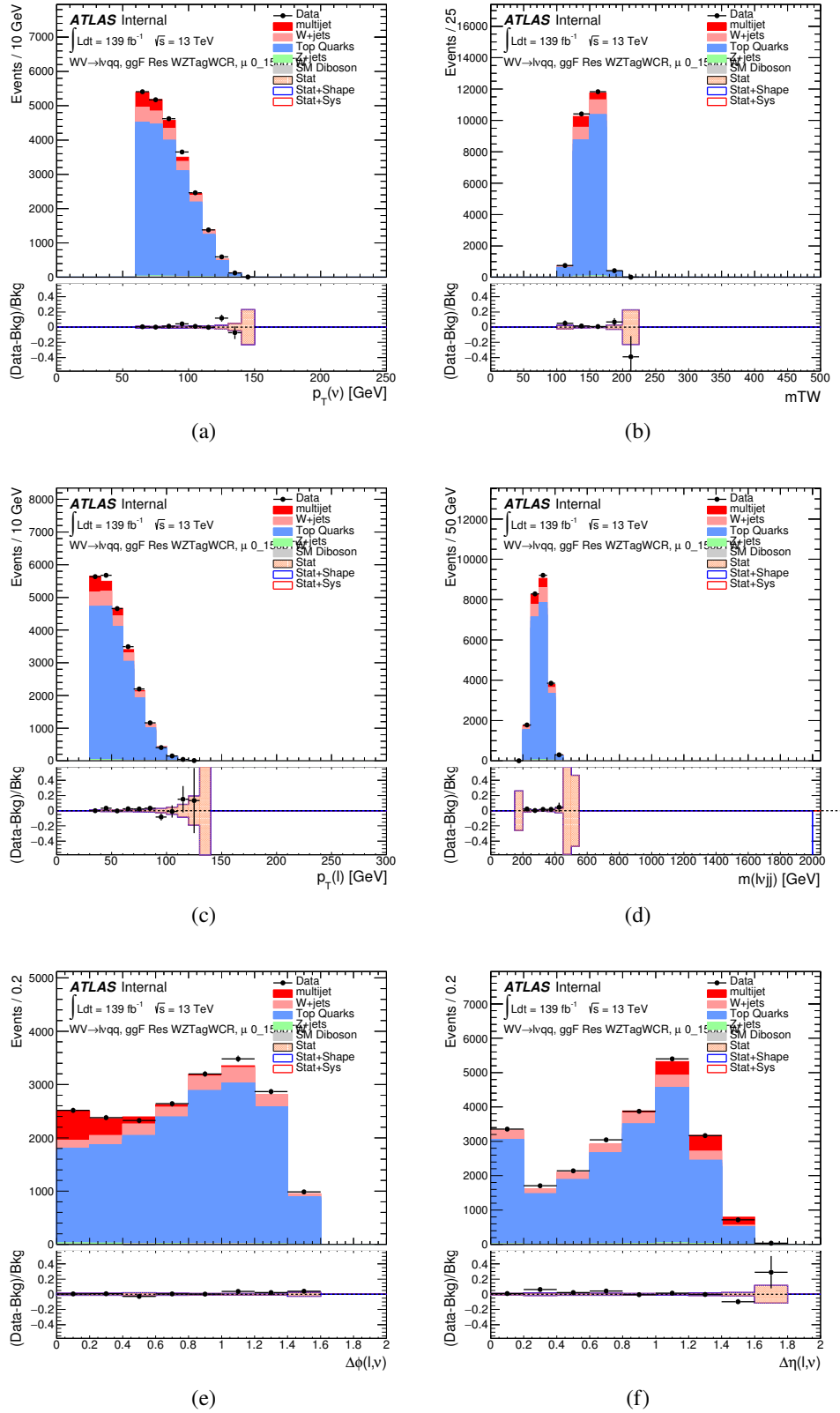


Figure 10.13: Postfit Data/MC comparison of distributions of E_T^{miss} , m_T^W , lepton and neutrino p_T , $m_{\ell\nu jj}$, lepton- ν angular distance in the WZ untag muon channel. The MJ template is obtained from the pre-MJ-fit.

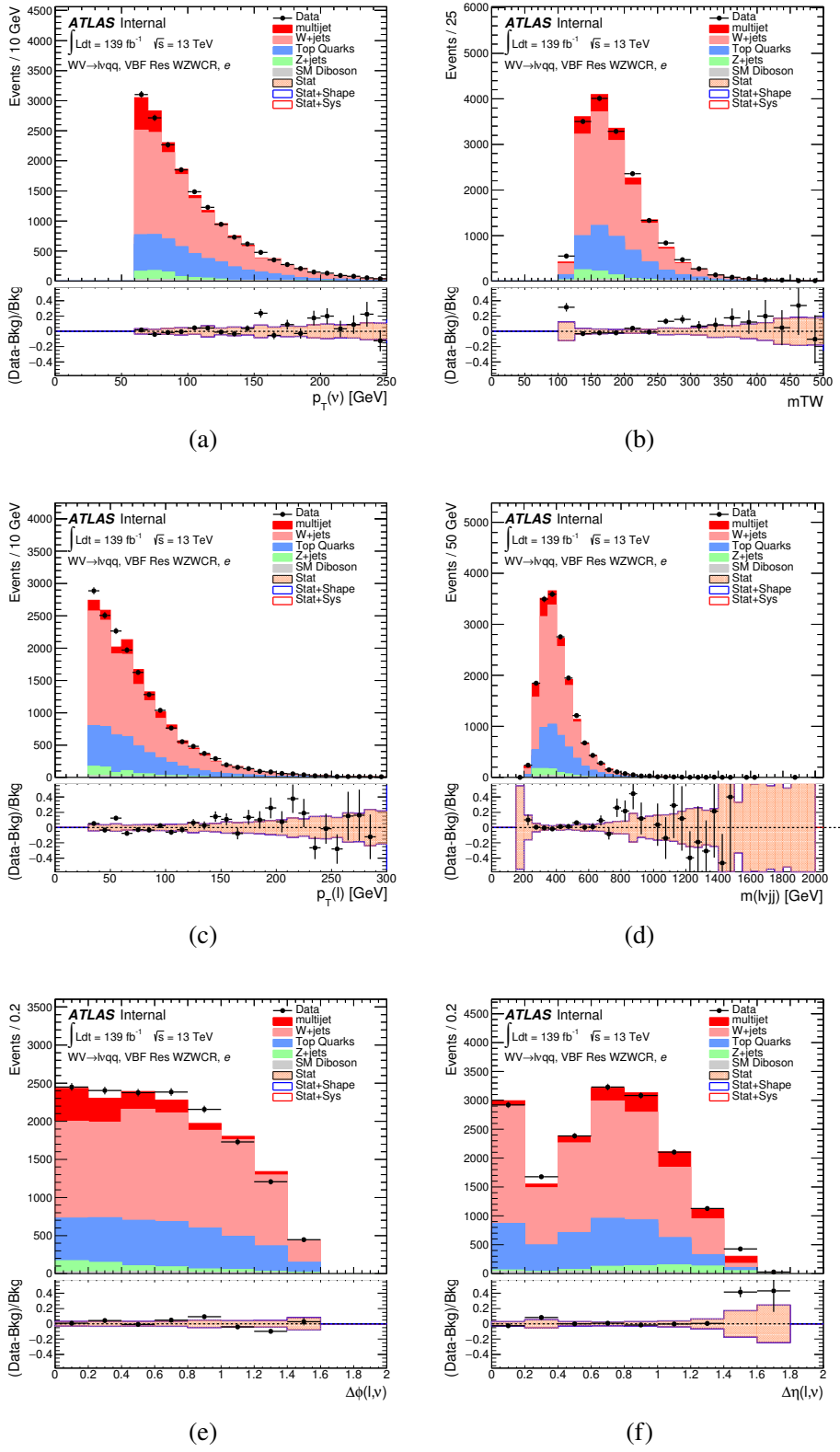


Figure 10.14: Postfit Data/MC comparison of distributions of E_T^{miss} , m_T^W , lepton and neutrino p_T , $m_{l\nu jj}$, lepton- ν angular distance in the VBF WW electron channel. The MJ template is obtained from the pre-MJ-fit.

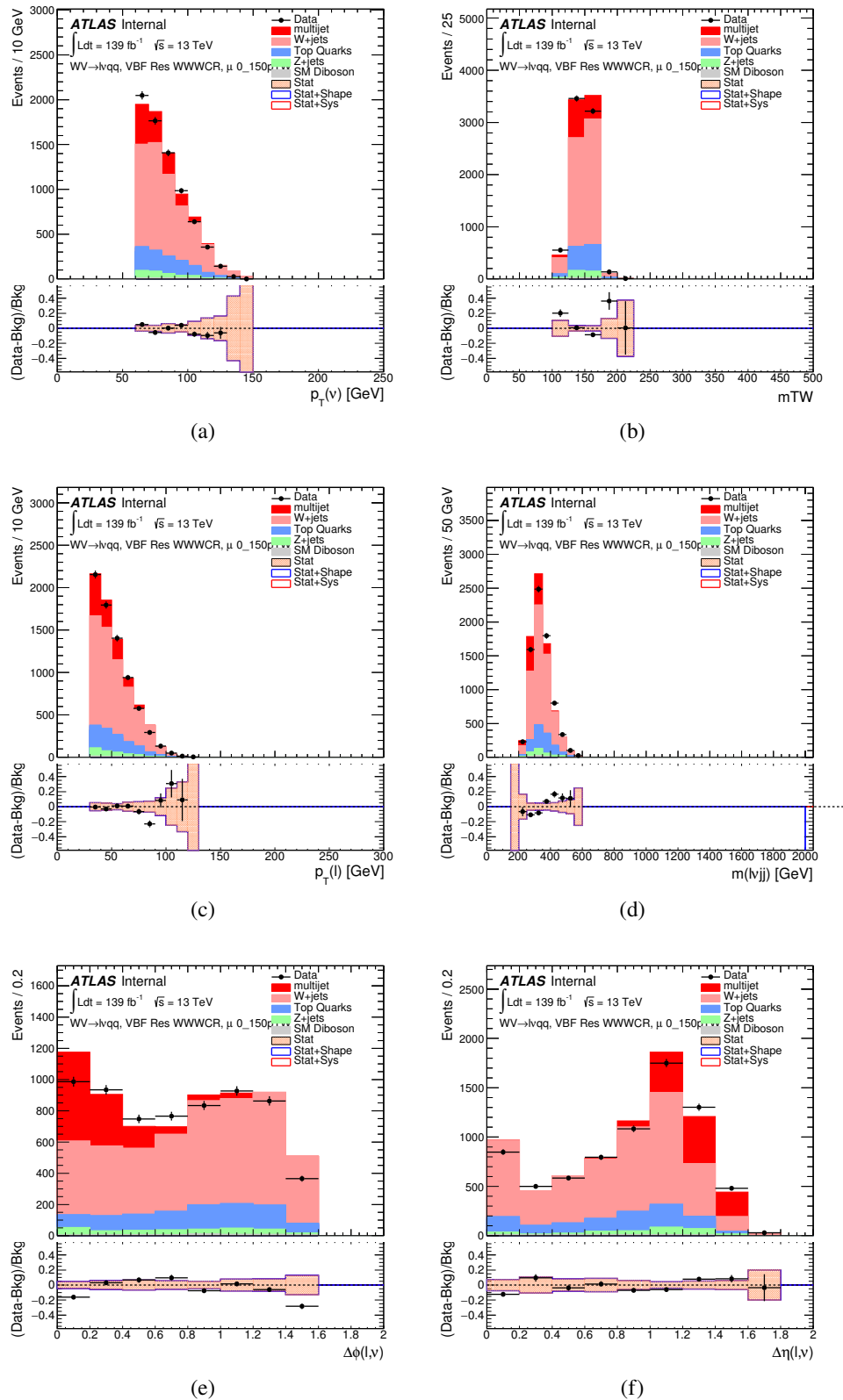


Figure 10.15: Postfit Data/MC comparison of distributions of E_T^{miss} , m_T^W , lepton and neutrino p_T , $m_{\ell\nu jj}$, lepton- ν angular distance in the VBF WW muon channel. The MJ template is obtained from the pre-MJ-fit.

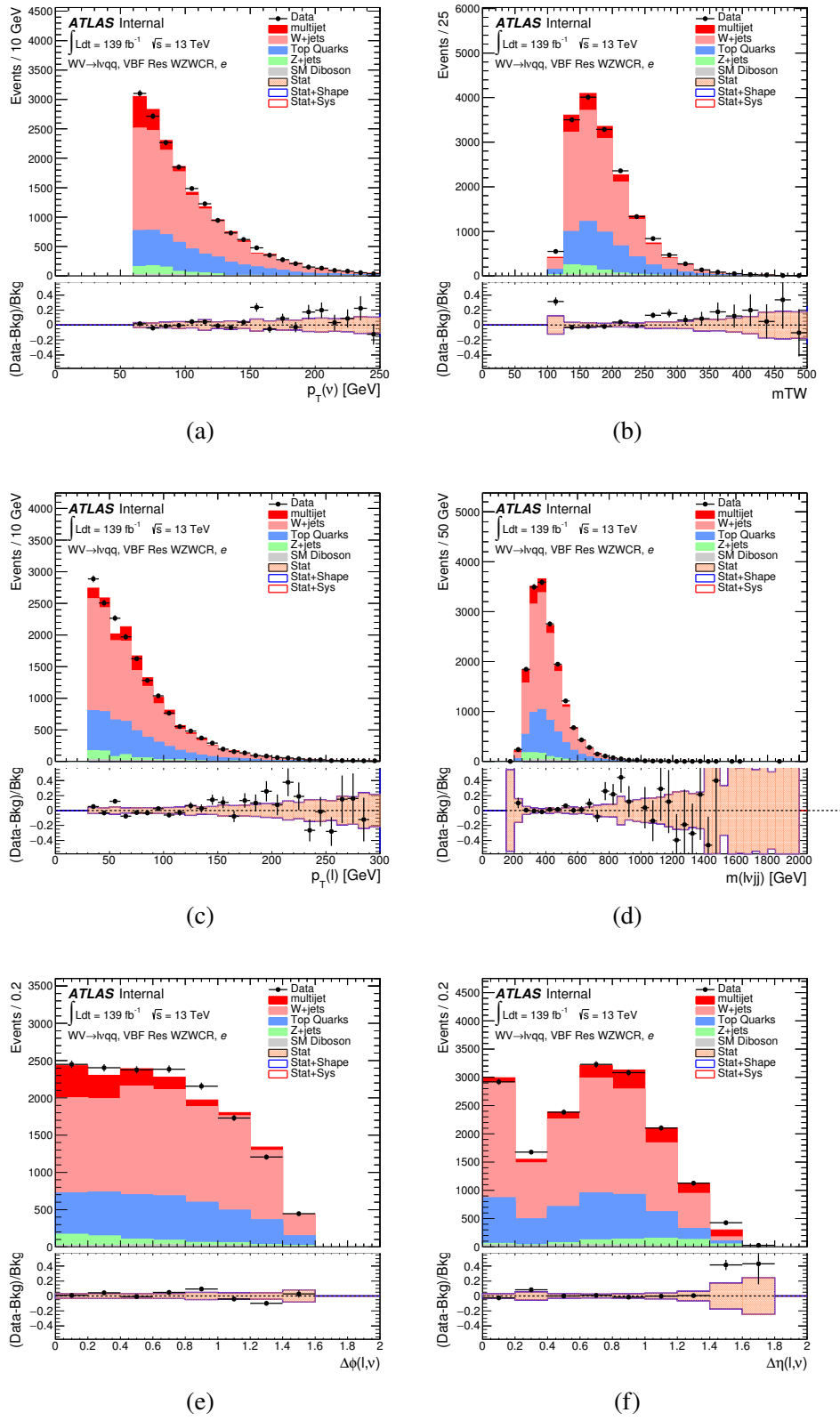


Figure 10.16: Postfit Data/MC comparison of distributions of E_T^{miss} , m_T^W , lepton and neutrino p_T , $m_{l\nu jj}$, lepton- ν angular distance in the VBF WZ electron channel. The MJ template is obtained from the pre-MJ-fit.

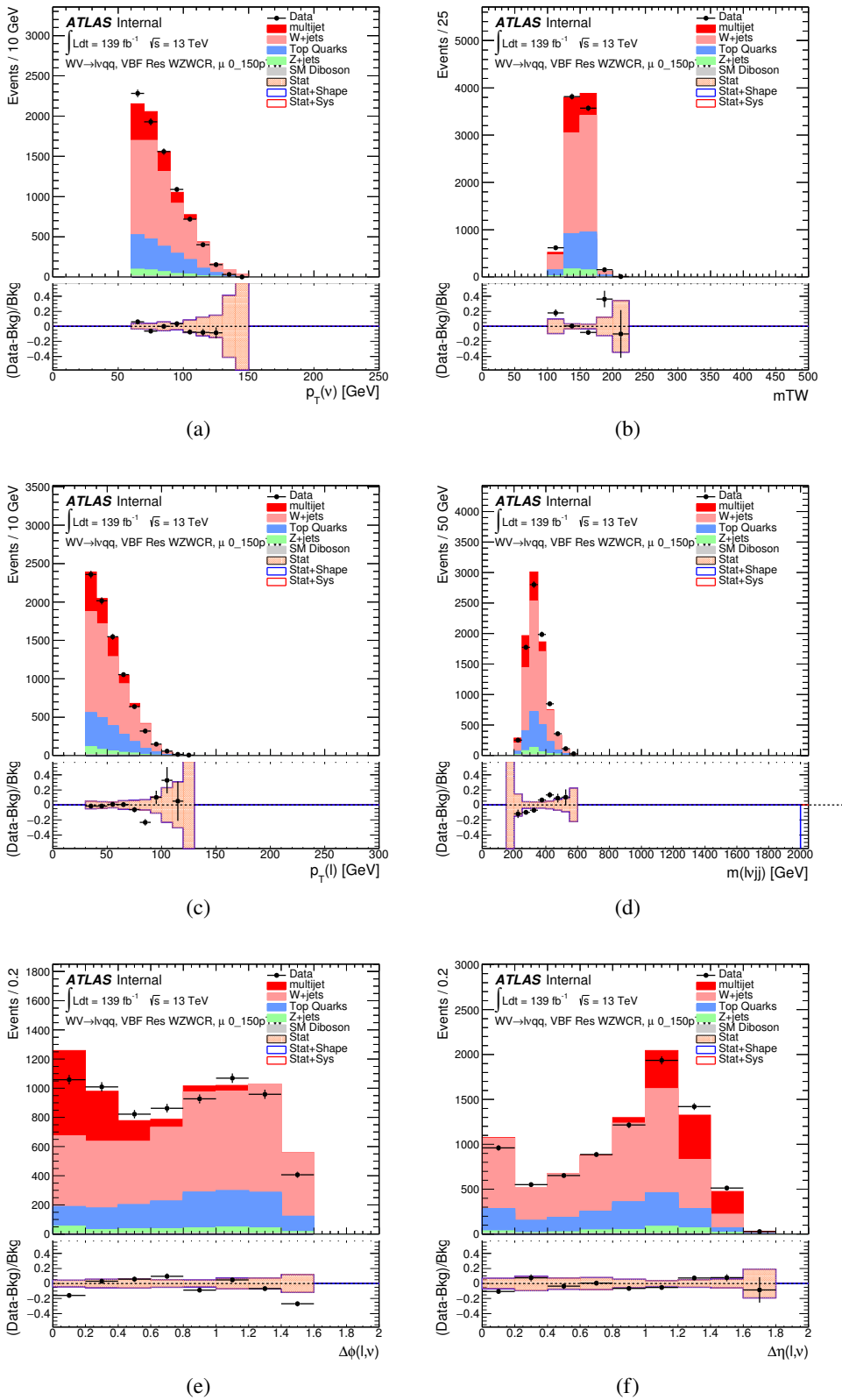


Figure 10.17: Postfit Data/MC comparison of distributions of E_T^{miss} , m_T^W , lepton and neutrino p_T , $m_{\ell\nu jj}$, lepton- ν angular distance in the VBF WZ muon channel. The MJ template is obtained from the pre-MJ-fit.

Full Run 2
ggF Res WWWCR

Sample	Yield	R.U.	SF
Top&W	645040 ± 1971.68	0.31%	0.998
Z&VV	24075.9		fixed
MJ_el	24156.3 ± 1224.62	5.06%	3.973
MJ_mu	35528.5 ± 923.94	2.60%	9.019

ggF Res WZ01bWCR

Sample	Yield	R.U.	SF
Top&W	644690 ± 1981.4	0.31%	0.997
Z&VV	24075.9		fixed
MJ_el	24366.5 ± 1232.69	5.05%	3.874
MJ_mu	35528.5 ± 921.27	2.58%	8.746

ggF Res WZ2bWCR

Sample	Yield	R.U.	SF
Top&W	71236.5 ± 688.74	0.97%	1.031
Z&VV	518.5		fixed
MJ_el	595.63 ± 449.34	75.44%	0.094
MJ_mu	1196.9 ± 222.13	18.56%	0.294

VBF Res WWWCR

Sample	Yield	R.U.	SF
Top&W	19032.3 ± 364.43	1.91%	0.928
Z&VV	1091.63		fixed
MJ_el	1425.73 ± 214.42	15.03%	0.235
MJ_mu	1281.36 ± 157.21	11.83%	0.314

VBF Res WZWCR

Sample	Yield	R.U.	SF
Top&W	21341.8 ± 392.21	1.84%	0.942
Z&VV	1111.75		fixed
MJ_el	1413.76 ± 230.36	16.29%	0.225
MJ_mu	1281.36 ± 157.21	12.27%	0.314

Table 10.2: Fit validation result in WCRs for 2015+16 data. The fit is done in various WCRs, in order to obtain the corresponding scale factors for MJ templates: ggF resolved WCR for the $WW \rightarrow lvqq$ selection, ggF resolved untagged WCR for the $WZ \rightarrow lvqq$ selection, ggF resolved tagged WCR for the $WZ \rightarrow lvqq$ selection, VBF resolved WCR for the $WW \rightarrow lvqq$ selection, and VBF resolved WCR for the $WZ \rightarrow lvqq$ selection. Post-fit event yields for electroweak processes and MJ contributions are shown. The SF column shows the corresponding normalization scale factors for electroweak processes from the fit. R.U. stands for relative uncertainty.

₁₁₃₂ **Chapter 11**

₁₁₃₃ **Systematic Uncertainties**

₁₁₃₄ This section describes the sources of systematic uncertainties of the m_{WV} dis-
₁₁₃₅ tribution. These uncertainties are divided into experimental and modeling un-
₁₁₃₆ certainties. Each systematic uncertainty is treated as a nuisance parameter in
₁₁₃₇ the final likelihood fit. The dominant systematics in this analysis arise from jet
₁₁₃₈ reconstruction and the generator choice for the $V + \text{jets}$ backgrounds.

₁₁₃₉ **11.1 Experimental Systematics**

₁₁₄₀ The uncertainty on the integrated luminosity of the dataset used is 1.7% and
₁₁₄₁ a systematic in the final fit. This uncertainty was calculated using $x - y$ beam
₁₁₄₂ separation scans [natasha ref P55].

₁₁₄₃ Another source of systematic uncertainty is assigned to the pileup modeling in
₁₁₄₄ MC samples. This ensures simulated detector response and particle reconstruction
₁₁₄₅ conditions are as similar as possible. The distribution of the average number of
₁₁₄₆ interactions per bunch crossing applied to simulation is called the μ profile. The
₁₁₄₇ pileup modeling uncertainty is accounted for by re-weighting simulated events so
₁₁₄₈ the average number of interactions per bunch crossing varies within its uncertainty

1149 due to systematics from vertex reconstruction [cite ATL-COM-SOFT-2015-119].

1150 The associated re-weighting factors are propagated through the entire analysis
1151 chain to construct a systematic uncertainty on m_{VV} .

1152 The single-lepton and E_T^{miss} triggers used are not fully efficient, so scale factors
1153 are applied to simulation to more accurately model the data. These scale factors
1154 are given by the ratio of the distribution of offline objects before trigger selection
1155 and after trigger selection. The associated uncertainty on these scale factors are
1156 used in the final fit.

1157 Uncertainties on small-R jet energy scale and resolution are measured in-situ
1158 by calculating the response between data and simulation. This analysis uses a
1159 reduced set of JES and JER uncertainties (totaling 30 and 8 systematics, respec-
1160 tively). This reduced set of systematics is calculated using a principal component
1161 analysis, yielding largely uncorrelated independent systematics. These uncertain-
1162 ties on jet energy scale and resolution (JES and JER, respectively) account for the
1163 dependence on p_T , η , μ , flavor response and global sequential corrections. System-
1164 atic uncertainties associated with b -tagging are also considered. These systematics
1165 are evaluated as uncertainties on a scale factor which accounts for the difference
1166 in b -tagging efficiencies in data and MC, and the flavor dependence (between b,
1167 c, and light jets).

1168 The uncertainty on the p_T scale of the large-R jets is determined by comparing
1169 the jet's p_T^{calo} to p_T^{track} in di-jet simulation and data. In addition to this uncertain-
1170 ties from tracking, modeling (Pythia vs Herwig), and statistical constraints are
1171 also calculated. The large-R jet p_T resolution is given by smearing the jet p_T with
1172 a Gaussian with a 2% width.

1173 The W/Z tagging efficiency scale factor is estimated by comparing the tagging
1174 efficiency in simulation with that in data for four regions of the W/Z tagger (D_2

fail, m_J fail; D_2 pass, m_J fail; D_2 fail, m_J pass; D_2 pass, m_J pass). (Additionally, separate scale factors are determined for events with large-R jets from W bosons and top backgrounds.) A simultaneous template fit is used to fit the signal jets (jets initiated by W/Z bosons or top quarks) and background jets (all other jets from the simulated backgrounds) to the data in the four regions using the m_J distributions. The scale factor for a given region is then given by:

$$SF = \frac{\epsilon_{data}^{region}}{\epsilon_{MC}^{region}} = \frac{\frac{N_{fitted-signal}^{region}}{N_{all-regions}^{fitted-signal}}}{\frac{N_{signal}^{region}}{N_{all-regions}^{signal}}} \quad (11.1)$$

The effects of experimental and theoretical uncertainties on the efficiency scale factor are determined by taking the ratio of efficiencies in data and simulation. By taking this ratio the uncertainties not arising for jet mass and D_2 cancel.

Lepton identification, reconstruction, isolation systematic uncertainties are determined by reconstructing the Z mass peak with a tag and probe method. The lepton energy and momentum scales are also measured with the Z mass peak.

As E_T^{miss} is calculated using all the physics objects in the event, all those objects associated errors result in an uncertainty on E_T^{miss} . Additionally, the unassociated tracks used to construct E_T^{miss} contribute to the uncertainty on E_T^{miss} .

11.2 Theory Systematics

Theoretical uncertainties for signal and background processes arise from uncertainties in the parameters used in Monte Carlo simulation. In particular for the $t\bar{t}$, $W/Z+jets$, diboson backgrounds and signal samples, the QCD scale, PDF, generator and hadronization uncertainties were evaluated. To assess the QCD scale uncertainty the renormalization and factorization scales were scaled up and

1196 down by a factor of two at the event generation stage of sample production. Un-
1197 certainties due to the choice of the parton distribution functions were evaluated by
1198 re-weighting samples from the nominal PDF to a set of error PDFs which account
1199 for the uncertainty of the fits used to produce the PDF set. In addition to this,
1200 samples are re-weighted to different PDF sets to account for the arbitrariness of
1201 the PDF choice. The difference between the m_{WV} distributions using different
1202 event generators is assessed by comparing samples generated with different gen-
1203 erators. Similarly, the uncertainty in hadronization models is accounted for by
1204 comparing samples created using different hadronization models (e.g. $t\bar{t}$ Powheg
1205 is compared to AMC@NLO, $W + jets$ compares Sherpa and MadGraph+Pythia
1206 samples). Figures 11.1 - 11.8 show the impact of these uncertainties on the $t\bar{t}$ and
1207 $W/Z + jets$ backgrounds. Additionally, contributions to the diboson background
1208 for the VBF analysis were found to be small and were accounted for by including
1209 a 5(10)% systematic in the diboson normalization in the final fit.

1210 The normalization of the $t\bar{t}$ and $W+jets$ processes impact the multijet tem-
1211 plate shape. The impact of these normalizations was assessed by including a shape
1212 systematic on the multijet background from varying the $t\bar{t}$ and $W+jets$ normal-
1213 ization factors. The overall normalization of the template is systematic in the
1214 final likelihood fit (account for other systematic effects on the template).

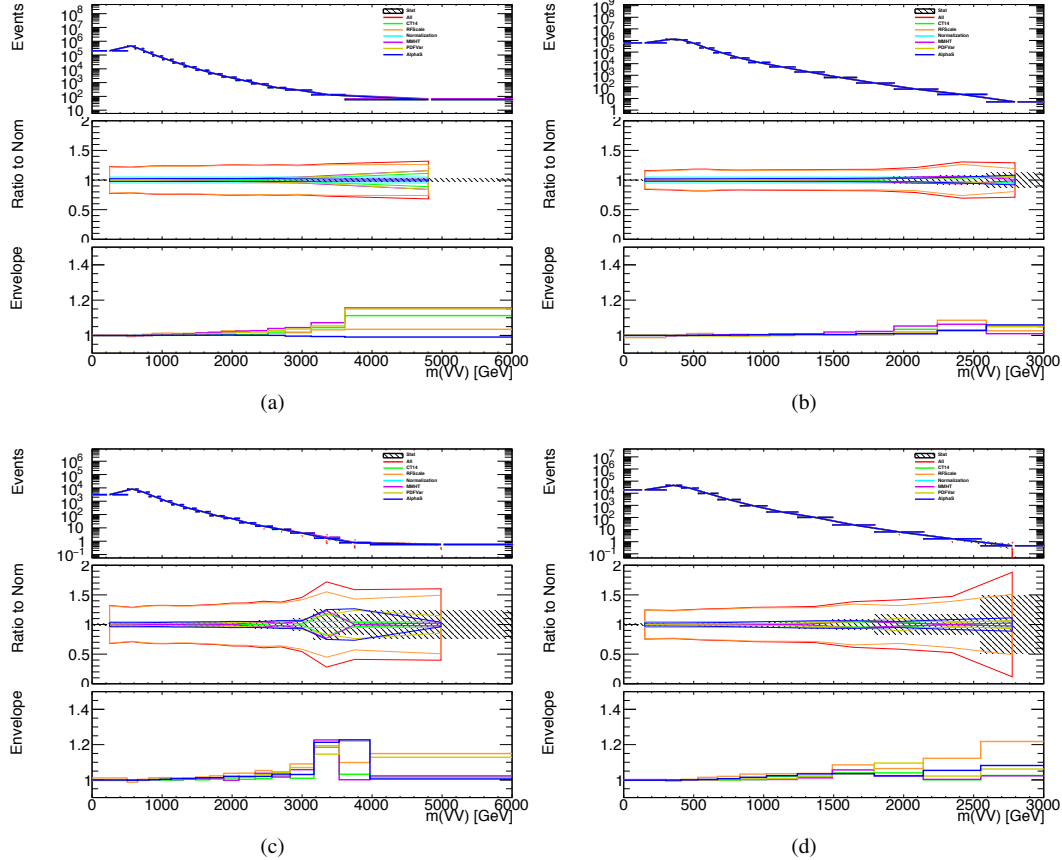


Figure 11.1: The $W/Z + \text{jet}$ systematics for the a) Merged ggF, b) Resolved ggF, c) Merged VBF, and d) Resolved VBF regions. The top subplot shows the nominal and variation distributions/bands, the middle shows the ratio of the two, and the final shows just the shape of the envelope (the final uncertainty).

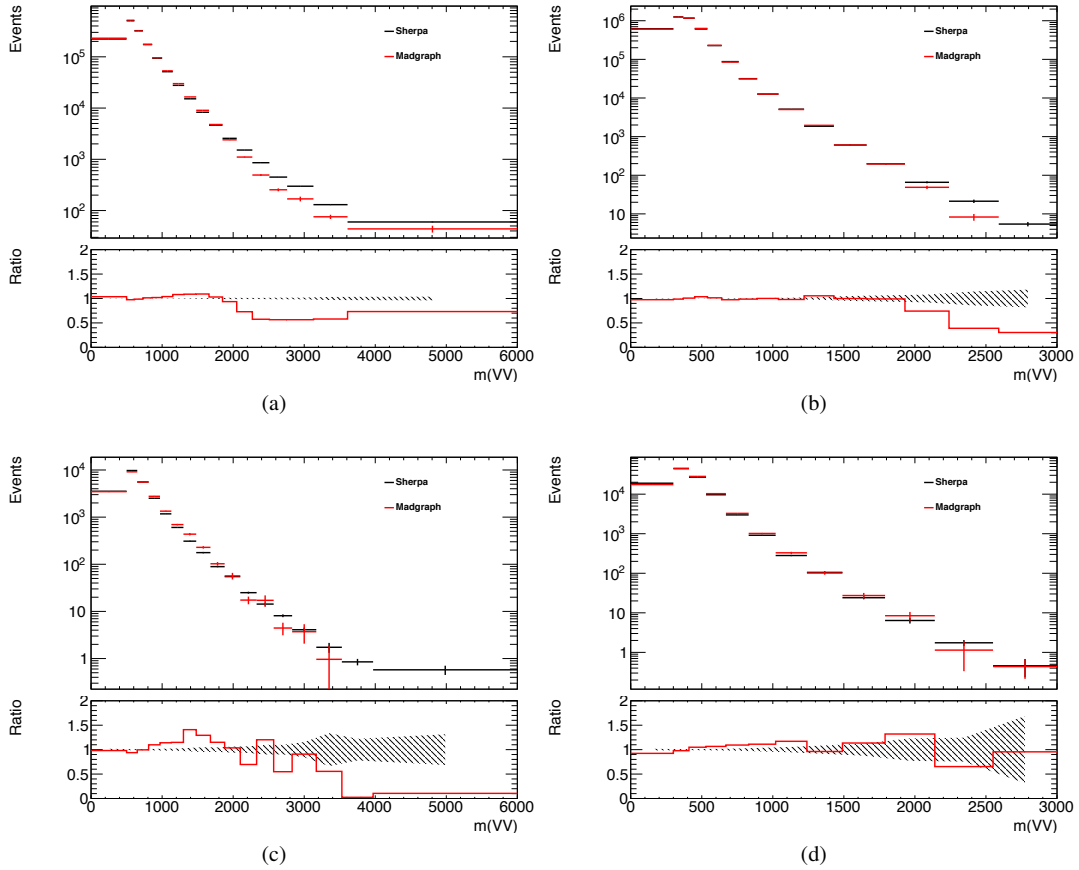


Figure 11.2: The two-point generator comparison between Sherpa and MadGraph for the $W/Z + \text{jet}$ samples in the a) Merged ggF, b) Resolved ggF, c) Merged VBF, and d) Resolved VBF regions. The normalization of the Madgraph sample is set to the Sherpa value to consider only shape effects. The bottom inset shows the ratio of the two.

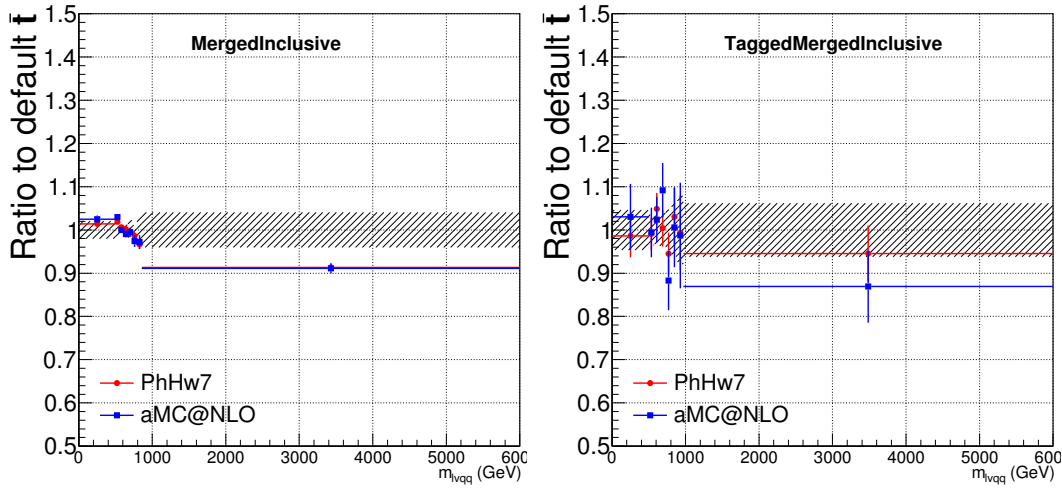


Figure 11.3: Ratio between the variations of generator (red) and hadronization (blue) variations for the Merged regime for $t\bar{t}$ sample.

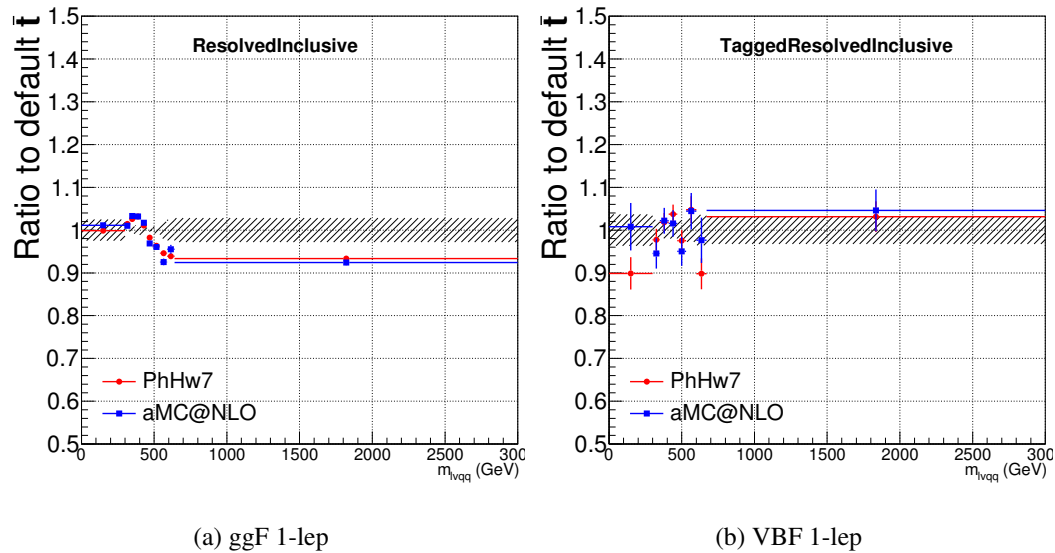


Figure 11.4: Ratio between the variations of generator (red) and hadronization (blue) variations for the Resolved regime for $t\bar{t}$ sample.

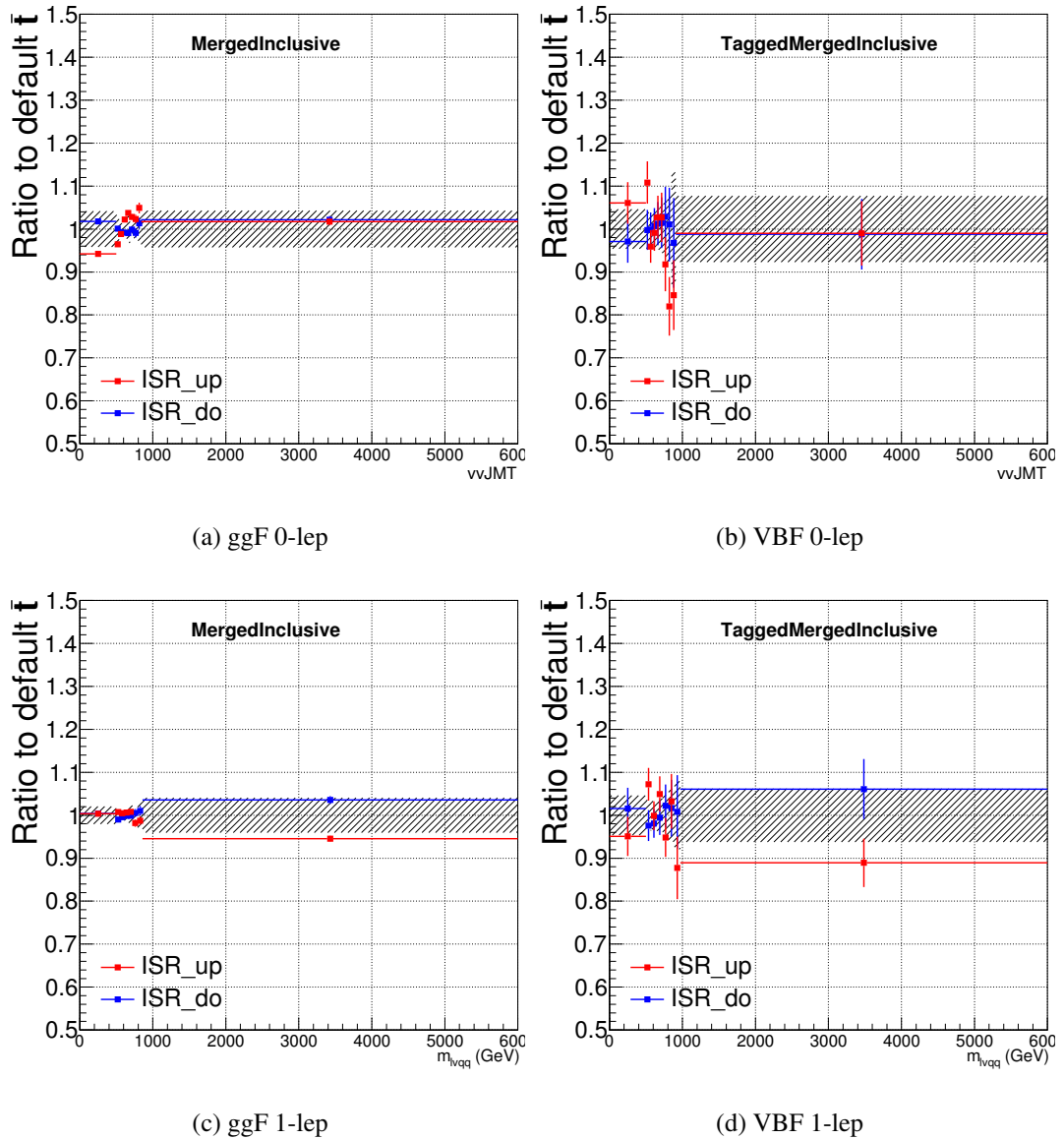


Figure 11.5: Ratio between the variations of ISR up (red) and down (blue) variations for the Merged regime for $t\bar{t}$ sample.

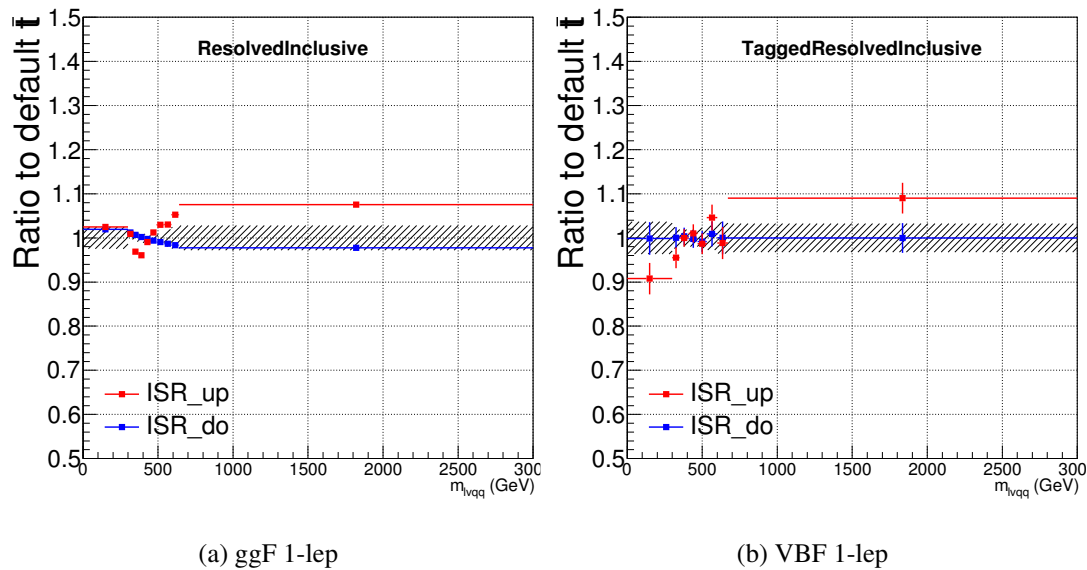


Figure 11.6: Ratio between the variations of ISR up (red) and down (blue) variations for the Resolved regime for $t\bar{t}$ sample.

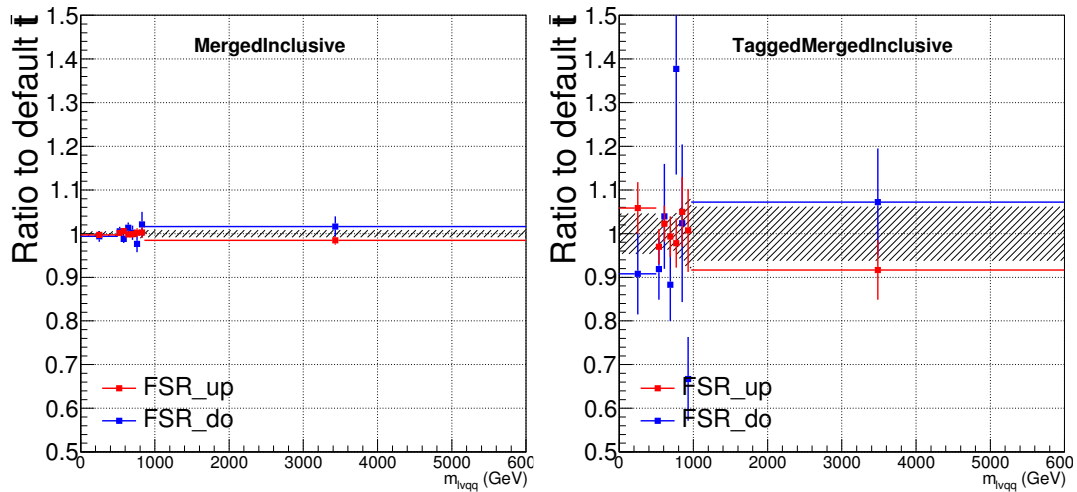


Figure 11.7: Ratio between the variations of FSR up (red) and down (blue) variations for the Merged regime for $t\bar{t}$ sample.

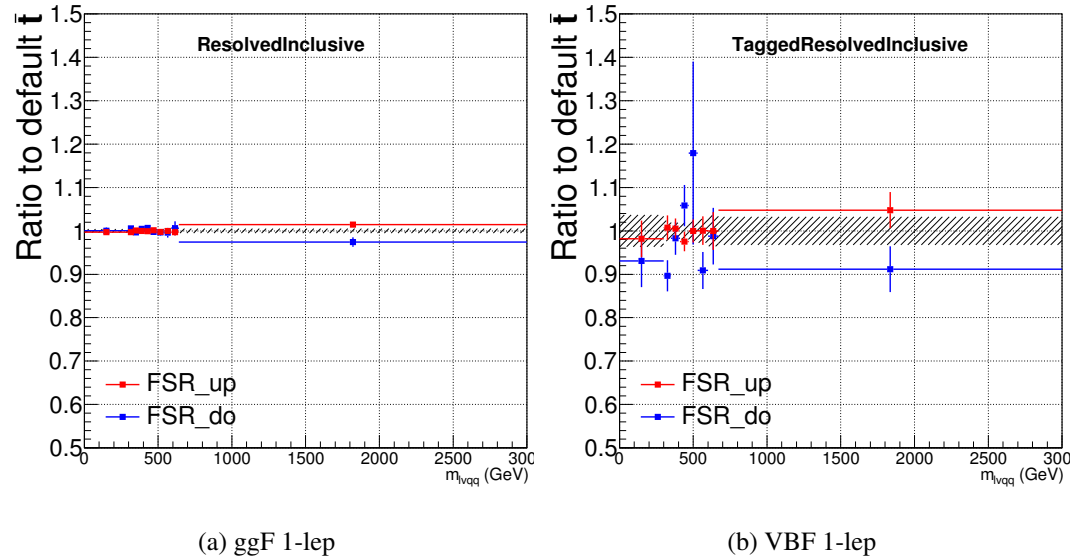


Figure 11.8: Ratio between the variations of FSR up (red) and down (blue) variations for the Resolved regime for $t\bar{t}$ sample.

₁₂₁₅ **Chapter 12**

₁₂₁₆ **Statistical Analysis**

₁₂₁₇ To determine the compatibility of the data collected with the proposed reso-
₁₂₁₈ nances a statistical procedure based on a likelihood function is used. This test
₁₂₁₉ compares the distribution of m_{WV} for the background only hypothesis with the
₁₂₂₀ background and signal hypothesis (see Figures 13.5 - 13.9 for m_{WV} SR distribu-
₁₂₂₁ tions). A discovery test is used to measure the compatibility of the observed data
₁₂₂₂ with the background only hypothesis. If the observed data are sufficiently incom-
₁₂₂₃ patible with the background only hypothesis, this could indicate a discovery. In
₁₂₂₄ the absence of discovery, upper limits on the signal strength parameter, μ , are as-
₁₂₂₅ sessed using the CLs method. For signal masses below 500GeV only the resolved
₁₂₂₆ analysis is used, as the merged analysis is not applicable for such small resonance
₁₂₂₇ masses. Similarly, it is unlikely that the two jets from the hadronically decaying
₁₂₂₈ boson will be well separated for signal masses exceeding 1 TeV. Therefore, only
₁₂₂₉ the merged analysis is used above 1TeV. For signal masses between 500 - 1000
₁₂₃₀ GeV the merged and resolved analyses are combined for the signal production
₁₂₃₁ mode considered.

1232 12.1 Likelihood Function Definition

1233 The likelihood function is product of Poisson probabilities over all m_{WV} bins
1234 and the associated systematics:

$$\mathcal{L}(\mu, \boldsymbol{\theta}) = \prod_c \prod_i \frac{(\mu s_{ci}(\boldsymbol{\theta}) + b_{ci}(\boldsymbol{\theta}))^{n_{ci}}}{n_{ci}!} e^{-(\mu s_{ci}(\boldsymbol{\theta}) + b_{ci}(\boldsymbol{\theta}))} \prod_k (\theta'_k | \theta_k) \quad (12.1)$$

1235 Here c are the analysis channels (e.g. merged SRs and CRs and resolved SRs
1236 and CRs) considered and i runs over all the m_{WV} bins used in the fit. The
1237 signal strength parameter, μ , multiplies the expected signal yield in each anal-
1238 ysis bin, s_{ci} . The background content for channel c and bin i is given by b_{ci} .
1239 The dependence of signal and background predictions on systematic uncertain-
1240 ties is described by the aforementioned set of nuisance parameters $\boldsymbol{\theta}$, which are
1241 parameterized by Gaussian or log-normal priors denoted here as θ_k . Statistical
1242 uncertainties of the simulated bin contents are also included as systematic un-
1243 certainties. Most systematics are correlated among all the analysis regions and
1244 considered to be independent from each other. The validity of this assumption is
1245 checked by evaluating the covariance of nuisance parameters.

1246 12.2 Fit Configuration

1247 The binning of m_{WV} in signal regions for the likelihood fit is determined by the
1248 statistical uncertainty of signal mass width. For each signal mass point, the signal
1249 mass resolution is given by the fitted Gaussian width in simulate of m_{WV} . The
1250 fitted signal widths are then fit to a line to give a parameterized signal mass width,
1251 as shown in Figures 12.1 and 12.2. Bin widths are set first to this parameterized
1252 signal mass resolution. Then if the statistical uncertainty of the data or simulated

1253 background is more than 50%, bins are merged until the statistical uncertainty is
1254 less than 50%. All control regions contain only a single bin.

1255 For this analysis, each signal model is fit in the Merged and Resolved chan-
1256 nels for the relevant signal production mode simultaneously. The $W + \text{jets}$ and $t\bar{t}$
1257 normalizations are given by the best fit values in the overall fit and these fitted
1258 normalizations are then applied to those backgrounds in the SRs, as mentioned
1259 previously.

1260 The m_{VV} distributions for a given systematic may contain unphysically large
1261 fluctuations due to m_{VV} bins with few events. This can lead to artificial pulls and
1262 constraints in the fit. To remove such issues a multi-step smoothing procedure is
1263 applied to all systematic variation distributions. First, distributions are rebinned
1264 until the statistical error per bin is at least 5%. Next all local extrema are identi-
1265 fied. The bins around smallest extrema are iteratively merged until only four local
1266 extrema remain. Then distributions are rebinned so that statistical uncertainties
1267 in each bin are $< 5\%$.

1268 For some systematics, up and down variations may be in the same direction
1269 with respect to the nominal distributions. This causes the variations to not cover
1270 the nominal choice, and the interpretation of the confidence interval is skewed as
1271 the nominal distribution should be bracketed by the up and down variations. This
1272 asymmetry may also lead to unconstrained systematics in the fit. To handle such
1273 asymmetric systematics, if the up and down variation for a given systematic are in
1274 the same direction for at least three m_{VV} bins the variation is averaged for those
1275 bins. The averaging procedure replaces bin-by-bin the up and down variation bins
1276 by $b_{\pm}^{new} = b_{nom} \pm \frac{|b_+ - b_-|}{2}$, where b_{nom} is the nominal bin content and b_{\pm} are the
1277 original up and down variation bin content. The same procedure is also applied to
1278 any variations where the integral of the difference between the up/down variation

1279 and the nominal distribution is twice that of the other down/up variation, further
 1280 ensuring variations are symmetric around the nominal distribution.

1281 Finally, systematics that have a negligible effect on the m_{WW} distribution are
 1282 not considered in the fit. Shape systematics where no bin in the variational dis-
 1283 tribution deviates more than 1% from the nominal distribution (after normalizing
 1284 all histograms to the nominal) are not included in the fit. Also, statistical bin
 1285 uncertainties < 1% are ignored.

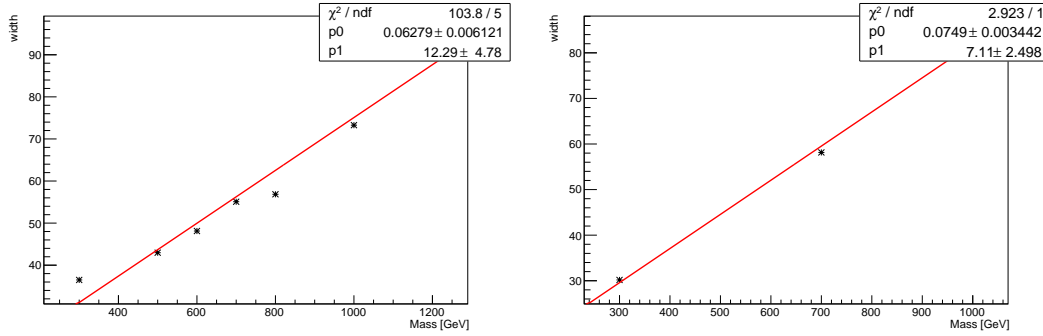


Figure 12.1: The HVT signal mass resolution as a function of mass fit with a straight line in the Resolved ggF region (left) and VBF (right) region.

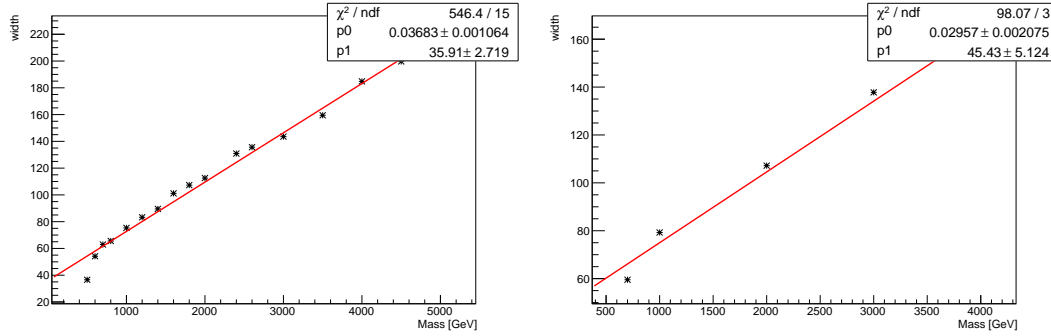


Figure 12.2: The HVT signal mass resolution as a function of mass fit with a straight line in the Merged ggF region (left) and VBF (right) region.

1286 **12.3 Best Fit μ**

1287 The best fit signal strength parameter is denoted by $\hat{\mu}$ and calculated by
1288 maximizing the likelihood function over the entire m_{WV} distribution with respect
1289 to all systematics and μ . The corresponding set of systematics that maximize
1290 the likelihood are given by $\hat{\boldsymbol{\theta}}$. The first term in the likelihood is maximized
1291 when the expected number of signal and background events over all m_{WV} bins is
1292 equal to the number of events in data ($n_{ci} = \mu s_{ci} + b_{ci}$) . Thus, by maximizing
1293 the likelihood, the fit determines value of μ and $\boldsymbol{\theta}$ that give the best agreement
1294 between expected and measured event yields. The second term in the likelihood
1295 is a penalty term which decreases the likelihood when systematics are shifted
1296 from their nominal values. This prevents the fit from profiling (unexpectedly)
1297 constraining or shifting the fitted value of a systematic far from its nominal value)
1298 systematics in unphysical ways to maximize the likelihood. The uncertainty on
1299 μ is calculated by varying μ up and down until the natural log of the likelihood
1300 function shifts by one-half.

1301 **12.4 Discovery Test**

1302 To determine if the observed dataset is consistent with tested signal model a
1303 likelihood ratio is constructed:

$$\lambda(\mu) = \frac{\mathcal{L}(\mu, \hat{\boldsymbol{\theta}}_\mu)}{\mathcal{L}(\hat{\mu}, \hat{\boldsymbol{\theta}})} \quad (12.2)$$

1304 The denominator in this equation is the maximized value of \mathcal{L} over all system-
1305 atics and μ . The numerator is the maximized likelihood over all systematics for
1306 a given μ value, where the maximized systematics are given by $\hat{\boldsymbol{\theta}}_\mu$. To test for
1307 the existence of signal the observed dataset the null hypothesis (H_0) is defined as

1308 the background only hypothesis and the alternate hypothesis includes signal and
 1309 background (H_1). This test quantifies the compatibility of observed data with
 1310 H_0 by calculating a p-value representing the probability of observing data as dis-
 1311 crepant or more than the observed data under the H_0 . The test statistic used to
 1312 calculate this p-value is given by (r_0):

$$r_0 = \begin{cases} -2 \ln \lambda(0), \hat{\mu} > 0 \\ +2 \ln \lambda(0), \hat{\mu} < 0 \end{cases} \quad (12.3)$$

1313 The expected distribution of the the test statistic under H_0 ($f(r_0|0)$) is used
 1314 to calculate the p-value:

$$p_0 = \int_{r_0,obs}^{\infty} f(r_0|0) dr_0 \quad (12.4)$$

1315 Small p-values indicate the observed data is poorly described by H_0 . This
 1316 equivalent Z-score of a given p-value is usually used to further quantify the agree-
 1317 ment between the observed data and H_0 . The Z-score is given by the number of
 1318 standard deviations away from the mean of a Gaussian distribution, the integral
 1319 of the upper tail of the distribution would equal the p-value. Mathematically:

$$Z = \Phi^{-1}(1 - p_0) \quad (12.5)$$

1320 where Φ is the Gaussian cumulative distribution function. The statistical
 1321 significance of these tests are expressed as the Z -score. In particle physics, 3σ is
 1322 considered evidence for new phenomena and 5σ is the threshold for discovery.

1323 12.5 Exclusion Limits

1324 In the absence of discovery, upper limits on the signal strength, μ are set using
 1325 the CLs method [cite P60]. The test statistic for this test, q_μ , is constructed as:

$$\tilde{\lambda}_\mu = \begin{cases} \frac{\mathcal{L}(\mu, \hat{\theta}_\mu)}{\mathcal{L}(\hat{\mu}, \hat{\theta})}, \hat{\mu} > 0 \\ \frac{\mathcal{L}(\mu, \hat{\theta}_\mu)}{\mathcal{L}(0, \hat{\theta}_0)}, \hat{\mu} < 0 \end{cases} \quad (12.6)$$

$$\tilde{q}_\mu = \begin{cases} -2 \ln \tilde{\lambda}(\mu), \hat{\mu} < \mu \\ +2 \ln \tilde{\lambda}(\mu), \hat{\mu} > \mu \end{cases} \quad (12.7)$$

1326 As defined, larger values of q_μ correspond to increasing incompatibility between
 1327 the observed data and the background + signal hypothesis. The observed value
 1328 of the test statistic, $q_{\mu, obs}$, is then compared to its expected distribution, f , to
 1329 calculate p-values to assess the likelihood of the background+signal hypothesis.
 1330 Using these distributions, CL_s values are computed as:

$$CL_{s+b} = \int_{q_{\mu, obs}}^{\infty} f(q_\mu | \mu) dq_\mu \quad (12.8)$$

$$CL_b = \int_{q_0^{obs}}^{\infty} f(q_\mu | \mu = 0) dq_\mu \quad (12.9)$$

$$CL_s = \frac{CL_{s+b}}{CL_b} \quad (12.10)$$

1331 CL_{s+b} is the p-value for the signal + background hypothesis and CL_b is the
 1332 p-value for the background only hypothesis. The CL_s value is interpreted as
 1333 the probability to observe the background + signal hypothesis normalized to the
 1334 probability of background-only hypothesis. Normalizing by CL_b prevents setting
 1335 artificially strong exclusion limits due to downward fluctuations in data.

1336 For a given signal hypothesis, μ values are scanned simultaneously over all
 1337

₁₃₃₉ m_{WV} bins to find the μ value that yields $CL_s=0.05$, meaning the likelihood of
₁₃₄₀ finding data more incompatible with the signal+background hypothesis (relative
₁₃₄₁ to the background only hypothesis) is 5%. The 95% upper limit on the cross
₁₃₄₂ section is then calculated as the product of the μ value found, branching ratio,
₁₃₄₃ and theory cross section.

1344 **Chapter 13**

1345 **Results**

1346 **13.1 Expected and Measured Yields**

1347 The yield tables for the four analysis regions are shown in Tables ?? - ??.

1348 The fitted background normalizations are shown in Tables ??-??. The control

1349 region $m_{\ell\nu qq}$ distributions are shown in Figures 13.1 - 13.4. The signal region

1350 $m_{\ell\nu qq}$ distributions are shown in Figures 13.5 - ??.

	HP WCR	LP WCR	Resolved WCR
Electron Multi-jet	-	-	16507.83 ± 2314.87
Muon Multi-jet	-	-	19977.12 ± 2816.06
Diboson	1833.41 ± 177.78	3323.93 ± 320.92	9147.67 ± 961.63
Single-top	2160.62 ± 402.34	3551.09 ± 660.00	20058.36 ± 3817.26
$t\bar{t}$	15518.86 ± 338.22	24069.54 ± 453.15	138866.23 ± 1989.71
$W+jets$	40141.57 ± 357.79	88113.06 ± 487.87	673200.38 ± 4120.53
$Z+jets$	778.83 ± 78.93	1765.54 ± 179.10	16570.50 ± 1672.71
Total	60433.29 ± 664.92	120823.16 ± 1006.99	894328.12 ± 7247.12
Data	60264.00	120852.00	895362.00
	HP TCR	LP TCR	Resolved TCR
Electron Multi-jet	-	-	-
Muon Multi-jet	-	-	-
Diboson	421.11 ± 37.98	550.44 ± 53.10	996.87 ± 119.63
Single-top	4691.44 ± 846.11	3466.26 ± 631.03	16848.71 ± 3258.26
$t\bar{t}$	38945.18 ± 848.77	33836.95 ± 637.04	224226.14 ± 3212.76
$W+jets$	2258.34 ± 20.13	6564.78 ± 36.35	23466.41 ± 143.63
$Z+jets$	66.35 ± 6.72	213.26 ± 21.63	846.66 ± 85.47
Total	46382.43 ± 1199.25	44631.70 ± 899.23	266384.78 ± 4580.43
Data	46354.00	44629.00	266443.00
	WW SR	LP SR	Resolved 1-lepton SR
Electron Multi-jet	-	-	10788.40 ± 1512.85
Muon Multi-jet	-	-	15759.50 ± 2221.53
Diboson	4990.30 ± 376.50	3901.07 ± 313.22	16971.29 ± 1523.77
Single-top	3117.71 ± 565.07	2176.46 ± 400.52	20422.85 ± 3731.94
$t\bar{t}$	13785.77 ± 302.14	11005.12 ± 207.41	126965.25 ± 1819.66
$W+jets$	24718.56 ± 223.72	60080.66 ± 333.12	444133.56 ± 2719.02
$Z+jets$	478.18 ± 48.46	1226.69 ± 124.44	11686.32 ± 1179.69
Total	47090.52 ± 777.65	78389.98 ± 654.22	646727.19 ± 5963.98
Data	47330.00	78380.00	645610.00

Table 13.1: Expected and Measured for DY WW $W+jets$, $t\bar{t}$ control regions and signal regions.

	HP Untagged WCR	LP Untagged WCR	Resolved Untagged WCR
Electron Multi-jet	-	-	15080.03 ± 2277.99
Muon Multi-jet	-	-	27347.10 ± 2950.07
Diboson	1508.48 ± 154.20	2758.24 ± 284.50	9038.55 ± 728.69
Single-top	1756.59 ± 306.69	2913.18 ± 515.93	20511.74 ± 3523.47
$t\bar{t}$	13134.00 ± 238.30	21815.37 ± 334.98	140157.77 ± 2636.96
$W+jets$	40654.84 ± 333.65	87657.76 ± 501.96	665909.12 ± 4420.62
$Z+jets$	768.72 ± 77.97	1759.87 ± 178.96	16512.46 ± 1673.23
Total	57822.63 ± 540.40	116904.42 ± 862.16	894556.75 ± 7492.20
Data	57699.00	117306.00	895362.00
	HP Tagged WCR	LP Tagged WCR	Resolved Tagged WCR
Electron Multi-jet	-	-	384.58 ± 57.11
Muon Multi-jet	-	-	602.93 ± 190.12
Diboson	30.22 ± 4.69	48.95 ± 7.16	264.64 ± 28.24
Single-top	308.44 ± 56.19	371.59 ± 69.43	5752.39 ± 1029.97
$t\bar{t}$	1683.82 ± 48.73	2041.48 ± 70.00	58431.49 ± 614.30
$W+jets$	583.55 ± 75.37	1109.45 ± 85.78	11891.68 ± 903.01
$Z+jets$	13.19 ± 1.34	23.06 ± 2.34	324.74 ± 32.85
Total	2619.22 ± 106.00	3594.53 ± 130.90	77652.45 ± 1514.89
Data	2565.00	3546.00	77973.00
	HP Untagged TCR	LP Untagged TCR	Resolved Untagged TCR
Electron Multi-jet	-	-	-
Muon Multi-jet	-	-	-
Diboson	289.45 ± 28.45	346.78 ± 35.85	650.85 ± 65.56
Single-top	3107.99 ± 538.03	2250.64 ± 385.41	9606.87 ± 1698.22
$t\bar{t}$	30992.40 ± 562.33	26954.21 ± 413.89	91893.59 ± 1728.91
$W+jets$	2236.29 ± 18.35	4874.03 ± 27.91	16122.97 ± 107.03
$Z+jets$	71.54 ± 7.26	155.50 ± 15.81	577.71 ± 58.54
Total	36697.66 ± 779.03	34581.16 ± 567.59	118851.98 ± 2427.40
Data	36677.00	34573.00	118928.00
	HP Tagged TCR	LP Tagged TCR	Resolved Tagged TCR
Electron Multi-jet	-	-	-
Muon Multi-jet	-	-	-
Diboson	9.72 ± 1.13	8.75 ± 1.16	34.06 ± 4.98
Single-top	105.87 ± 20.65	119.66 ± 22.68	656.89 ± 132.96
$t\bar{t}$	1904.75 ± 50.61	1483.86 ± 47.05	17965.33 ± 188.87
$W+jets$	32.36 ± 4.28	85.74 ± 6.96	489.01 ± 37.13
$Z+jets$	1.27 ± 0.13	1.93 ± 0.20	19.14 ± 1.94
Total	2053.98 ± 54.84	1699.93 ± 52.70	19164.43 ± 234.01
Data	2047.00	1708.00	19143.00

Table 13.2: Expected and Measured for DY WZ $W+jets$, $t\bar{t}$ tag and untag control regions.

	HP Untagged SR	LP Untagged SR	Resolved Untagged SR
Electron Multi-jet	-	-	7782.17 ± 1175.56
Muon Multi-jet	-	-	17004.81 ± 1834.40
Diboson	3041.17 ± 273.77	2266.35 ± 212.79	14724.12 ± 1224.31
Single-top	2123.28 ± 373.83	1379.35 ± 240.92	18336.88 ± 3082.47
$t\bar{t}$	11678.86 ± 213.63	8906.34 ± 136.88	112669.24 ± 2122.46
$W+jets$	22741.32 ± 191.47	41726.76 ± 240.56	342934.00 ± 2280.21
$Z+jets$	442.03 ± 44.84	849.79 ± 86.42	9271.83 ± 939.52
Total	40026.65 ± 546.81	55128.59 ± 432.90	522723.03 ± 5131.71
Data	40193.00	54735.00	521813.00
	HP Tagged SR	LP Tagged SR	Resolved Tagged SR
Electron Multi-jet	-	-	199.22 ± 29.58
Muon Multi-jet	-	-	393.43 ± 124.06
Diboson	102.58 ± 11.59	65.44 ± 8.05	624.07 ± 58.10
Single-top	178.21 ± 33.62	155.53 ± 28.95	3470.39 ± 617.48
$t\bar{t}$	1017.93 ± 31.95	706.76 ± 26.20	38189.30 ± 401.91
$W+jets$	325.58 ± 41.62	575.36 ± 43.29	6161.96 ± 467.71
$Z+jets$	7.81 ± 0.80	11.62 ± 1.19	183.36 ± 18.55
Total	1632.11 ± 63.39	1514.70 ± 58.86	49221.74 ± 884.06
Data	1699.00	1559.00	48919.00

Table 13.3: Expected and Measured for DY WZ $W+jets$, $t\bar{t}$ tag and untag signal regions.

	HP WCR	LP WCR	Resolved WCR
Electron Multi-jet	-	-	898.48 ± 137.82
Muon Multi-jet	-	-	601.46 ± 182.74
Diboson	107.45 ± 45.20	166.87 ± 68.11	292.10 ± 235.29
Single-top	78.19 ± 18.22	132.71 ± 31.93	879.82 ± 216.89
$t\bar{t}$	400.71 ± 28.35	569.70 ± 48.88	5067.51 ± 155.69
$W+jets$	864.49 ± 63.44	1940.80 ± 89.41	18563.70 ± 408.99
$Z+jets$	19.51 ± 2.00	46.63 ± 4.77	795.20 ± 80.89
Total	1470.35 ± 84.89	2856.71 ± 126.74	27098.28 ± 594.01
Data	1495.00	2898.00	27120.00
	HP TCR	LP TCR	Resolved TCR
Electron Multi-jet	-	-	-
Muon Multi-jet	-	-	-
Diboson	14.95 ± 6.61	27.57 ± 14.12	24.33 ± 20.32
Single-top	68.31 ± 16.17	58.93 ± 13.56	278.60 ± 73.04
$t\bar{t}$	496.60 ± 31.72	401.23 ± 32.13	3834.49 ± 104.60
$W+jets$	50.68 ± 4.19	144.02 ± 7.86	450.01 ± 11.87
$Z+jets$	1.32 ± 0.14	5.35 ± 0.55	29.96 ± 3.07
Total	631.87 ± 36.45	637.10 ± 38.44	4617.39 ± 129.77
Data	636.00	634.00	4615.00
	HP SR	LP SR	Resolved SR
Electron Multi-jet	-	-	596.34 ± 91.52
Muon Multi-jet	-	-	481.01 ± 144.48
Diboson	148.84 ± 48.64	181.42 ± 67.30	395.52 ± 318.06
Single-top	79.49 ± 19.80	56.82 ± 14.89	782.07 ± 190.79
$t\bar{t}$	338.42 ± 24.14	236.80 ± 20.88	4261.70 ± 138.98
$W+jets$	501.13 ± 39.36	1347.76 ± 64.50	11445.73 ± 291.49
$Z+jets$	9.25 ± 0.95	28.77 ± 2.95	567.66 ± 57.94
Total	1077.13 ± 69.93	1851.57 ± 96.73	18530.03 ± 523.88
Data	1096.00	1846.00	18530.00

Table 13.4: Expected and Measured for VBF WW $W+jets$, $t\bar{t}$ control regions and signal regions.

	HP WCR	LP WCR	Resolved WCR
Electron Multi-jet	-	-	870.00 ± 132.75
Muon Multi-jet	-	-	618.45 ± 196.90
Diboson	92.92 ± 41.77	145.90 ± 64.26	228.62 ± 114.62
Single-top	71.13 ± 16.29	118.82 ± 27.98	1209.87 ± 281.64
$t\bar{t}$	427.80 ± 29.72	509.19 ± 46.57	6860.87 ± 254.83
$W+jets$	871.68 ± 64.22	2020.67 ± 93.54	19088.50 ± 442.10
$Z+jets$	19.58 ± 2.01	47.39 ± 4.85	800.19 ± 82.02
Total	1483.11 ± 83.79	2841.97 ± 125.92	29676.50 ± 644.96
Data	1495.00	2898.00	29755.00
	HP TCR	LP TCR	Resolved TCR
Electron Multi-jet	-	-	-
Muon Multi-jet	-	-	-
Diboson	10.12 ± 4.51	12.73 ± 6.55	14.23 ± 7.49
Single-top	51.57 ± 12.31	35.07 ± 8.17	169.21 ± 44.54
$t\bar{t}$	470.06 ± 28.97	298.99 ± 25.28	2414.75 ± 75.42
$W+jets$	49.64 ± 4.17	109.69 ± 6.16	378.22 ± 12.05
$Z+jets$	1.28 ± 0.13	4.81 ± 0.50	17.62 ± 1.83
Total	582.67 ± 32.07	461.30 ± 28.05	2994.03 ± 88.75
Data	584.00	459.00	3001.00
	HP SR	LP SR	Resolved SR
Electron Multi-jet	-	-	444.65 ± 67.99
Muon Multi-jet	-	-	397.29 ± 125.59
Diboson	109.66 ± 44.13	112.28 ± 46.45	265.75 ± 139.43
Single-top	63.16 ± 15.20	48.02 ± 11.56	872.16 ± 205.00
$t\bar{t}$	348.95 ± 24.34	190.68 ± 17.75	5134.25 ± 193.57
$W+jets$	467.21 ± 37.12	973.73 ± 47.91	10226.83 ± 254.67
$Z+jets$	8.15 ± 0.84	23.62 ± 2.43	558.48 ± 57.25
Total	997.13 ± 64.42	1348.33 ± 70.06	17899.41 ± 432.98
Data	1018.00	1313.00	17826.00

Table 13.5: Expected and Measured for VBF WZ $W+jets$, $t\bar{t}$ control regions and signal regions.

Background	Fitted Normalization
XS_Top_LP_lvqq_Merg_binned	$0.905^{+0.0166}_{-0.0166}$
XS_Top_Merg	$0.936^{+0.0199}_{-0.0199}$
XS_Top_Res	$0.957^{+0.0134}_{-0.0134}$
XS_Wjets_LP_lvqq_Merg_binned	$0.884^{+0.00489}_{-0.00489}$
XS_Wjets_Merg	$0.931^{+0.00831}_{-0.00831}$
XS_Wjets_Res	$1.03^{+0.00628}_{-0.00628}$

Table 13.6: Fitted background normalizations for $t\bar{t}$ and $W+jets$ backgrounds for the DY WW analysis region.

Background	Fitted Normalization
XS_Top_LP_Tag_lvqq_Merg_binned	$0.973^{+0.0333}_{-0.0333}$
XS_Top_LP_lvqq_Merg_binned	$0.894^{+0.0135}_{-0.0135}$
XS_Top_Merg	$0.893^{+0.016}_{-0.016}$
XS_Top_Res	$0.965^{+0.0179}_{-0.0179}$
XS_Top_Tag_lvqq_Merg_binned	$0.954^{+0.0276}_{-0.0276}$
XS_Top_Tag_lvqq_Res_binned	$0.999^{+0.0105}_{-0.0105}$
XS_Wjets_LP_Tag_lvqq_Merg_binned	$0.912^{+0.0703}_{-0.0703}$
XS_Wjets_LP_lvqq_Merg_binned	$0.876^{+0.00502}_{-0.00502}$
XS_Wjets_Merg	$0.948^{+0.00779}_{-0.00779}$
XS_Wjets_Res	$1.01^{+0.00673}_{-0.00673}$
XS_Wjets_Tag_lvqq_Merg_binned	$0.906^{+0.117}_{-0.117}$
XS_Wjets_Tag_lvqq_Res_binned	$1.2^{+0.0904}_{-0.0904}$

Table 13.7: Fitted background normalizations for $t\bar{t}$ and $W+jets$ backgrounds for the DY WZ analysis region.

Background	Fitted Normalization
XS_Top_LP_lvqq_Merg_binned	$0.79^{+0.0673}_{-0.0673}$
XS_Top_Merg	$0.888^{+0.061}_{-0.061}$
XS_Top_Res	$1.01^{+0.0311}_{-0.0311}$
XS_Wjets_LP_lvqq_Merg_binned	$0.88^{+0.0423}_{-0.0423}$
XS_Wjets_Merg	$0.881^{+0.0677}_{-0.0677}$
XS_Wjets_Res	$0.932^{+0.0202}_{-0.0202}$

Table 13.8: Fitted background normalizations for $t\bar{t}$ and $W+jets$ backgrounds for the VBF WW analysis region.

Background	Fitted Normalization
XS_Top_LP_lvqq_Merg_binned	$0.708^{+0.064}_{-0.064}$
XS_Top_Merg	$0.958^{+0.0644}_{-0.0644}$
XS_Top_Res	$1.02^{+0.038}_{-0.038}$
XS_Wjets_LP_lvqq_Merg_binned	$0.9^{+0.0438}_{-0.0438}$
XS_Wjets_Merg	$0.883^{+0.0685}_{-0.0685}$
XS_Wjets_Res	$0.945^{+0.0219}_{-0.0219}$

Table 13.9: Fitted background normalizations for $t\bar{t}$ and $W+jets$ backgrounds for the VBF WZ analysis region.

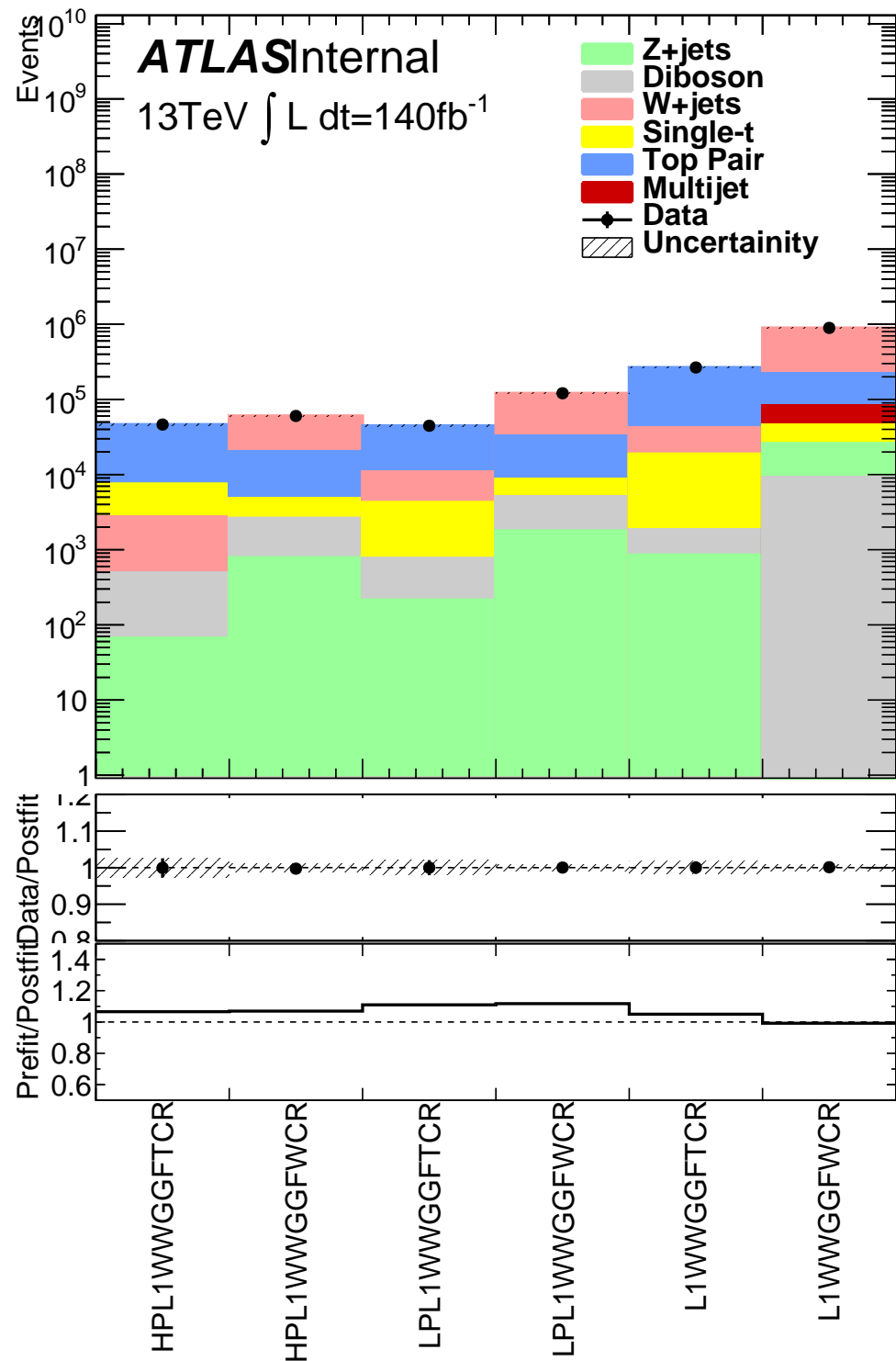


Figure 13.1: This figure shows the distribution of $m_{\ell\nu qq}$ in the DY WW control regions.

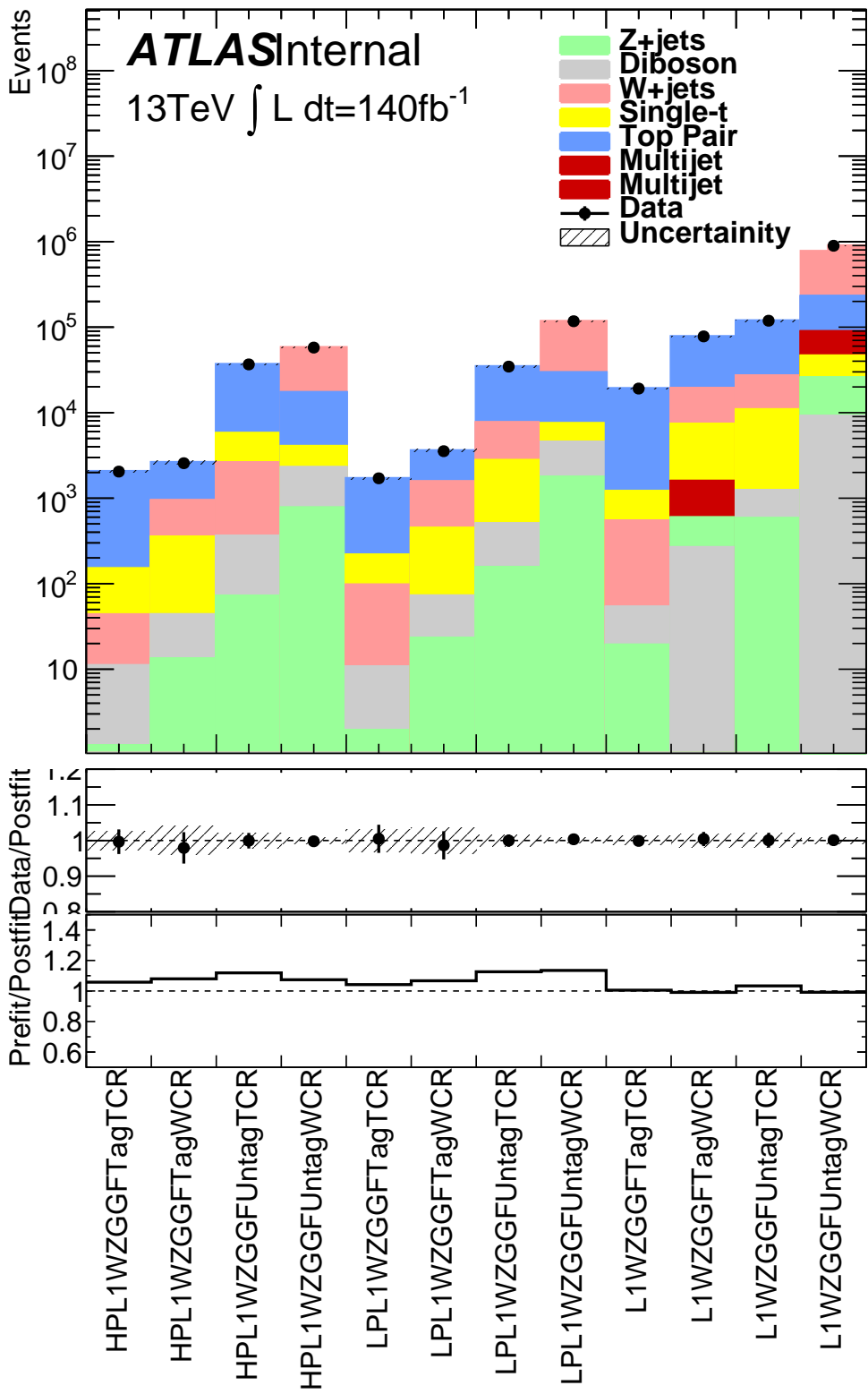


Figure 13.2: This figure shows the distribution of $m_{\ell\nu qq}$ in the DY WZ control regions.

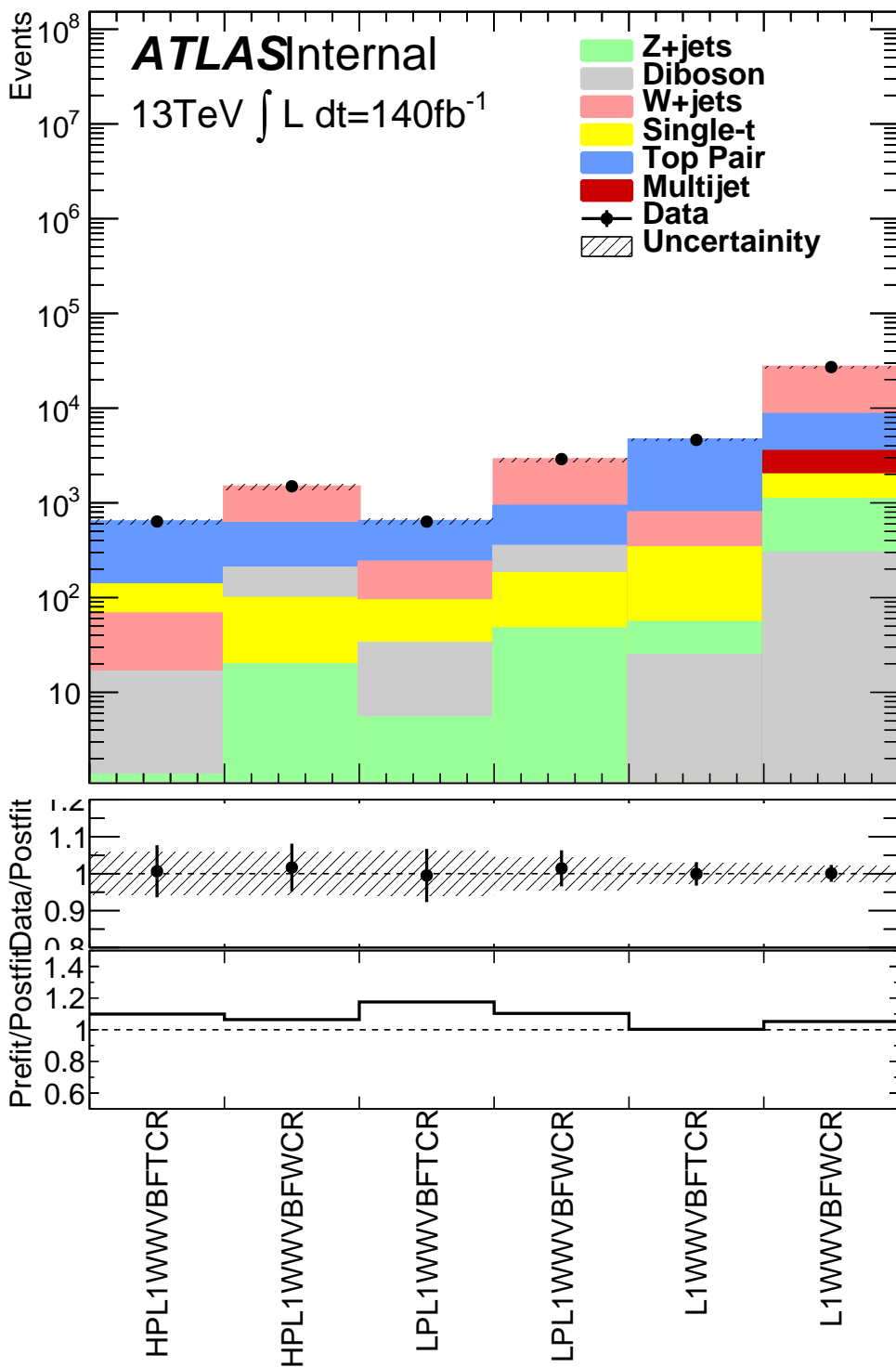


Figure 13.3: This figure shows the distribution of $m_{\ell\nu qq}$ in the VBF WW control regions.

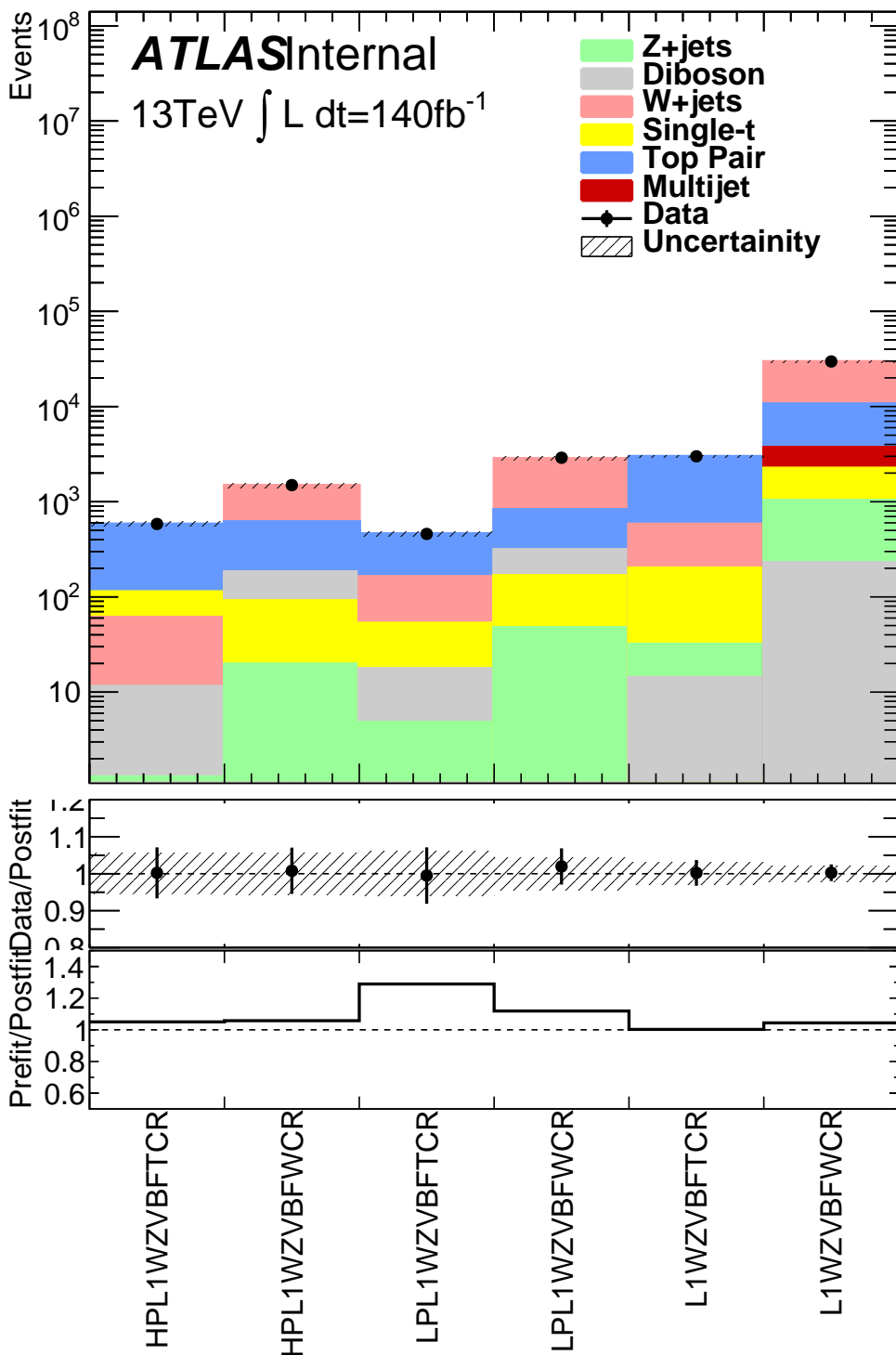


Figure 13.4: This figure shows the distribution of $m_{\ell\nu qq}$ in the VBF WZ control regions.

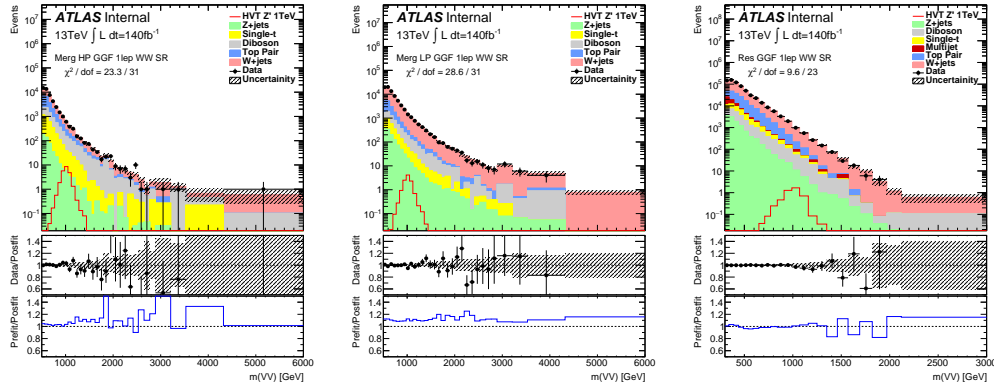


Figure 13.5: This figure shows the distribution of $m_{\ell\nu qq}$ in the GGF WW signal regions.

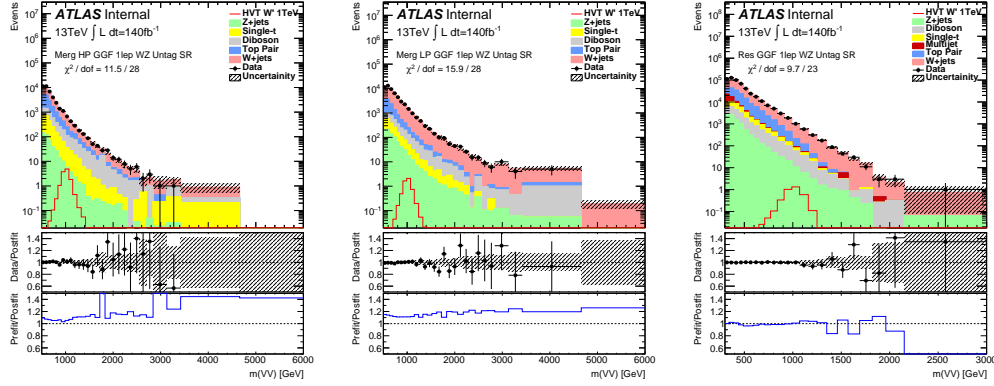


Figure 13.6: This figure shows the distribution of $m_{\ell\nu qq}$ in the GGF WZ Untag signal regions.

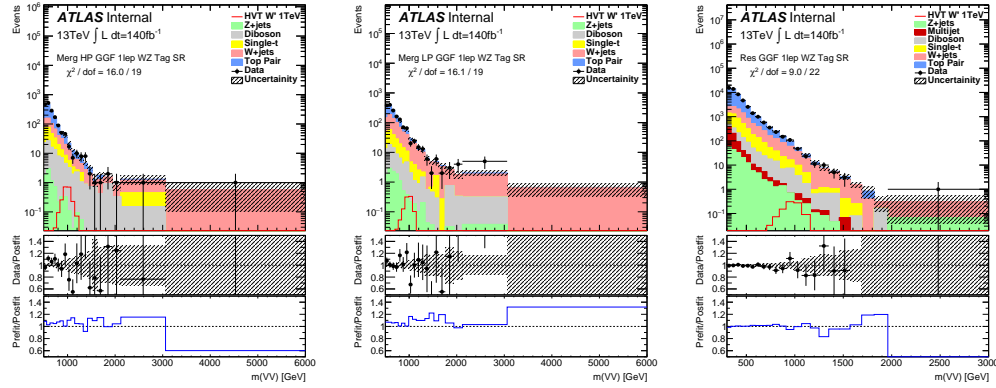


Figure 13.7: This figure shows the distribution of $m_{\ell\nu qq}$ in the GGF WZ Tag signal regions.

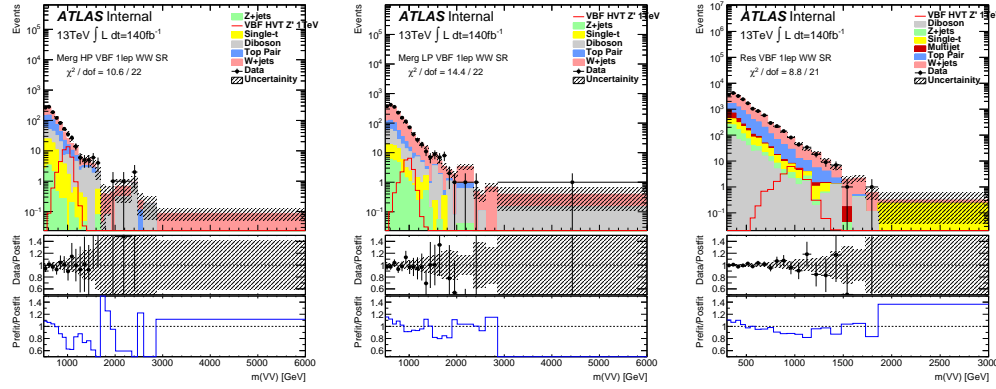


Figure 13.8: This figure shows the distribution of $m_{\ell\nu qq}$ in the VBF WZ Tag signal regions.

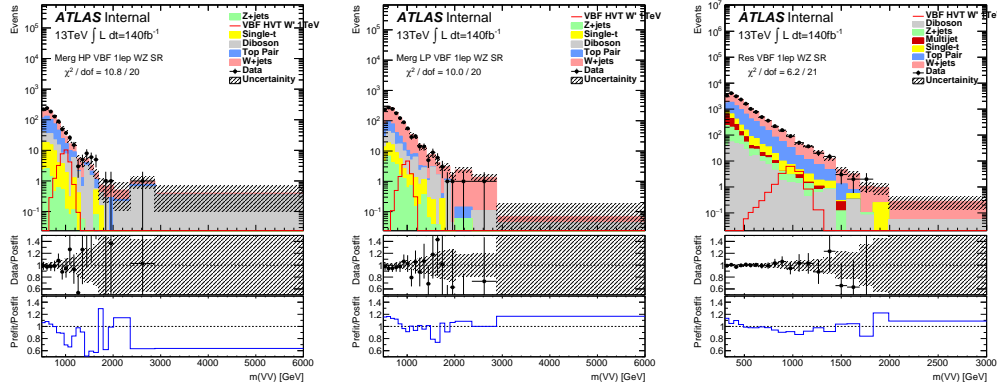


Figure 13.9: This figure shows the distribution of $m_{\ell\nu qq}$ in the VBF WZ Tag signal regions.

13.2 Systematic Profiling and Correlations

1351 The ranked systematics and their fitted values are shown for the different
 1352 analysis regions in Figure 13.10 - 13.12. Note that background normalizations for
 1353 $W+jets$ and $t\bar{t}$ are left free to float in the fit. This means the nominal normal-
 1354 ization values are at one and the uncertainties are not shown in the ranked plots.
 1355 Overall, systematics are not pulled outside their uncertainties, especially nuisance
 1356 parameters that affect the fitted μ value most significantly.

1358 The correlation between systematics are shown in Figures ???. Correlations
 1359 between background normalization are expected. The remaining systematic cor-
 1360 relations are not very strong or unexpected.

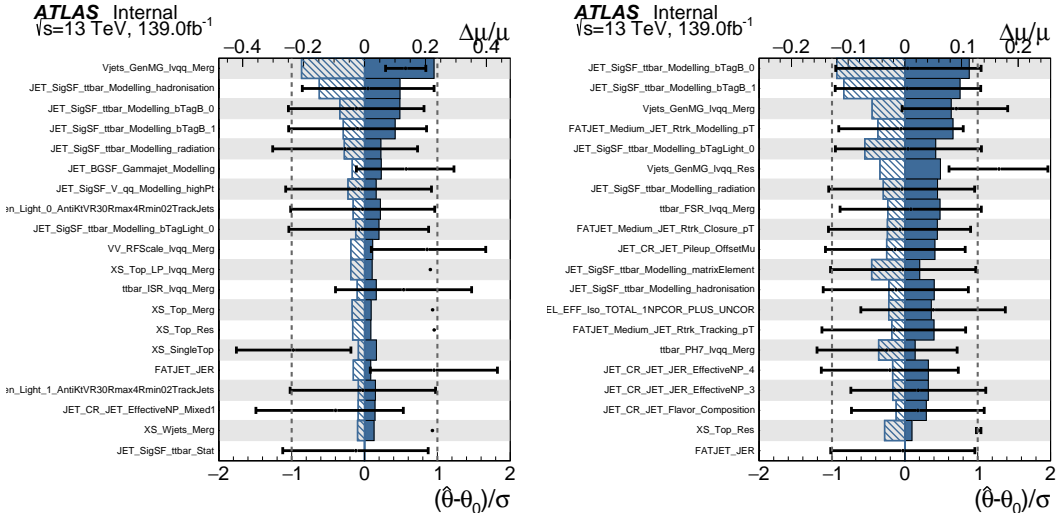


Figure 13.10: Ranked systematics and their fitted values for WW DY (right) and VBF (left) selections.

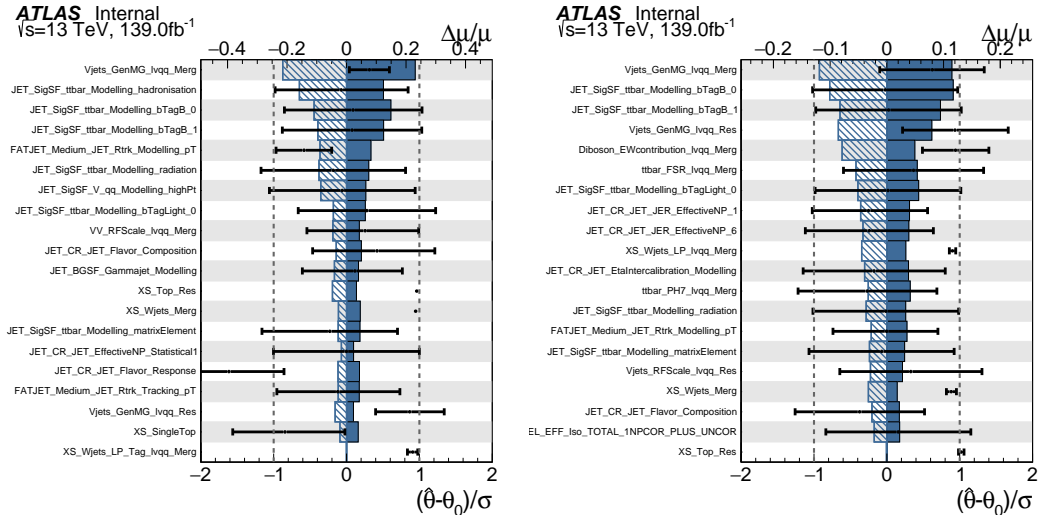


Figure 13.11: Ranked systematics and their fitted values for WZ DY (right) and VBF (left) selections.

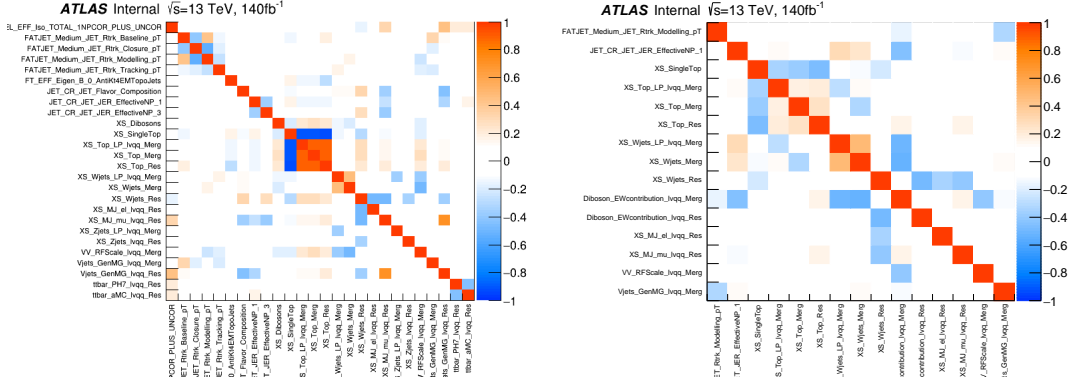


Figure 13.12: Correlations between systematics for WW DY (right) and VBF (left) selections.

13.3 Discovery Tests

To test for the existence of signal in the observed dataset, the discovery tests discussed earlier are used to calculate p-values as a function of resonance mass. The results of these tests are shown in Figures 13.13 - 13.17. Across the different DY signals the largest excesses are $\sim 2.2\sigma$ at 600 GeV and 1.8σ at 2 TeV. The largest excesses for VBF signals are $< 2.5\sigma$ at for 1 TeV resonances. As these deviations do not constitute discoveries, upper limits on μ are calculated.

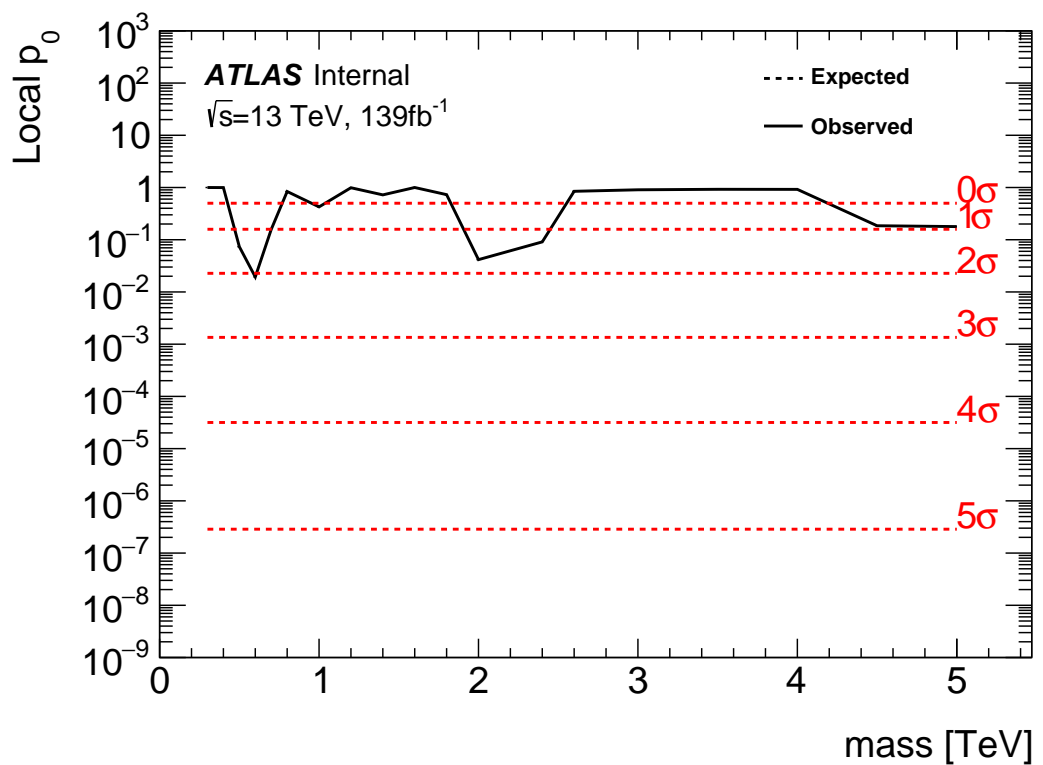


Figure 13.13: These plots show the measured p_0 value as a function of resonance mass for HVT Z' DY production.

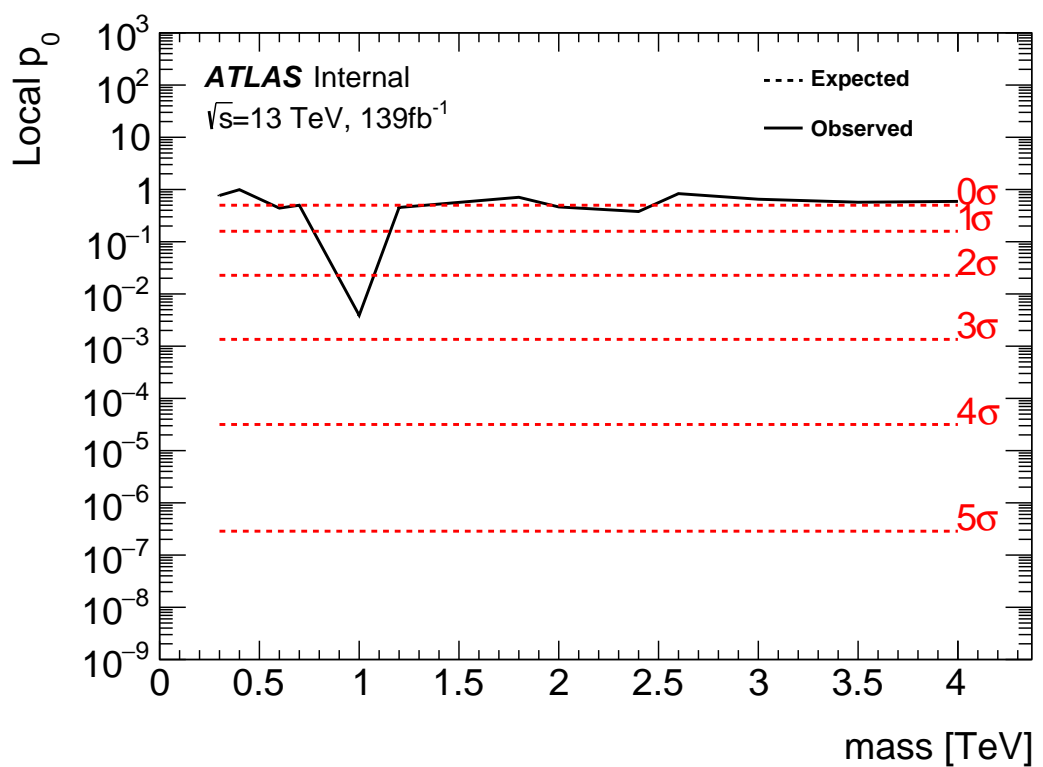


Figure 13.14: These plots show the measured p_0 value as a function of resonance mass for HVT Z' VBF production.

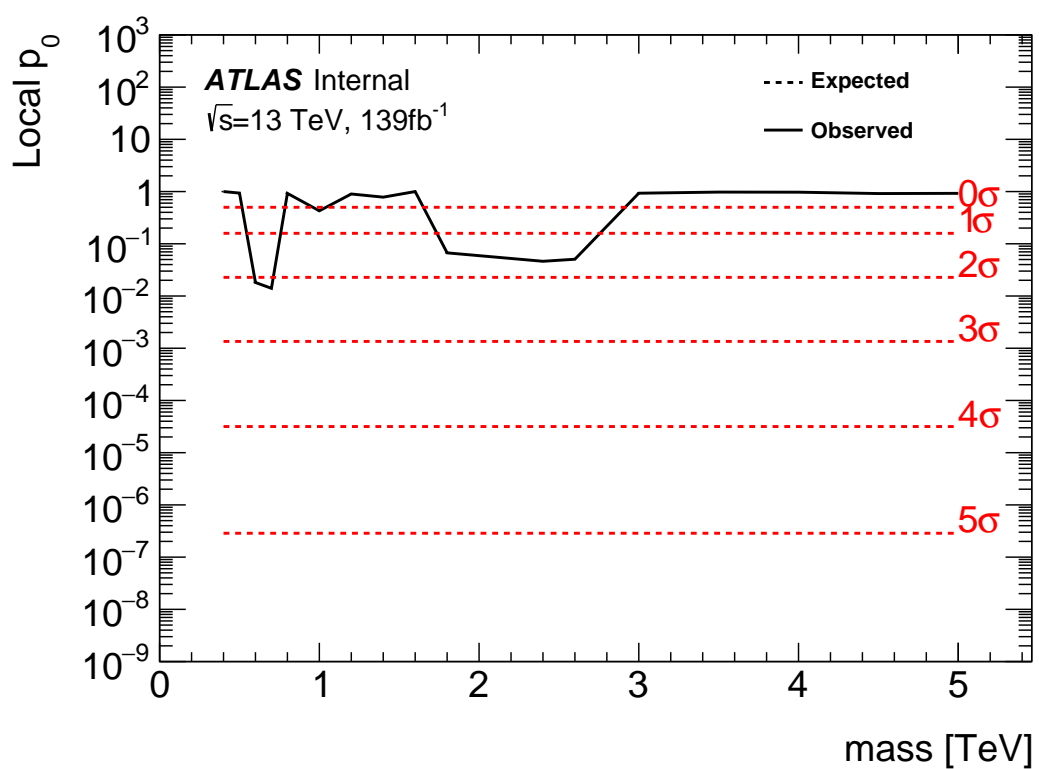


Figure 13.15: These plots show the measured p_0 value as a function of resonance mass for HVT W' DY production.

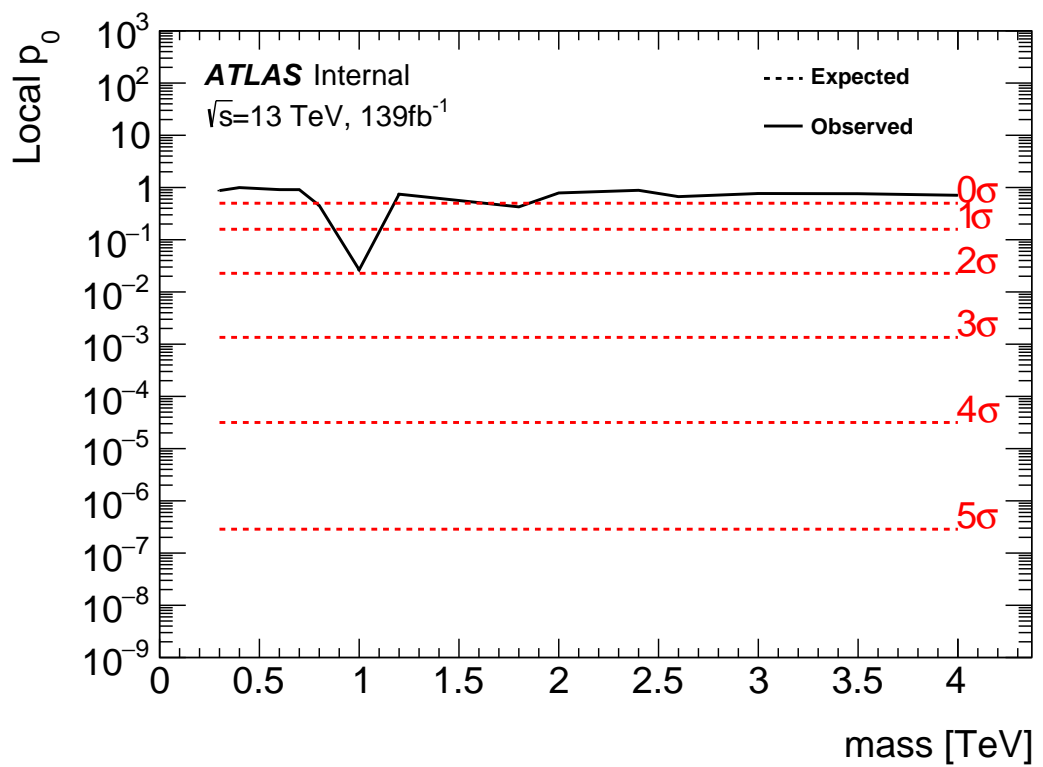


Figure 13.16: These plots show the measured p_0 value as a function of resonance mass for HVT W' VBF production.

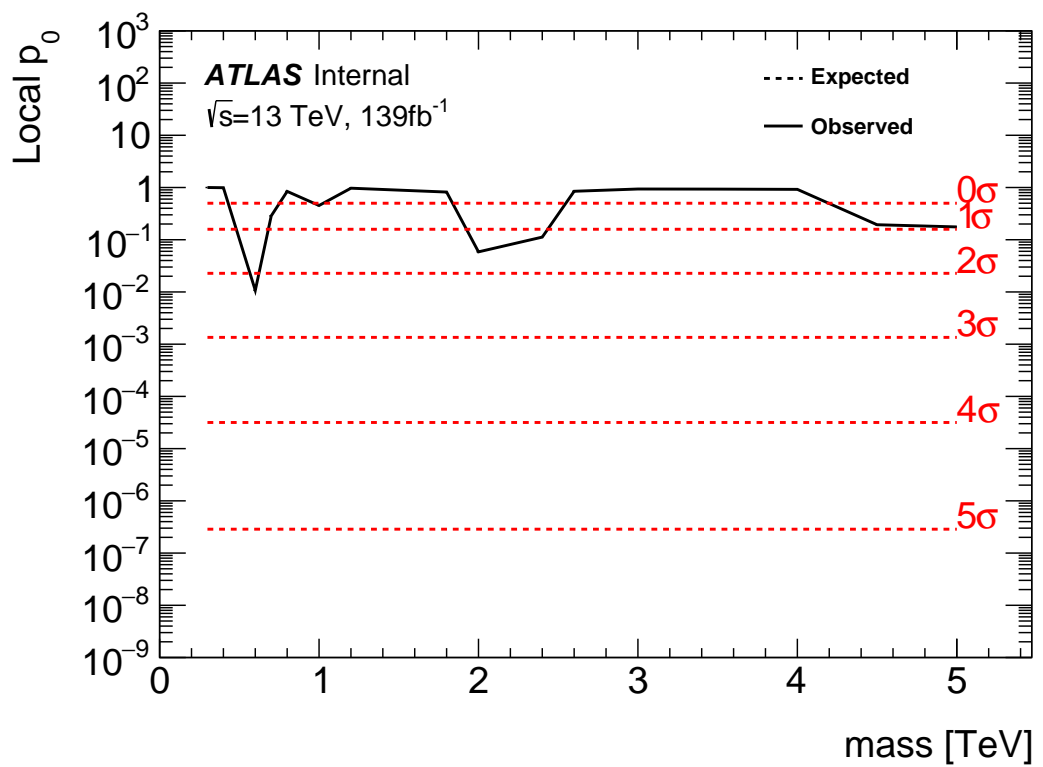


Figure 13.17: These plots show the measured p_0 value as a function of resonance mass for the RS Graviton DY production.

13.4 Limits

Using the exclusion limits tests discussed previously, exclusion limits are set on μ and consequently cross-sections for different signal models. Exclusion limits for the models considered are shown in Figure 13.18 - 13.20. These plots show the theory cross section for a given resonance to decay to WW/WZ . Also, an Asimov dataset is used to calculate the limits that could be set for the background only hypothesis with the associated errors on this predictions. Finally, the observed limits are shown in black. All signal mass where the theory prediction is less than the observed prediction are excluded at the 95% confidence level. These limits shown exclude HVT Model A $W' < 3.4\text{TeV}$ and $Z' < 3.3\text{ TeV}$ and Model B $W' < 3.7\text{ TeV}$ and $Z' < 3.7\text{ TeV}$. Randall Sundrum Gravitons are excluded for masses below 1.6TeV .

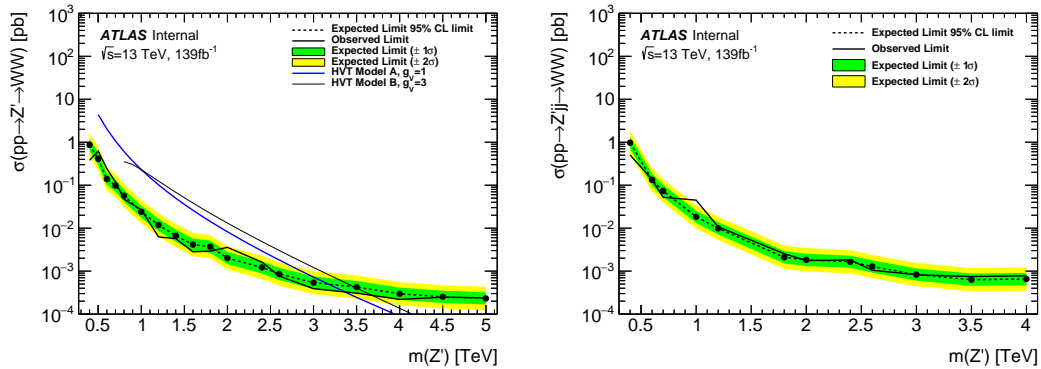


Figure 13.18: This figure shows theory, expected and observed limits for HVT W' DY (left) and VBF (right) production.

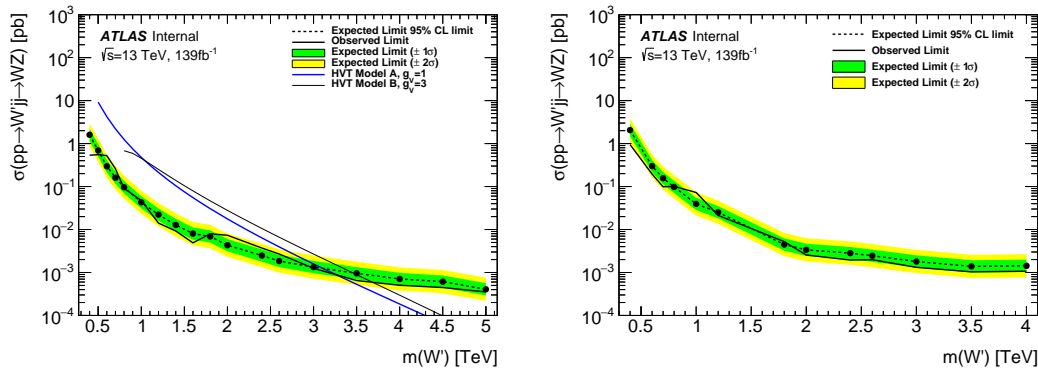


Figure 13.19: This figure shows theory, expected and observed limits for HVT Z' DY (left) and VBF (right) production.

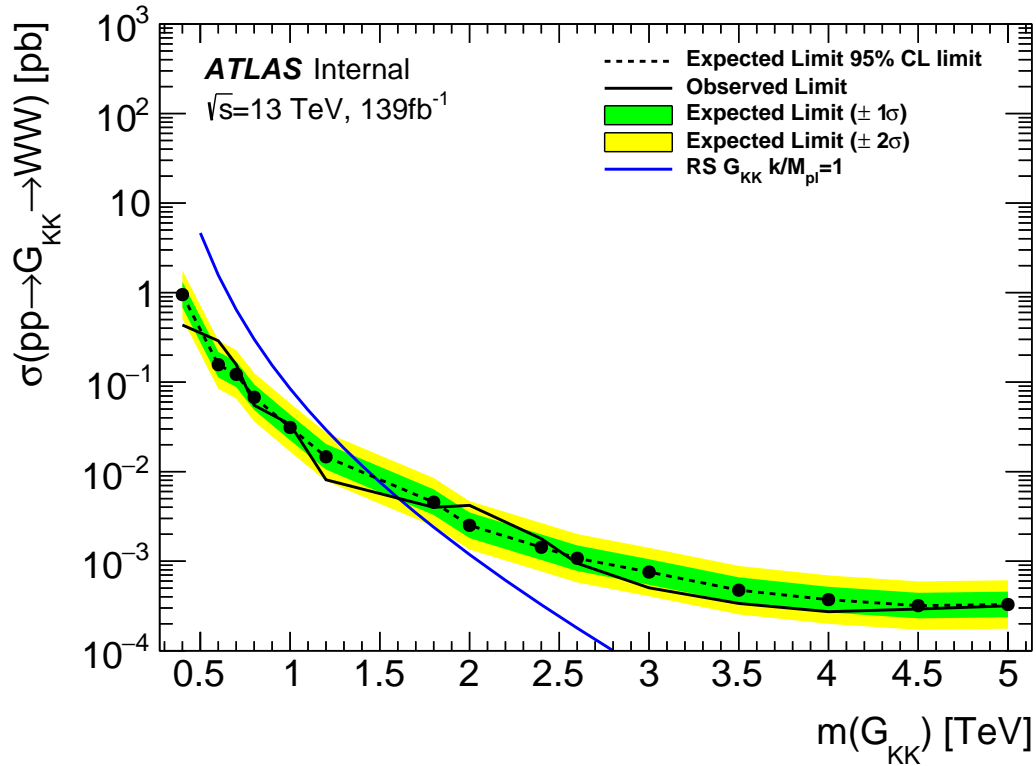


Figure 13.20: This figure shows theory, expected and observed limits for RS Gravitons via DY production.

Part V

1380

Quark and Gluon Tagging

1381

₁₃₈₂ **Chapter 14**

₁₃₈₃ **Prospects**

₁₃₈₄ For the resolved analysis, signal jets are quark enriched and background jets are
₁₃₈₅ gluon dominated. By classifying jets in the event as quark or gluon initiated, less
₁₃₈₆ background would contaminate the signal region. Figure 14.1 shows the PDGID
₁₃₈₇ for the truth parton matched to the jet (meaning the highest energy parton in
₁₃₈₈ the jet catchment area) in events passing the resolved signal region selections.
₁₃₈₉ PDGID = -1 corresponds to pileup jets, $0 < \text{PDGID} < 6$ correspond to quarks
₁₃₉₀ and $\text{PDGID} = 21$ corresponds to gluons. From this Figure, it is evident that a
₁₃₉₁ notable fraction of the background (all background events that passed the resolved
₁₃₉₂ SR are used) that contaminates the signal region contains gluon jets, especially
₁₃₉₃ for the sub-leading jet.

₁₃₉₄ As gluons jets have more constituents and therefore more tracks (n_{trk}), back-
₁₃₉₅ ground jets generally have more tracks than the signal jets. This is shown in
₁₃₉₆ Figure 14.2. Therefore, by cutting on the number of tracks in a jet, quark and
₁₃₉₇ gluon jets may be distinguished (i.e. jets with less than a given number of tracks
₁₃₉₈ are classified as a quark, otherwise the jet is classified as a gluon.) Moreover, as
₁₃₉₉ the momentum of the jet increases the number of tracks also increases logarith-
₁₄₀₀ mically [Cite nachman thesis Natasha], and improves tagging efficiency by about

1401 10% relative to a constant cut on the number of tracks. Therefore by applying a
1402 cut on the number of tracks that scales with the $\ln(p_T)$ is more powerful than a
1403 threshold cut on the number of tracks. Figures 14.3-14.6 show normalized heat
1404 maps of $\ln(p_T)$ vs the number of reconstructed tracks for the background and
1405 HVT Z' signals. This information is also shown in table ???. In these plots it is
1406 evident that the number of tracks in the background jets grows more quickly with
1407 $\ln(p_T)$ than for the signal jets. This is expected given that the signal is quark
1408 dominated and the background is gluon dominated.

1409 In Figure 14.7 is the ROC Curve for quark gluon tagging with cut on the
1410 number of tracks in a jet that depends on $\ln(p_T)$. The sum of the backgrounds
1411 in the signal region were used for this curve. Here the quark tagging efficiency is
1412 the ratio of quarks tagged as quarks to the total number of quarks in the signal
1413 region. The gluon rejection is calculated as the reciprocal of the gluon tagging
1414 efficiency. For example, choosing a 90% efficient working point with a rejection
1415 of 1.4 corresponds to a slope of 4 and intercept of -5. Tagging both jets in this
1416 analysis would yield an efficiency of $90\%^{n_{jets}}$. Focusing on the background in
1417 Figure 14.8, this cut helps minimize gluon contamination in the signal region.
1418 Also, from these heat maps it is obvious that the number of tracks in gluon jets
1419 grows more quickly than those in quark jets.

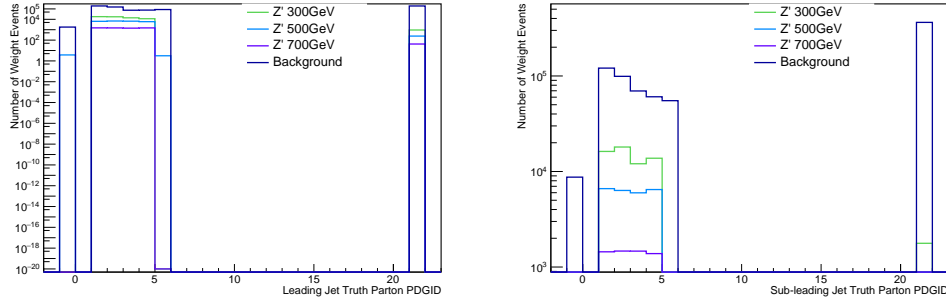


Figure 14.1: PDGID of the truth-level parton matched to the small-R jets passing the Resolved GGF WW Signal Region selections for the (a) Leading (b) Sub-Leading jets . These distributions are shown for 300, 500, and 700GeV Z' signals and the background (all simulated backgrounds that pass SR selections).

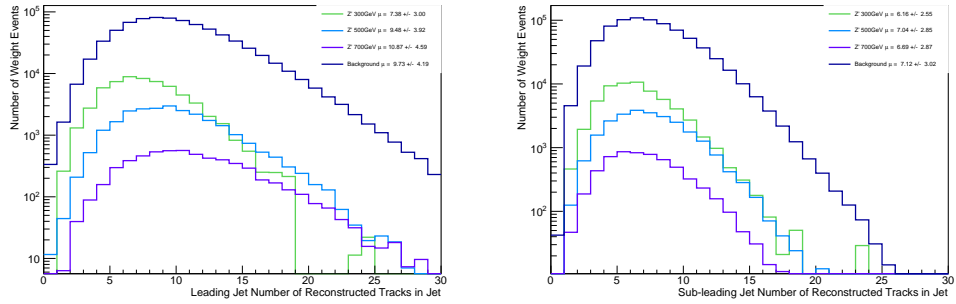


Figure 14.2: The number of tracks in small-R jets in events passing the Resolved GGF WW Signal Region selections for the (a) Leading (b) Sub-Leading jets. These distributions are shown for 300, 500, and 700GeV Z' signals and the background.

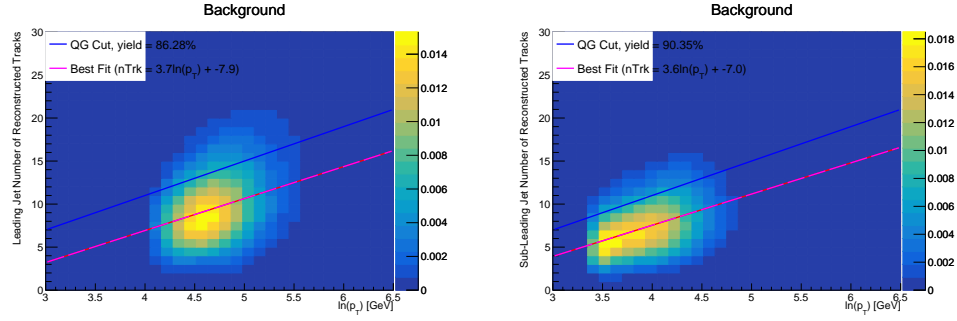


Figure 14.3: The number of tracks in background small-R jets in events passing the Resolved GGF WW Signal region selection vs. $\ln(p_T)$ for (a)Leading (b) Sub-Leading jets. The best fit line for the distribution is also shown, as well as the percentage of jets that pass a cut of number of tracks $< 4 \times \ln(p_T) - 5$. Note the number of total entries in these plots has been normalized to one.

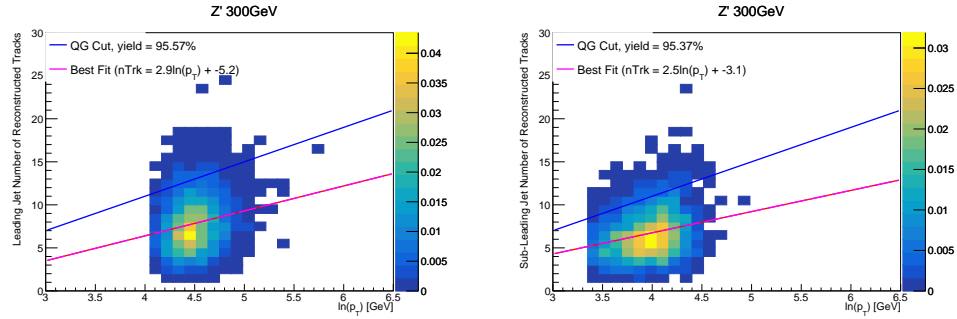


Figure 14.4: The number of tracks in small-R jets in 300GeV Z' events passing the Resolved GGF WW Signal region selection vs. $\ln(p_T)$ for (a)Leading (b) Sub-Leading jets. The best fit line for the distribution is also shown, as well as the percentage of jets that pass a cut of number of tracks $< 4 \times \ln(p_T) - 5$. Note the number of total entries in these plots has been normalized to one.

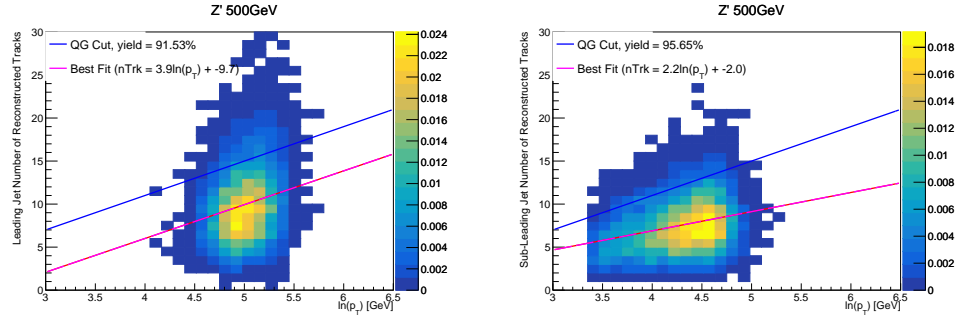


Figure 14.5: The number of tracks in small-R jets in 500GeV Z' events passing the Resolved GGF WW Signal region selection vs. $\ln(p_T)$ for (a)Leading (b) Sub-Leading jets. The best fit line for the distribution is also shown, as well as the percentage of jets that pass a cut of number of tracks $< 4 \times \ln(p_T) - 5$. Note the number of total entries in these plots has been normalized to one.

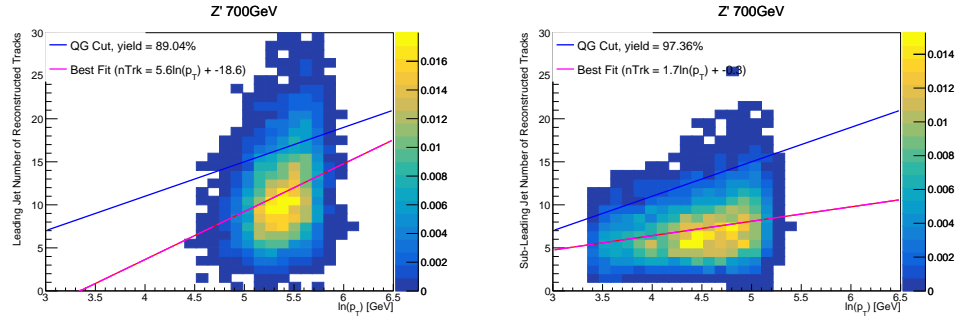


Figure 14.6: The number of tracks in small-R jets in 700GeV Z' events passing the Resolved GGF WW Signal region selection vs. $\ln(p_T)$ for (a)Leading (b) Sub-Leading jets. The best fit line for the distribution is also shown, as well as the percentage of jets that pass a cut of number of tracks $< 4 \times \ln(p_T) - 5$. Note the number of total entries in these plots has been normalized to one.

Sample	Best Fit Slope	Best Fit Intercept	QG Tag Yield
Backgrounds	3.7	-7.9	86%
HVT Z' 300 GeV	2.9	-5.2	95%
HVT Z' 500 GeV	3.9	-9.7	92%

Table 14.1: This table shows the best fit slope and intercept for the 2-d distribution of number of tracks vs. jet $\ln(p_T)$ for the leading jet in the background and HVT Z' samples. The tagging efficiency is shown for the 90% working point in the last column. The background jets contain more gluons than the signal jets. Consequently, the best fit line for the background predicts larger values of the number of tracks in jets for the background than the considered signals.

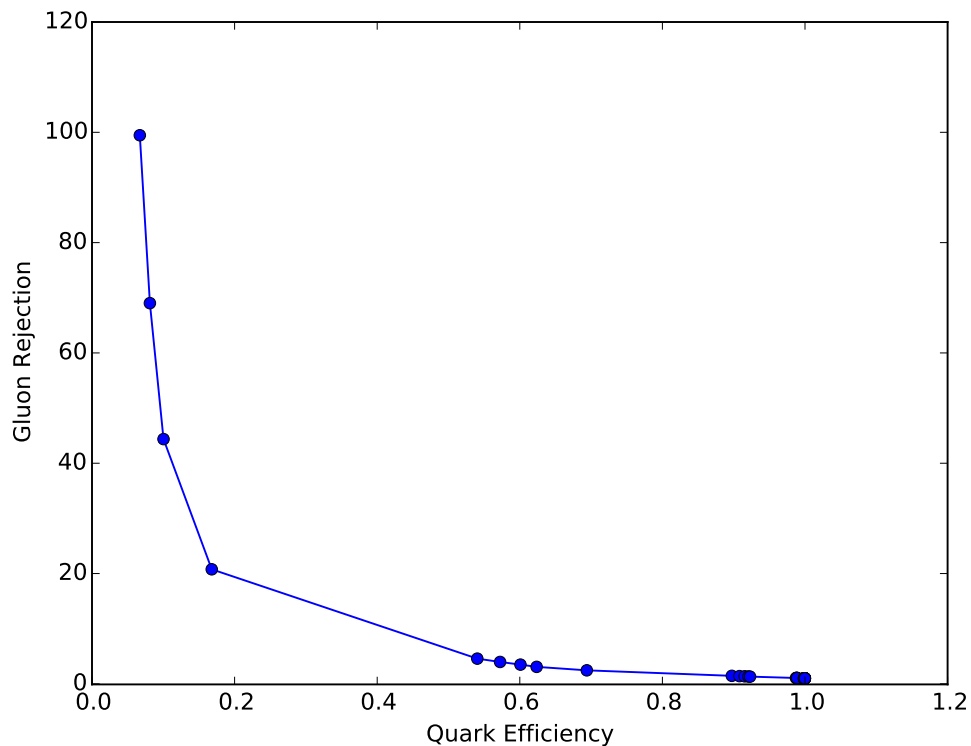


Figure 14.7: ROC Curve for Quark and Gluon Tagging with a cut on the number of tracks that depends on the $\ln(p_T)$.

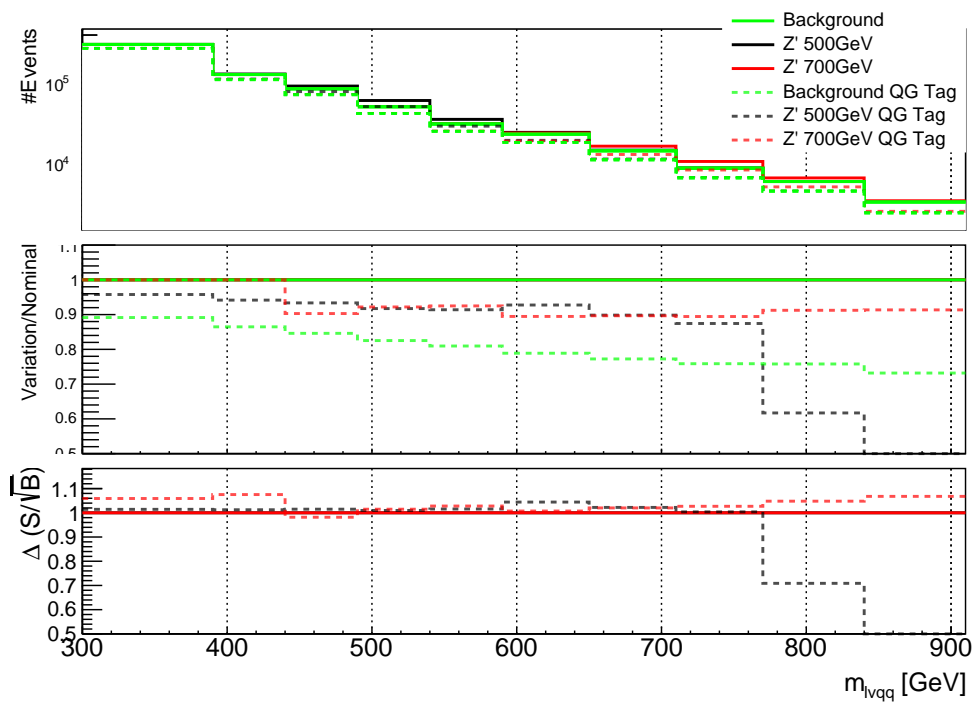


Figure 14.8: The top panel shows the distribution of m_{lvqq} with and without quark gluon tagging. The middle panel shows the ratio of the signals and backgrounds with and without quark gluon tagging. The bottom panel shows the change in S/\sqrt{B} with quark gluon tagging.

1420 **Chapter 15**

1421 n_{trk} Calibration

1422 The number of tracks in jets depends on modeling and experimental systemat-
1423 ics. Consequently, the efficiency of a quark-gluon tagger based on the number of
1424 tracks in jets would have associated uncertainties. In the context of the resonance
1425 search discussed, these uncertainties would be treated as systematics that impact
1426 the m_{WV} distributions that are used for discovery tests.

1427 Modeling uncertainties are obtained by assessing PDF and ME uncertainties
1428 on the number of charged particles in particle-level jets in dijet events. The
1429 number of charged particles as a function of jet p_T is calculated using an Iterative
1430 Bayesian (IB) technique [cite paper].

1431 This measurement ([11]) uses the ATLAS 2012 pp collision dataset, corre-
1432 sponding to $20.3/\text{fb}$ at center-of-mass energy $\sqrt{s} = 8\text{TeV}$. The number of charged
1433 constituents depends on fragmentation modeling and matrix elements, which
1434 do not depend on s . For this reason, it is safe to use these uncertainties for
1435 $\text{sqrt}(s)=13\text{TeV}$. Monte Carlo (MC) samples are used to determine the response
1436 matrix. The MC sample is a dijet sample generated with Pythia 8.175 using CT10
1437 PDF and AU2 tune. The anti- k_T algorithm is used to cluster jets with a radius
1438 parameter $R = 0.4$. Jets are required to have $|\eta| < 2.1$. Tracks in jets are re-

1439 quired to have $p_T > 500\text{MeV}$, $|\eta| < 2.5$, track-fit $\chi^2 < 3.0$ and originate from the
1440 primary vertex. Matching tracks to jets is accomplished using ghost-association
1441 [cite]. In this technique, jets are re-clustered with the track collection augmented
1442 with "ghost" versions of tracks. These "ghosts" tracks have the same direction as
1443 their parent track, but infinitesimal track p_T . This insures meta-jet properties
1444 (e.g. η , p_T , etc) are unchanged. A track is matched to a jet if it's ghost version
1445 remains in the jet after re-clustering. Further details of the data, object, and
1446 event selection may be found in [cite 35].

1447 To select dijet topologies events are required to have at least two jets with
1448 $p_T > 50\text{GeV}$ that are relatively well-balanced ($p_T^{\text{lead}}/p_T^{\text{sub-lead}} < 1.5$).

1449 In the IB technique, the prior distribution and number of iterations are the
1450 inputs [cite Bayesian paper]. The IB response matrix connects number of charged
1451 particles to the number of tracks in jets determined using the simulated samples.
1452 This response matrix is used to unfold data to extract the n_c . Before applying
1453 the response matrix a fake factor is applied. This accounts for jets that pass
1454 detector level selections, but not particle level selections. Following this, the IB
1455 method iteratively applies the response matrix using the nominal Pythia 8.175
1456 sample as a prior. The number of IB iterations is chosen to minimize unfolding
1457 bias and statistical fluctuations. For this measurement four iterations was found
1458 to be optimal by minimizing the unfolding bias from pseudodata simulated with
1459 Herwig++ with a prior from Pythia 8 AU2. Finally, the inefficiency factor is
1460 applied to account for events passing particle level selection but not detector
1461 level, yielding the unfolded nCharged distribution.

1462 This process is prone to three main sources of bias: response matrix, correction
1463 factor, and unfolding procedure uncertainties. The response matrix is sensitive to
1464 experimental uncertainties impacting jet track reconstruction and calorimeter jet

1465 p_T . Correction factors are also sensitive to experimental uncertainties (e.g. JES)
 1466 as such uncertainties modify detector level acceptance. Sensitivity to particle
 1467 level acceptance is calculated by comparing Pythia and Herwig. Finally, the bias
 1468 from the IB prior choice is determined by reweighting the particle-level spectrum,
 1469 so the simulated detector level spectrum more closely matches the uncorrected
 1470 data. Unfolding this modified detector-level simulation and comparing it to the re-
 1471 weighted particle-level spectrum indicates bias from the prior distribution choice.

1472 A summary of all the systematic uncertainties associated with this unfolding
 1473 may be found in [ref paper]. Total uncertainties are < 7% for the number of
 1474 charged particles in jets. The unfolded distribution of the nCharged in jets from
 1475 data are further analyzed to extract the quark and gluon nCharged distributions.
 1476 In dijet events, the jet with a larger η is more energetic and therefore more likely
 1477 to be a quark. This is due to the quarks in protons generally having a larger
 1478 fraction of the total momentum of the proton constituents. The more central jet
 1479 is more likely to be a gluon-initiated jet. This correlation between jet η and flavor
 1480 may then be used to extract nCharged in p_T bins using:

$$\langle n_c^f \rangle = f_q^f \langle n_c^q \rangle + f_g^f \langle n_c^g \rangle \quad (15.1)$$

1481

$$\langle n_c^c \rangle = f_q^c \langle n_c^q \rangle + f_g^c \langle n_c^g \rangle \quad (15.2)$$

1482 In this equation the f and c subscripts denote the more forward and central
 1483 jets, respectively. The q and g subscripts denote quark and gluon. The fraction
 1484 of more forward jets that are say gluons is denoted by f_g^f . The other relevant jet
 1485 fractions are denoted with the same naming scheme. Finally, $\langle n_c \rangle$ is the average
 1486 number of charged particles in a jet in a given p_T bin. To show that Eq. (??) may
 1487 be used to extract quark and gluon n_c distributions the extracted distributions
 1488 are compared to n_c distributions determined using the jet flavor in simulation.

1489 Figure [add figure natasha] shows that the extracted and true distributions differ
1490 by < 1% over the p_T range probed for this study. Moreover, this implies that n_c
1491 depends only on the flavor of the initiating parton and jet p_T .

1492 These extracted distributions are prone to PDF and ME biases. The bias from
1493 the choice of the CT10 PDF for the Pythia sample is accounted for by comparing
1494 quark/gluon fractions for the nominal CT10 sample with its eigenvector variations.
1495 Comparing the quark/gluon fractions from Pythia 8 and Herwig++ quantify the
1496 uncertainty from the ME calculation. These uncertainties are added in quadra-
1497 ture with the unfolding uncertainty to give the total modelling uncertainty on
1498 the extracted n_c distribution. This is shown in Figure 16.2.

1499 To apply these uncertainties in n_c distributions in data, per-jet event weights
1500 are associated with each uncertainty according to:

$$w_i(n_c) = \frac{P(n_c | n_c > \pm \sigma_{n_c}^i)}{P(n_c | n_c >)} \quad (15.3)$$

1501 In Eq. (??), i denotes the uncertainty considered, P is the Poisson probability,
1502 and $\sigma_{n_c}^i$ represents the average impact of the uncertainty on n_c .

1503 The previous uncertainties described accounted for modeling uncertainty as-
1504 sociated with the number of charged particles in a jet. However, n_c is not a
1505 measurable quantity. Instead the number of tracks in a jet is measured, which is
1506 a proxy for n_c . Therefore the uncertainties associated with the measurement of
1507 nTracks must also be considered ([13]). These uncertainties were calculated using
1508 a Pythia 8 dijet sample with NNPDF 23 and Run 2 data. Track reconstruction
1509 efficiency and fake rates are the dominant sources of nTrack uncertainties.

1510 The track reconstruction efficiency is affected by the uncertainty of the de-
1511 scription of the ID material in simulation and the modeling of charged-particle
1512 interactions with this material. These uncertainties are accounted for by varying

1513 the ID material by 5-25% (dependent on the region of the detector considered).
1514 The difference in the tracking efficiency between the nominal and varied simula-
1515 tion give the uncertainty on the track reconstruction efficiency. Another important
1516 source of track reconstruction inefficiency arises in the core of jets. The high den-
1517 sity of tracks in the jet cores can cause ID clusters to merge. The fraction of lost
1518 tracks due to merging is given by the fraction of tracks that have a charge of two
1519 minimum ionizing particles. This quantity is compared between data and simu-
1520 lation resulting in an uncertainty of 0.4% on tracks with $\Delta R < 0.1$. Combining
1521 these effects gives a total uncertainty as a function of p_T and η that is generally
1522 $< 2\%$ [references figure 44 from [13]).

1523 Fake tracks are the other dominant source of nTrk uncertainty. Fake tracks
1524 are tracks that cannot be associated to a single particle. Often these tracks are a
1525 result of random combinations of hits from charged particles that overlap in space.
1526 In dense environments, such as the core of jets or high-pileup environments, fake
1527 tracks are more likely. Fake tracks are estimated with a 'control region method'
1528 which is briefly summarized here [[12]]. By applying a series of track selections
1529 to enrich the fraction of fake tracks (e.g. $|d_0| > 0.1$, track $\chi^2 > 1.4$, etc) in
1530 simulation, templates for fake track parameters are calculated. These templates
1531 are then fit to data to determine the fraction of fake tracks. On average the fake
1532 rate is found to be 30% (independent of p_T and η).

1533 To assess the impact of these two detector level uncertainties, tracks are ran-
1534 domly dropped according to the rates described above. Reconstruction and fake
1535 uncertainties both lower the number of tracks, hence these uncertainties are one-
1536 sided. By dropping tracks in this way a varied nTrk distribution is calculated for
1537 both uncertainties. The associated per-jet event weights are then calculated in
1538 the same way as the modeling weights as:

$$w_i(n_c) = \frac{P(n_{trk} | < n_{trk} > \pm \sigma_{n_{trk}}^i)}{P(n_{trk} | < n_{trk} >)} \quad (15.4)$$

1539 Adding the modeling and detector level uncertainties in quadrature gives the
 1540 overall nTrack uncertainty. The effects of the individual uncertainties on the nTrk
 1541 distributions can be seen in Fig 16.4. Fig 16.3 shows the m_{lvqq} and nTrk distri-
 1542 butions for the W and Top control regions before likelihood fitting. In these plots
 1543 the nTrk uncertainties improve agreement between data and MC. The remaining
 1544 differences are likely covered by likelihood fitting and improving the analysis itself.

₁₅₄₅ **Chapter 16**

₁₅₄₆ **Application**

₁₅₄₇ Using the 90% WP of the n_{trk} tagger improves S/\sqrt{B} is $\sim 3\%$ as shown in
₁₅₄₈ Figure 14.8. Although, n_{trk} is the single most powerful discriminating variable
₁₅₄₉ for quark and gluon jets, the addition of other jet variables would improve the
₁₅₅₀ classification efficiency. Figure 16.1 shows the possible improvement of 10%
₁₅₅₁ in jet classification using the truth label of the jets to classify jets. This type of
₁₅₅₂ improvement is possible by using variables such as jet width, and energy correlata-
₁₅₅₃ tors. Figure [add BDT figure/use 1612.01551.pdf] shows for a 90% quark tagging
₁₅₅₄ efficiency for a 100 GeV jet, a BDT improve the gluon rejection by 0.4. Once this
₁₅₅₅ tagger is calibrated it would improve the analysis sensitivity of this channel.

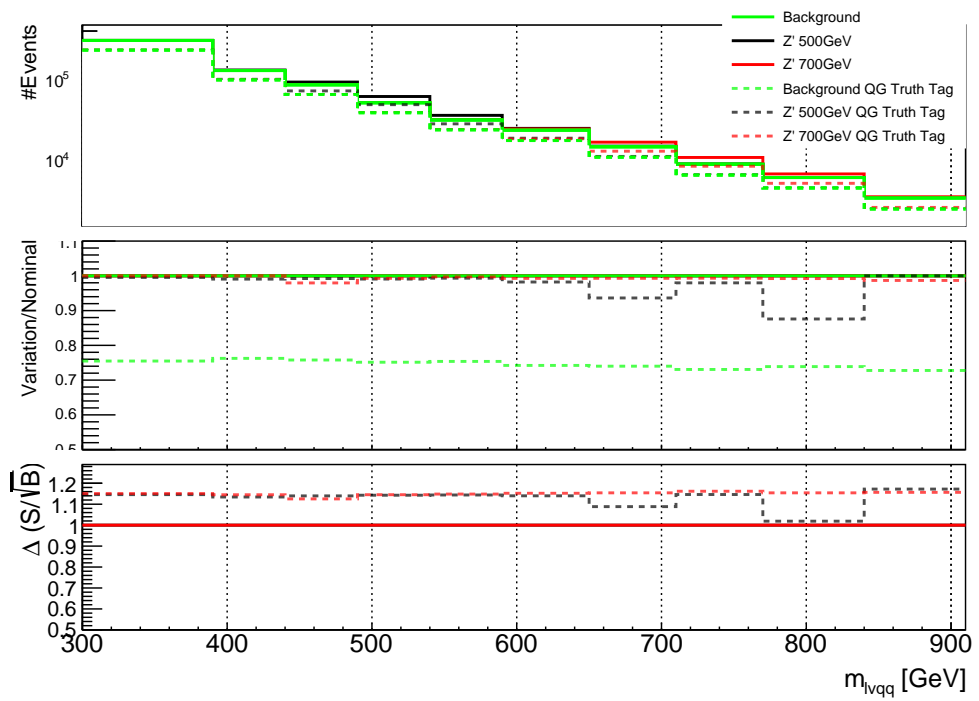


Figure 16.1: The top panel shows the distribution of m_{lvqq} with and without requiring jets to be true quarks. The middle panel shows the ratio of the signals and backgrounds with and without requiring jets to be true quarks. The bottom panel shows the change in S/\sqrt{B} when requiring jets to be true quarks..

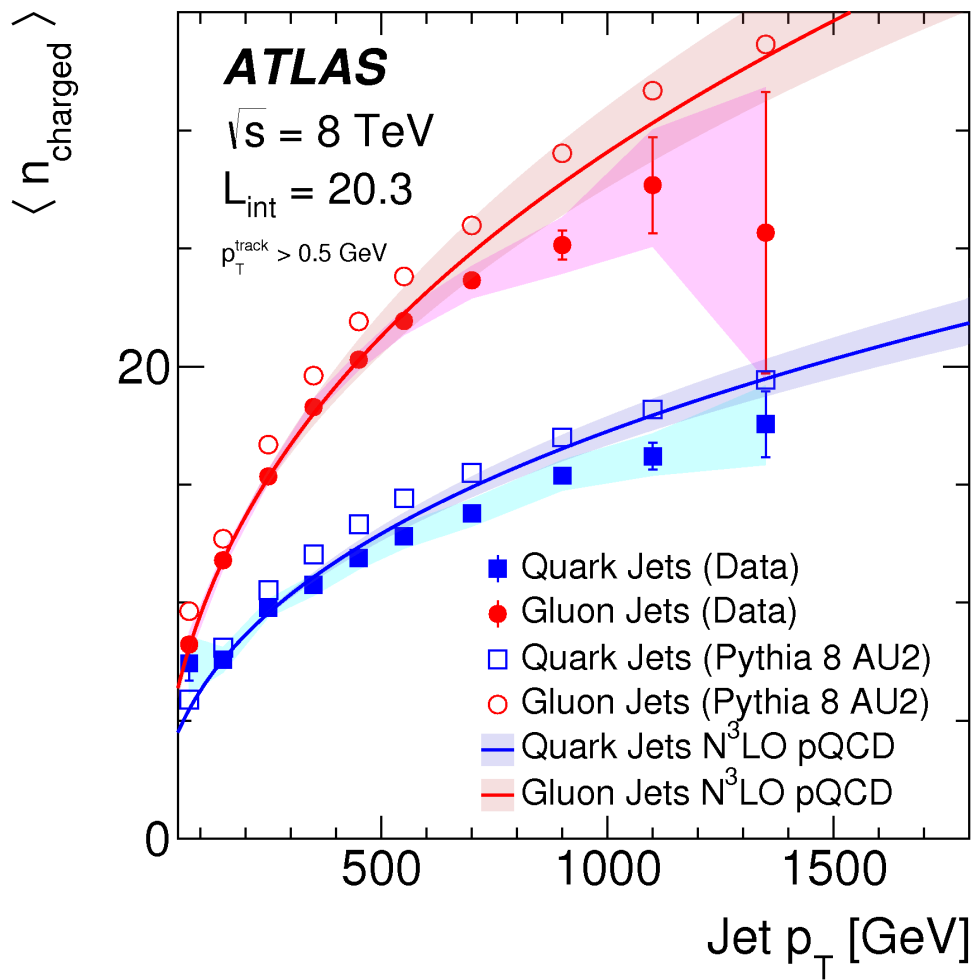


Figure 16.2: Unfolded and extracted n_C qg dstbs..

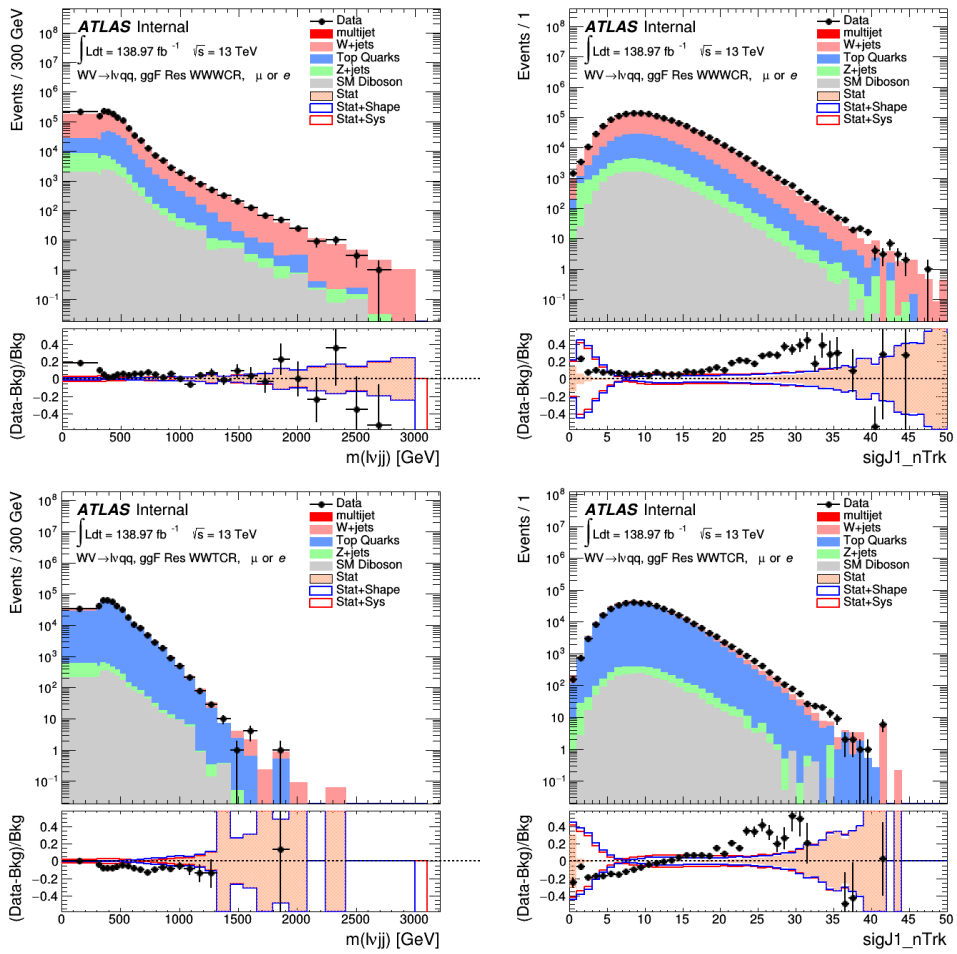


Figure 16.3: PDGID of the truth-level parton matched to the small-R jets passing the Resolved GGF WW Signal Region selections for the (a) Leading (b) Sub-Leading jets . These distributions are shown for 300, 500, and 700GeV Z' signals and the background.

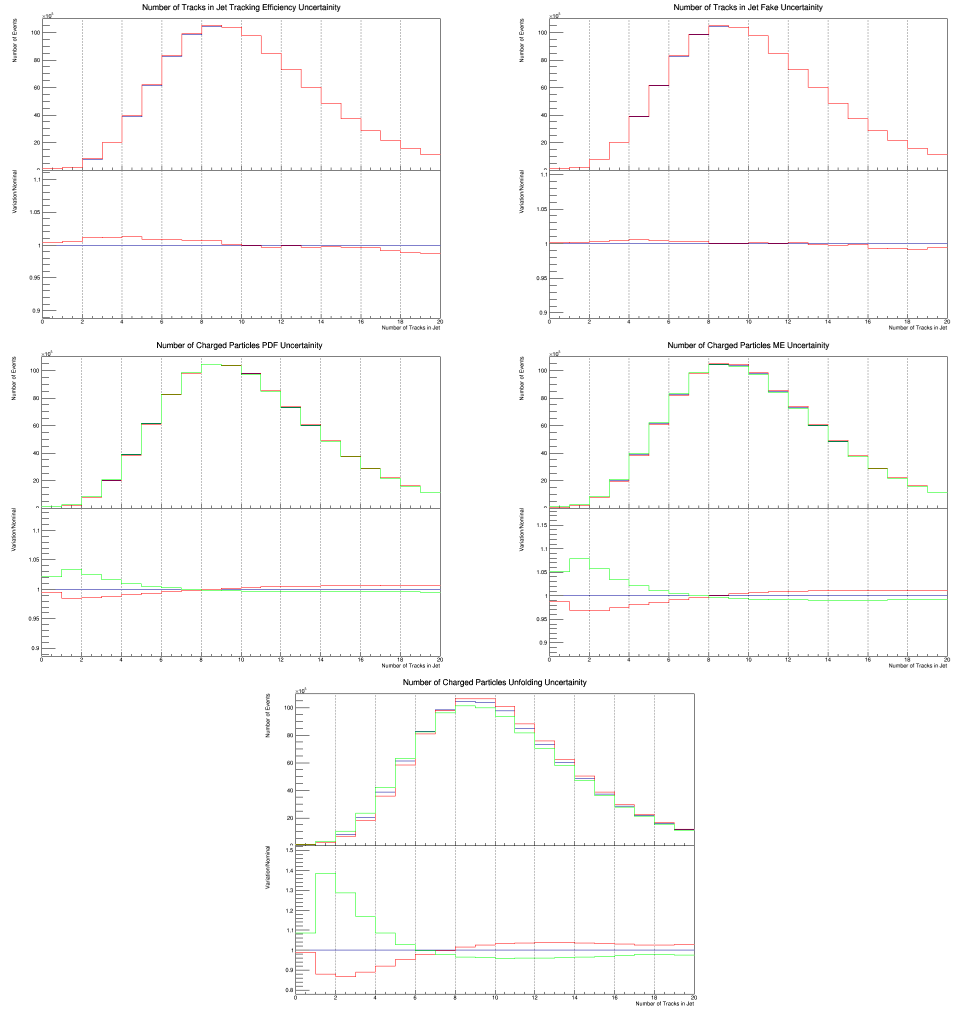


Figure 16.4: These figures show the impact of the uncertainties on the number of tracks in the leading jet in the sum of the background sample in the Resolved GGF WW SR (a) tracking efficiency (b) fake (c) PDF (d) ME (e) unfolding uncertainties.

Part VI

1556

Conclusion

1557

1558 **Chapter 17**

1559 **Conclusions**

1560 A search for WW and WZ diboson resonance production in $\ell\nu qq$ final states
1561 was performed using 139fb^{-1} of pp collision data collected at a center-of-mass
1562 energy of $\sqrt{s} = 13\text{TeV}$ by that ATLAS detector at the LHC between 2015 and
1563 2018. No excess of events above the background-only expectation was observed.
1564 The largest local excess is approximately 2.7σ , which is not significant. Limits
1565 on the production cross section are obtained for the HVT W' and Z' and RS
1566 Gravitons. Signal masses below 3.4 (3.7) TeV are excluded for HVT W' Model
1567 A(B). Signal masses below 3.3 (3.7) TeV are excluded for HVT Z' Model A(B).
1568 Randall Sundrum Gravitons are excluded for masses below 1.6 TeV. Going forward,
1569 improving the classification of jets in events would improve analysis sensitivity.
1570 To distinguish quark from gluon jets a jet tagger based on the number of tracks in
1571 jets is studied in the context of this search. Finally, the calibration of the number
1572 of tracks in jets is discussed.

₁₅₇₃ **Bibliography**

- ₁₅₇₄ [1] Lecture notes particle physics ii.
- ₁₅₇₅ [2] Kaustubh Agashe, Hooman Davoudiasl, Gilad Perez, and Amarjit Soni.
₁₅₇₆ Warped Gravitons at the LHC and Beyond. *Phys. Rev.*, D76:036006, 2007.
- ₁₅₇₇ [3] G. Altarelli and G. Parisi. Asymptotic freedom in parton language. *Nuclear*
₁₅₇₈ *Physics B*, 126(2):298 – 318, 1977.
- ₁₅₇₉ [4] Matteo Cacciari, Gavin P. Salam, and Gregory Soyez. Fastjet user manual.
₁₅₈₀ *The European Physical Journal C*, 72(3), Mar 2012.
- ₁₅₈₁ [5] M. N. Chernodub. Background magnetic field stabilizes qcd string against
₁₅₈₂ breaking, 2010.
- ₁₅₈₃ [6] ATLAS Collaboration. Atlas muon reconstruction performance in lhc run 2.
- ₁₅₈₄ [7] ATLAS Collaboration. Summary plots from the atlas standard model physics
₁₅₈₅ group.
- ₁₅₈₆ [8] ATLAS Collaboration. Tagging and suppression of pileup jets with the atlas
₁₅₈₇ detector. *ATLAS-CONF- 2014-018*, 2014.
- ₁₅₈₈ [9] ATLAS Collaboration. Jet energy scale measurements and their systematic
₁₅₈₉ uncertainties in proton-proton collisions at $\sqrt{s} = 13$ tev with the atlas detec-
₁₅₉₀ tor. *Physical Review D*, 96(7), Oct 2017.
- ₁₅₉₁ [10] ATLAS Collaboration. Jet energy scale measurements and their systematic
₁₅₉₂ uncer- tainties in proton–proton collisions at $\sqrt{s} = 13$ tev with the atlas
₁₅₉₃ detector. arXiv: 1703.09665 [hep-ex].
- ₁₅₉₄ [11] ATLAS Collaboration. Measurement of the charged-particle multiplicity
₁₅₉₅ inside jets from $s=\sqrt{8}$ tev pp collisions with the atlas detector.
₁₅₉₆ arXiv:1602.00988 [hep-ex].
- ₁₅₉₇ [12] ATLAS Collaboration. Performance of the atlas track reconstruction algo-
₁₅₉₈ rithms in dense environments in lhc run 2. arXiv:1704.07983 [hep-ex].

- 1599 [13] ATLAS Collaboration. Properties of jet fragmentation using charged par-
1600 ticles measured with the atlas detector in pp collisions at $\sqrt{s} = 13$ tev.
1601 arXiv:1906.09254 [hep-ex].
- 1602 [14] Alex Dias and V. Pleitez. Grand unification and proton stability near the
1603 peccei-quinn scale. *Physical Review D*, 70, 07 2004.
- 1604 [15] Stefan Höche, Frank Krauss, Marek Schönherr, and Frank Siegert. Qcd ma-
1605 trix elements + parton showers. the nlo case. *Journal of High Energy Physics*,
1606 2013(4), Apr 2013.
- 1607 [16] Diederik P. Kingma and Jimmy Ba. Adam: A method for stochastic opti-
1608 mization, 2014.
- 1609 [17] David Krohn, Jesse Thaler, and Lian-Tao Wang. Jets with variable r. *Journal*
1610 *of High Energy Physics*, 2009(06):059–059, Jun 2009.
- 1611 [18] Gregory Soyez Matteo Cacciari, Gavin P. Salam. The anti- k_T jet clustering
1612 algorithm. arXiv:0802.1189 [hep-ph].
- 1613 [19] Duccio Pappadopulo, Andrea Thamm, Riccardo Torre, and Andrea Wulzer.
1614 Heavy vector triplets: bridging theory and data. *Journal of High Energy*
1615 *Physics*, 2014(9), Sep 2014.
- 1616 [20] Antonio Pich. The Standard Model of Electroweak Interactions. In *Proceed-
1617 ings, High-energy Physics. Proceedings, 18th European School (ESHEP 2010):*
1618 *Raseborg, Finland, June 20 - July 3, 2010*, pages 1–50, 2012. [,1(2012)].
- 1619 [21] Lisa Randall and Raman Sundrum. A Large mass hierarchy from a small
1620 extra dimension. *Phys. Rev. Lett.*, 83:3370–3373, 1999.
- 1621 [22] Sebastian Raschka. Model evaluation, model selection, and algorithm selec-
1622 tion in machine learning, 2018.
- 1623 [23] Tania Robens and Tim Stefaniak. Lhc benchmark scenarios for the real higgs
1624 singlet extension of the standard model. *The European Physical Journal C*,
1625 76(5), May 2016.
- 1626 [24] Alex Sherstinsky. Fundamentals of recurrent neural network (RNN) and long
1627 short-term memory (LSTM) network. *CoRR*, abs/1808.03314, 2018.
- 1628 [25] Muhammed Ali Sit and Ibrahim Demir. Decentralized flood forecasting using
1629 deep neural networks. Jun 2019.
- 1630 [26] Wojciech Zaremba, Ilya Sutskever, and Oriol Vinyals. Recurrent neural net-
1631 work regularization, 2014.